

**Some pages of this thesis may have been removed for copyright restrictions.**

If you have discovered material in Aston Research Explorer which is unlawful e.g. breaches copyright, (either yours or that of a third party) or any other law, including but not limited to those relating to patent, trademark, confidentiality, data protection, obscenity, defamation, libel, then please read our [Takedown policy](#) and contact the service immediately (openaccess@aston.ac.uk)

**MULTISCALE MODELLING OF BONDING PERFORMANCE OF  
BITUMINOUS MATERIALS**

YANGMING GAO

Doctor of Philosophy

ASTON UNIVERSITY

December 2019

©Yangming Gao, 2019

Yangming Gao asserts his moral right to be identified as the author of this thesis

This copy of the thesis has been supplied on condition that anyone who consults it is understood to recognise that its copyright belongs to its author and that no quotation from the thesis and no information derived from it may be published without appropriate permission or acknowledgement.

Aston University

## Multiscale Modelling of Bonding Performance of Bituminous Materials

Yangming Gao

Doctor of Philosophy

2019

### Thesis Summary

Bonding performance of bituminous materials fundamentally determines the resistance of asphalt to fatigue cracking which is one of the major distresses in asphalt pavements. Running laboratory fatigue tests of bitumen or asphalt is costly and time consuming, resulting in empirical-based fatigue life prediction models. To reveal the debonding mechanism of fatigue damage in bitumen, a hierarchical multiscale modelling framework was developed in this thesis to understand and model the bonding performance of bitumen in order to accurately and reliably predict fatigue crack initiation and propagation in bitumen.

At the nanoscale, the bonding performance of bitumen was characterised by bond energy using molecular dynamics (MD) simulations, which was validated by contact angle measurements. The MD modelling and simulations were performed to understand the effects of minerals and oxidative ageing on the bonding performance of bitumen at the molecular level. At the microscale, cohesive debonding performance of bitumen under a rotational shear fatigue load was first quantified by a DSR-C model to predict fatigue crack length. Then, based on the quantification of cohesive debonding behaviour at the nanoscale, an energy-based fatigue crack initiation criterion was developed for bitumen using a viscoelastic Griffith's theory. At the macroscale, the cohesive debonding behaviour in bitumen was modelled for fatigue crack propagation by a pseudo J-integral based Paris' law. Dynamic shear rheometer (DSR) tests were conducted to validate the developed models at different environmental and loading conditions.

Results indicated that the cohesive bond energy predicted at the nanoscale can be used as a fundamental material property and scale-independent input for the cohesive debonding modelling for fatigue cracking of bitumen at the microscale. Adhesive bonding performance of bitumen with minerals is attributed to non-bond energy including van der Waals and electrostatic interactions. Bitumen oxidative ageing trends to strengthen interfacial electrostatic interaction since the introduction of oxygen atoms makes bitumen polarity stronger. The developed DSR-C model is capable of accurately predicting the fatigue crack length in bitumen. The energy-based crack initiation criterion along with the DSR fatigue tests can act as a substitute for surface energy tests. The crack propagation model based on the pseudo J-integral Paris' law is able to characterise the fatigue crack evolution in bitumen. The Paris' law coefficients  $A$  and  $n$  are temperature dependent fundamental material property, which are demonstrated to be independent of loading frequency or loading amplitude.

**Keywords:** Multiscale modelling, bituminous materials, bond energy, fatigue cracking, crack initiation and propagation

## **Dedication**

To my parents and my wife for their love, patience and encouragement

## Acknowledgements

I would like to sincerely thank my supervisor, Dr. Yuqing Zhang, for his constant support, guidance and encouragement. Dr. Yuqing Zhang has carefully guided me to overcome many obstacles throughout my research. I sincerely appreciate his technical and professional advice. He has made the constant efforts to ensure I had the necessary resources to complete my thesis work. I could not finish the research without his help. My interactions with Dr. Yuqing Zhang have opened career opportunities. I am so lucky that I had my most important three-year study under his supervision.

I would also like to thank my associate supervisor, Dr. Dmitry Nerukh, for his support and valuable suggestions. I want to thank Dr. Mujib Rahman and Dr. Jiawei Wang for serving at my viva examination and providing fruitful comments on my work. I am grateful to Dr. Paul Topham and Dr. John Elgy for their insightful comments on my annual reports. My appreciation is extended to Mrs. Mahvash Miri and Dr. Yang Bai for their help on my tests.

My sincere appreciation also goes to my colleagues and friends who make my PhD journey enjoyable. Many thanks to Dr. Fan Gu, Dr. Linglin Li, Mrs. Eman L. Omairey and Mr. Yifan Li for their support, friendship and encouragement.

I would also like to express my deepest gratitude to my parents for their selfless love and endless support. Special thanks to my wife, Mrs. Dan Ren, for her love, understanding, and encouragement.

I appreciate the financial support provided by Aston University via a PhD studentship that makes this research possible.

# List of Contents

Thesis Summary .....	2
Dedication .....	3
Acknowledgements .....	4
List of Contents .....	5
List of Tables.....	8
List of Figures .....	9
Chapter 1 Introduction .....	12
1.1 Background .....	12
1.2 Problem Statement .....	15
1.2.1 Research gap at the nanoscale .....	15
1.2.2 Research gap at the microscale and macroscale .....	16
1.3 Research Objectives .....	17
1.4 Thesis Outline .....	18
Chapter 2 Nanoscale Modelling of Bonding Performance of Bitumen .....	20
2.1 Overview .....	20
2.2 Introduction .....	21
2.3 MD Simulation Method .....	23
2.4 Molecular Models of Bitumen .....	25
2.5 Materials and Laboratory Tests.....	29
2.5.1 Theoretical background .....	29
2.5.2 Materials .....	30
2.5.3 Sample preparation .....	31
2.5.4 Contact angle measurements .....	32
2.5.5 Cohesive bond energy.....	33
2.6 Cohesive Bonding Performance of Bitumen.....	34
2.6.1 Validation of molecular model .....	34
2.6.2 Calculation of cohesive bond energy.....	35
2.7 Adhesive Bonding Performance of Bitumen .....	36
2.7.1 Molecular models of aggregate minerals.....	37
2.7.2 Molecular models of bitumen-mineral interface.....	37
2.7.3 Molecular interaction between bitumen and minerals .....	39
2.7.4 Calculation of adhesive bond energy.....	41
2.7.5 Adhesive bond energy in dry condition.....	41
2.7.6 Adhesive bond energy in wet condition .....	43
2.8 Conclusions .....	45
Chapter 3 Nanoscale Modelling of Oxidative Ageing Effect on Bitumen Bonding Performance.....	47
3.1 Overview .....	47
3.2 Introduction.....	48
3.3 Bitumen Oxidative Ageing.....	50
3.4 Molecular Models of Aged Bitumen.....	51

3.5	Materials and Laboratory Tests.....	53
3.6	Cohesive Bonding Performance of Aged Bitumen .....	54
3.6.1	Hardening mechanism of the aged bitumen .....	54
3.6.2	Calculation of cohesive bond energy.....	56
3.7	Adhesive Bonding Performance of Aged Bitumen.....	57
3.7.1	Molecular models of aged bitumen-mineral interface .....	57
3.7.2	Molecular structure of bitumen on mineral surfaces .....	58
3.7.3	Effect of oxidative ageing on bitumen adhesive bonding performance in dry condition.....	62
3.7.4	Effect of oxidative ageing on bitumen adhesive bonding performance in wet condition .....	67
3.7.5	Combined effect of oxidative ageing and water on bitumen adhesive bonding performance.....	70
3.8	Conclusions.....	72
<b>Chapter 4 Quantifying Cohesive Debonding in Bitumen Under a Rotational Shear Fatigue Load .....</b>		
		<b>74</b>
4.1	Overview .....	74
4.2	Introduction.....	74
4.3	Linear Viscoelastic Analysis of Bitumen.....	77
4.4	Damage Viscoelastic Analysis of Bitumen.....	79
4.5	Modelling Fatigue Crack Length in Bitumen Based on Damage Mechanics ..	80
4.6	Materials and Laboratory Tests.....	83
4.6.1	Materials .....	83
4.6.2	Sample preparation .....	83
4.6.3	Test methods.....	84
4.7	Results and Discussion.....	87
4.7.1	Measurement of crack length.....	87
4.7.2	Validation of crack length model.....	89
4.7.3	Crack growth in bitumen .....	94
4.8	Conclusions.....	95
<b>Chapter 5 Microscale Modelling of Cohesive Debonding for Fatigue Crack Initiation in Bitumen .....</b>		
		<b>97</b>
5.1	Overview .....	97
5.2	Introduction.....	97
5.3	Viscoelastic Characterisation of Bitumen with Pseudostrain.....	99
5.4	Definition of Fatigue Crack Initiation in Bitumen .....	101
5.5	Modelling Fatigue Crack Initiation in Bitumen Using Griffith's Criterion ...	104
5.5.1	Energy redistribution due to 'factory-roof' cracking.....	104
5.5.2	Crack initiation criterion .....	106
5.6	Materials and Laboratory Tests.....	106
5.7	Results and Discussion.....	107
5.7.1	Determination of model parameters .....	107
5.7.2	Implementation in prediction of surface energy .....	108
5.8	Conclusions.....	109
<b>Chapter 6 Macroscale Modelling of Cohesive Debonding for Fatigue Crack Propagation in Bitumen.....</b>		
		<b>111</b>
6.1	Overview .....	111
6.2	Introduction.....	111

6.3 Dissipated Pseudostrain Energy (DPSE) for Crack Growth .....	113
6.4 Modelling Crack Propagation in Bitumen Using Pseudo J-integral Paris' Law .....	115
6.5 Materials and Laboratory Tests.....	116
6.6 Results and Discussion.....	117
6.6.1 Description of fatigue crack propagation in bitumen .....	117
6.6.2 Paris' law coefficients A and n.....	119
6.7 Conclusions .....	122
<b>Chapter 7 Summaries, Conclusions and Recommendations.....</b>	<b>124</b>
7.1 Summaries.....	124
7.2 Conclusions .....	125
7.3 Recommendations .....	127
List of References.....	129

## List of Tables

Table 2-1 Compositions of bitumen molecular model used for MD simulations.....	28
Table 2-2 Surface energy components of probe liquids for contact angle measurements (mJ/m <sup>2</sup> ).....	31
Table 2-3 Contact angles between tested bitumen and probe liquids (°).....	33
Table 2-4 Surface energy components of tested bitumen (mJ/m <sup>2</sup> ).....	33
Table 2-5 Thermodynamic properties of bitumen from MD simulations.....	34
Table 2-6 Cohesive bond energy of bitumen from MD simulations. ....	36
Table 2-7 The details of four minerals used for MD simulations.....	38
Table 2-8 Adhesive bond energy between minerals and bitumen in dry and wet conditions. ..	42
Table 3-1 Compositions of aged bitumen molecular model at different oxidation levels used for MD simulations. ....	52
Table 3-2 Contact angles between aged bitumen and liquid probes (°). ....	53
Table 3-3 Surface energy components of aged bitumen (mJ/m <sup>2</sup> ).....	53
Table 3-4 Cohesive bond energy of aged bitumen from MD simulations.....	57
Table 3-5 First peak positions of RDF curves for asphaltene-asphaltene pair in bulk bitumen model and four interfacial models at different oxidation levels. ....	60
Table 3-6 Slopes of MSD curves for asphaltenes in bulk bitumen model and four interfacial models at different oxidation levels. ....	62
Table 4-1 Shear fatigue testing plan. ....	85
Table 4-2 Calculated vs. measured results for effective radius and crack length in time sweep (TS) tests at different load cycles for two bitumen materials (@ 5% strain level, 20 °C and 10 Hz).....	92
Table 4-3 Calculated vs. measured results for effective radius and crack length in time sweep (TS) tests at different conditions. ....	93
Table 6-1 Laboratory test plan.....	117

## List of Figures

Figure 1-1 Hierarchical structure of bituminous materials.....	13
Figure 2-1 Molecular structures of asphaltene fraction. (Carbon atoms are grey, hydrogen atoms are white, oxygen atoms are red, sulphur atoms are yellow, and blue is nitrogen.) .....	26
Figure 2-2 Molecular structures of resin fraction.....	26
Figure 2-3 Molecular structures of aromatic fraction.....	27
Figure 2-4 Molecular structures of saturate fraction. ....	27
Figure 2-5 Molecular models of bitumen after equilibration. (a) Bulk model of bitumen. (b) Film model of bitumen with free surfaces. ....	28
Figure 2-6 Bitumen sample preparation. (a) Bitumen in small containers. (b) Glass slide samples.....	32
Figure 2-7 Contact angle measurements of bitumen. (a) Tensiometer from Biolin Scientific. (b) Dispensing a drop of the probe liquid on the bitumen sample surface.....	32
Figure 2-8 Measured cohesive bond energy of bituminous binders.....	34
Figure 2-9 An atomistic model of microcline substrate used for MD simulations.....	38
Figure 2-10 Bitumen-mineral interface models for (a) the bitumen-microcline interface system and (b) bitumen-water-microcline interface system.....	39
Figure 2-11 Bitumen-mineral interface systems after MD simulations. (a) Quartz-bitumen model. (b) Calcite-bitumen model. (c) Albite-bitumen model. (d) Microcline-bitumen model.....	40
Figure 2-12 Bitumen-water-mineral interface systems after MD simulations. (a) Quartz-water-bitumen model. (b) Calcite-water-bitumen model. (c) Albite-water-bitumen model. (d) Microcline-water-bitumen model. ....	40
Figure 2-13 Contribution of non-bond components including van der Waals and electrostatic energy to total adhesive bond energy ( $W_{MB-dry}$ ) for different mineral-bitumen systems. ....	43
Figure 2-14 Adhesion degradation ratio ( $R_{AD}$ ) for four mineral-bitumen systems.....	45
Figure 3-1 Molecular structures of oxidised asphaltene fraction. ....	50
Figure 3-2 Molecular structures of oxidised resin fraction. ....	51
Figure 3-3 Molecular structures of oxidised aromatic fraction. ....	51
Figure 3-4 Bitumen bulk models at different oxidation levels. (a) Virgin model. (b) Lightly-oxidised (LO) model. (c) Heavily-oxidised (HO) model. ....	52
Figure 3-5 Measured cohesive bond energy of aged bituminous binders. ....	53
Figure 3-6 Density of bulk bitumen model at different oxidation levels. ....	54
Figure 3-7 Cohesive energy density (CED) of bulk bitumen model at different oxidation levels including two components, namely van der Waals and electrostatic intermolecular interactions. ....	55
Figure 3-8 Fraction of free volume (FFV) of bulk bitumen model at different oxidation levels. ....	56
Figure 3-9 Aged bitumen-mineral interface models and simulations. (a) The heavily-oxidised bitumen-albite model. (b) The heavily-oxidised bitumen-water-albite model. (c) The change of energy during the simulations. ....	58
Figure 3-10 Nanostructures of bitumen at (a) heavily-oxidised bitumen-quartz interface and (b) heavily-oxidised bitumen-water-quartz interface obtained from MD simulations. ....	59
Figure 3-11 RDFs of asphaltene-asphaltene pair in bitumen-microcline interfacial model at	

different oxidation levels.....	60
Figure 3-12 MSDs of asphaltenes in bitumen-microcline interfacial model at different oxidation levels. ....	61
Figure 3-13 Adhesive bond energy for bitumen-quartz interface model in the dry condition and different oxidation levels. ....	63
Figure 3-14 Centre-to-centre distance ( $\text{\AA}$ or $10^{-10}$ m) between bitumen mass and mineral matrix for (a) bitumen-quartz interface model and (b) bitumen-calcite interface model at different oxidation levels. ....	64
Figure 3-15 Adhesive bond energy for bitumen-calcite interface model in dry condition and different oxidation levels. ....	65
Figure 3-16 Adhesive bond energy for bitumen-albite interface model in dry condition and different oxidation levels. ....	66
Figure 3-17 Adhesive bond energy for bitumen-microcline interface model in dry condition and different oxidation levels. ....	67
Figure 3-18 Adhesive bond energy of bitumen-quartz model in dry and wet conditions and at different oxidation levels. ....	68
Figure 3-19 Adhesive bond energy of bitumen-calcite model in dry and wet conditions and at different oxidation levels. ....	69
Figure 3-20 Adhesive bond energy of bitumen-albite model in dry and wet conditions and at different oxidation levels. ....	70
Figure 3-21 Adhesive bond energy of bitumen-microcline model in dry and wet conditions and at different oxidation levels. ....	70
Figure 3-22 Sensitivity of adhesion to oxidative ageing ( $S_{O-H}$ and $S_{O-L}$ ) and water ( $S_w$ ) for quartz (acidic), calcite (weak alkali) and albite (strong alkali) minerals. ....	72
Figure 4-1 Schematic of a cylindrical sample with a circumferential crack in dynamic shear rheometer (DSR) tests. ....	80
Figure 4-2 Results of linear amplitude sweep (LAS) tests at 20 °C and 10 Hz including shear modulus ( $ G^*_0 $ ) and phase angle ( $\delta_0$ ) for unaged X-70 bitumen with strain levels. ....	85
Figure 4-3 Results of time sweep (TS) test at 5% strain, 20 °C and 10 Hz including shear modulus ( $ G^*_N $ ) and phase angle ( $\delta_N$ ) for unaged X-70 bitumen with load cycles. ....	87
Figure 4-4 Images of cracking surfaces for bitumen sample after time sweep (TS) tests at 20 °C and 10 Hz. (a) Cracking morphology under 42000 load cycles at 5% strain level for virgin unmodified bitumen 40/60 ( $B_v$ ). (b) Definition and measurement of the effective radius and crack length for $B_v$ . (c) Cracking morphology under 24000 load cycles at 7% strain level for virgin polymer modified bitumen X-70 ( $A_v$ ). (d) Cracking morphology under 24000 load cycles at 5% strain level for aged polymer modified bitumen X-70 ( $A_a$ ). (e) Cracking morphology under 24000 load cycles at 5% strain level for aged unmodified bitumen 40/60 ( $B_a$ ). ....	89
Figure 4-5 Shear modulus vs. load cycles and crack surface images for three duplicate samples terminated at different load cycles (@ 5% strain level, 20 °C and 10 Hz). ....	91
Figure 4-6 Comparison between calculated and measured crack length in time sweep (TS) tests at different load cycles for two bitumen materials (@ 5% strain level, 20 °C and 10 Hz). ....	92
Figure 4-7 Comparison between calculated and measured crack length in time sweep (TS) tests at different conditions (@ 24,000 load cycles). ....	94
Figure 4-8 Crack length in bitumen vs. number of load cycle under a rotational shear fatigue load (@ 5% strain level, 20 °C and 10 Hz). ....	95
Figure 5-1 Fatigue cracking in bituminous binders under a rotational shear fatigue load. (a) Cracking morphology. (b) Cracking model. $c$ is the crack length, $r_0$ is the original radius of sample, and $h$ is the height of sample. ....	102

Figure 5-2 Crack growth with the number of load cycles for a cylindrical bitumen sample subjected to a rotational shear fatigue load. ....	102
Figure 5-3 Crack growth rate with the crack length for a cylindrical bitumen sample subjected to a rotational shear fatigue load. ....	103
Figure 5-4 Edge flow damage and crack initiation of ‘factory-roof’ cracking zone. $c_0$ is the edge flow damage size. $a$ is the ‘factory-roof’ crack length for crack initiation..	104
Figure 5-5 Time sweep (TS) test results at 5% strain, 20 °C and 10 Hz for an aged X-70 bitumen sample. ....	107
Figure 5-6 Comparison between the calculated results and the tested data from the contact angle measurements. ....	109
Figure 6-1 Crack propagation including ‘shallow’ crack growth and ‘deep’ crack growth. ..	118
Figure 6-2 Relationship between crack growth rate ( $dc/dN$ ) and energy release rate ( $\Delta J_R$ ) during deep (steady) crack growth at 20 °C and 10 Hz under 5% strain level.....	119
Figure 6-3 Paris’ law coefficients at different temperatures and ageing conditions (@ 10 Hz and 5% strain level).....	120
Figure 6-4 Paris’ law coefficients at different loading frequencies and strain levels for different binders. ....	122

# Chapter 1 Introduction

## 1.1 Background

Asphalt pavements are the most common type used for road construction and make up around 90% of the paved roads in the United Kingdom (Thom, 2014). Asphalt (i.e., asphalt mixture or asphalt concrete) primarily composed of mineral aggregates bound together with bitumen is widely used for the construction of the asphalt pavement including its surface and structural layers. Under the complex environmental and loading conditions, various forms of distresses such as cracking, potholes, ravelling and stripping can occur in asphalt pavements, which are closely related to the fundamental properties and performance of bituminous materials.

The bituminous materials are mainly referred to bitumen and asphalt, which are used to pave the surfaces of road structures. Bitumen is produced from petroleum refining process with very complex chemical compositions and acts as a glue in the asphalt bonding the mineral aggregates to form a skeleton to transfer the traffic or environmental load to the underpinning layers. It contains a high percentage of hydrocarbons with a few structurally analogous heterocyclic species and functional groups including oxygen, sulphur and nitrogen atoms. Bitumen is mixed with mineral aggregates to design asphalt based on the volume fractions of individual constituents. Asphalt is a typical viscoelastic composite used to construct highway structures. Three significant characteristics of the bituminous materials are as follows:

- (1) The materials present highly time-dependent viscoelastic behaviour and their properties and performance are strongly influenced by external environmental factors such as temperature and moisture;
- (2) The materials are composed of various constituents with different molecular functional groups, e.g. non-polar saturates, aromatics, polar resins, polar asphaltenes and acidic/alkali minerals, which induce considerably complicated intermolecular interactions in bituminous materials including physical interactions and chemical reactions; and
- (3) The materials are highly heterogeneous because of the complex components with distinct material properties such as bituminous binders, mineral aggregates and air voids.

To assess the lifetime service performance of the bituminous materials, some traditional approaches have been developed based on homogeneous continuum assumptions, including continuum damage mechanics (CDM) and micromechanics methods. Although these approaches, compared to empirical trial-and-error methods, have improved the understanding of material behaviours, they are unable to associate the inherent microstructural configuration and physicochemical characteristics with the damage mechanisms of the bituminous materials. The macroscopic behaviours of the bituminous materials are governed by the structure and properties of the constituent materials at smaller scales, e.g., microscale and nanoscale. In order to improve the durability and life expectancy of the asphalt pavement, it is very necessary to understand the structure-property relationships in the bituminous materials that relate nanoscale and microscale details with macroscale performance. Thus, multiscale modelling is needed to investigate the mechanical behaviour and pavement performance of the bituminous materials based on the structure and properties of the material components at different scales.

Across wide length scales, the highly heterogeneous bituminous materials present different structural and material features. The hierarchical structure of the bituminous materials is shown in **Figure 1-1**, which is a multiscale schematic with different hierarchical levels focusing on the key length scales of asphalt.

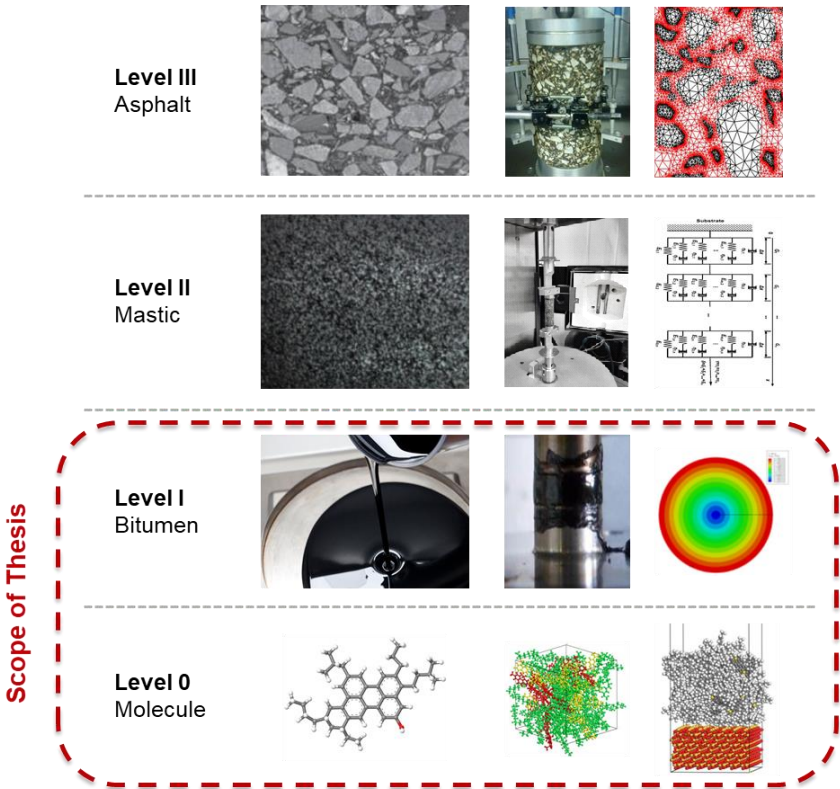


**Figure 1-1 Hierarchical structure of bituminous materials.**

At Level 0, the studies are focused on the chemical composition and molecular structure of bitumen that directly determine its physical properties. Bitumen is composed of a wide variety of hydrocarbons with heteroatoms such as oxygen, sulphur and nitrogen. Based on modern chromatographic methods, bitumen can be separated into four fractions, i.e., saturates, aromatics, resins and asphaltenes (SARA). Due to the very small length scale (Å), the molecular behaviour of bitumen cannot be easily probed through laboratory experiments. Thus, molecular dynamics (MD) modelling and simulations are required to fundamentally understand the molecular behaviour of bitumen and the effects of the external factors, e.g. temperature, oxidative ageing and mineral molecules, on the bonding performance of the materials. At Level I, the rheological properties of bitumen are investigated, which is critical for pavement performance of asphalt. Dynamic shear rheometer (DSR) is widely used to measure the viscoelastic response of bitumen. Research efforts are made to evaluate the rutting and fatigue characteristics of bitumen.

At Level II, mastic composed of bitumen, filler and fine aggregate is considered. It is referred to as the matrix phase in asphalt, which directly affects the mechanical behaviour of asphalt. The viscoelastic properties of mastic are usually characterised using a dynamic mechanical analyser (DMA). At Level III, asphalt mixture is formed by combining mastic, coarse aggregates and air voids, which is a typical multi-phase viscoelastic composite. From **Figure 1-1**, it can be seen under this framework that, across different levels, the composition, structure and properties of the constituent materials at lower scales ultimately dominate the performance of the asphalt mixture.

This thesis is focused on using a hierarchy multiscale modelling method to investigate bonding performance of bitumen from Level 0 to Level I shown in **Figure 1-1**. The bonding behaviour of bitumen is an inherent material property, which directly affects the pavement performance of the asphalt like such as moisture damage and fatigue cracking. At the nanoscale (Level 0), the bonding performance of bitumen is modelled using MD simulations to understand the fundamental mechanisms of the debonding in the bitumen and to reveal the effects of oxidative ageing and aggregate mineralogy on the bitumen's bonding performance. At the microscale and macroscale (Level I), the cohesive debonding performance of bitumen under a rotational shear fatigue load is modelled using viscoelastic damage mechanics based on the understanding of bonding performance at the nanoscale for crack initiation at the microscale and crack propagation at the macroscale. The critical link between Level 0 modelling and Level I modelling lies in the fundamental and scale-independent material parameters predicted from the nanoscale (Level 0) that can be directly used as the inputs to for cohesive fatigue debonding

modelling at the microscale and the macroscale. The fundamental investigation of bonding performance of bitumen can provide essential information to better explore and predict the properties and performance of mastic and asphalt at the higher levels (Levels II and III).

## **1.2 Problem Statement**

Fatigue cracking caused by a repeated traffic load is one of the major distresses in asphalt pavements that are constructed using asphalt composed of bitumen, aggregates and air voids. The fatigue performance of the asphalt pavements is strongly related to fatigue resistance of the bitumen. The fatigue mechanisms of the bitumen have not been well understood, particularly from the fundamental perspective of material bonding behaviour at multiple scales. The bonding behaviour of the bitumen is an inherent material property, which directly affects its fatigue performance. A bottom-up characterisation of the bitumen's bonding performance from nanoscale to macroscale is needed to fundamentally investigate the fatigue cracking in the bitumen.

In this thesis, the hierarchy multiscale modelling of the bitumen's bonding performance includes two parts, namely, molecular dynamics (MD) simulations of the bitumen's bonding performance at the nanoscale and the mechanical modelling of the bitumen's cohesive debonding for fatigue cracking characterisation at the microscale and the macroscale. The existing problems or research gap in the literature are briefly summarised in this section. More details of those problems will be addressed in the chapters later corresponding to each topic.

### **1.2.1 Research gap at the nanoscale**

At the nanoscale, MD simulations have been widely used to investigate the thermodynamic properties of bituminous materials. The three-component model (Zhang and Greenfield, 2007a) and the twelve-component model (Li and Greenfield, 2014a) are two major model bitumen systems used for molecular simulations. Based on these molecular models of the bitumen, MD modelling and simulations have been carried out to analyse the physical, rheological and mechanical properties of the bitumen. The MD modelling and simulations of bituminous materials have been discussed and summarised in two review literatures (Greenfield, 2011, Chen et al., 2018). Although the important results have been produced based on MD method, some crucial problems are not well explored:

- (1) It has been found that, for bulk modulus and adhesion strength of bitumen, the calculated results from MD simulation are greater than the measured results from laboratory experiments by about two orders of magnitude (Wang et al., 2015b, Xu and

Wang, 2016a). The discrepancy is caused by the difference in the length scale, which is the so-called “size effect”. Thus, at the molecular level, what parameters or material properties can be obtained by MD simulations as the reliable and accurate inputs for the computational constitutive models at the higher scale, e.g., microscale or macroscale? A prerequisite is believed that these identified parameters should be independent of the length scale.

- (2) Experimental studies have shown that the aggregate mineralogical composition significantly affect the adhesive bonding performance of bitumen (Horgnies et al., 2011, Zhang et al., 2015). What are the mechanisms at the molecular level that can be used to explain and model such effects of aggregates’ mineralogy on the bitumen’s bonding performance?
- (3) MD study of bitumen ageing behaviour reported that oxidative ageing has a significant impact on molecular structure and physical properties of bitumen (Pan and Tarefder, 2016, Xu and Wang, 2017). However, it is still unclear how the oxidative ageing affects the adhesive bonding performance of bitumen at the molecular level.

### **1.2.2 Research gap at the microscale and macroscale**

At the microscale and macroscale, focus is given on the mechanics modelling of bitumen cohesive debonding performance for fatigue characterisation. Researchers have made efforts to characterise the fatigue properties of bitumen at intermediate temperatures. Based on dynamic shear rheometer (DSR) tests, several fatigue parameters were proposed to evaluate the fatigue resistance of bitumen, including the SHRP fatigue factor  $|G^*| \cdot \sin \delta$ , dissipated energy ratio (DER) (Ghuzlan and Carpenter, 2000, Anderson et al., 2001, Bonnetti et al., 2002), ratio of dissipated energy change (RDEC) (Shen and Carpenter, 2005, Shen et al., 2006, Shen et al., 2010) and fatigue performance parameter  $N_f$  based on the viscoelastic continuum damage (VECD) mechanics (Hintz et al., 2011b, Hintz and Bahia, 2013a). Recently, Hintz and Bahia (2013b) investigated the fatigue damage mechanism in bitumen to improve these fatigue characterisation methods. It was found that, under a cyclic torsional load, the fatigue damage in a cylindrical bitumen sample is a circumferential crack that initiates at the edge of the sample and propagates toward the centre. However, several key problems have not been well addressed:

- (1) Hintz and Bahia (2013b) predicted the crack length in the bitumen based on the decrease of the measured torque with the number of load cycles during the DSR time sweep testing. The results showed that the predicted crack lengths are less than the measured values, particularly at greater load cycles. Thus, there is a need to accurately

predict the fatigue crack length in the bitumen from the fundamental mechanical perspective to quantify the cohesive debonding performance of the bitumen under a rotational shear fatigue load.

- (2) Based on the quantification of the cohesive debonding performance, when is the fatigue crack of the bitumen initiated under a rotational shear fatigue load at the microscale? Crack initiation refers to the onset of edge fracture, which is critical to estimate the crack propagation in the bitumen.
- (3) Based on the quantification of the cohesive debonding performance, how does the fatigue crack of the bitumen evolve once the crack is initiated under the rotational shear fatigue load at the macroscale? Crack propagation dominates the fatigue life in the bitumen.

### **1.3 Research Objectives**

The overall aim of this research is to develop a hierarchy multiscale model to fundamentally characterise the bonding performance of bitumen. This multiscale model is capable of providing an essential basis for the bitumen's fatigue damage predictions including the reliable predictions of material fundamental properties, fatigue crack characterisation, crack initiation and evolution laws at nano, micro and macro scales. This will pave a solid foundation for the constitutive modelling and performance predictions of mastic and asphalt at larger scales. A bottom-up understanding of the bitumen will enable future design of more durable asphalt materials. To achieve this research aim, the following specific objectives are proposed:

- (1) At the nanoscale, to model the bonding performance of bitumen using MD simulations to identify parameters which can serve as fundamental and scale-independent inputs for the cohesive debonding modelling at the microscale;
- (2) At the nanoscale, to reveal the molecular mechanisms of the effects of minerals and oxidative ageing on the bonding performance of the bitumen using the MD simulations;
- (3) To quantify cohesive debonding behaviour of the bitumen under a rotational shear fatigue load which would be able to serve as a direct and fundamental parameter to evaluate the resistance of the bitumen to fatigue cracking;
- (4) At the microscale, to model the cohesive debonding performance for the fatigue crack initiation in the bitumen based on the fundamental and scale-independent parameters obtained from the MD simulations at the nanoscale; and
- (5) At the macroscale, to model the cohesive debonding performance for fatigue crack propagation in the bitumen based on the quantification of cohesive debonding.

## 1.4 Thesis Outline

This thesis is composed of four journal papers that have been published and one paper that is being submitted for review. To avoid unnecessary repetitions, the contents of these papers are slightly modified in this thesis to ensure the article flow. Besides, further studies beyond the papers are included in this thesis to present a complete multiscale characterisation of the bitumen. This thesis includes seven chapters and is organised as follows:

Chapter 1 presents an introduction, including background, problem statement, research objectives and thesis outline.

Chapter 2 presents the nanoscale modelling of the bonding performance of bitumen using MD simulations, which includes the construction of molecular models, MD simulations, identification and calculation of bitumen bond energy and the effects of minerals on the bonding performance. Contact angle measurements were conducted to determine the cohesive bond energy of the bitumen which were used to validate the predicted ones from the MD simulations. The predicted cohesive bond energy of bitumen at the nanoscale can be used as an input for the cohesive debonding modelling for bitumen fatigue crack initiation at the microscale. The MD investigation in this chapter has been published as a paper in the *Construction and Building Materials* (Gao et al., 2018).

Chapter 3 presents the nanoscale modelling of oxidative ageing effect on the bitumen's bonding performance on different mineral surfaces. The aged molecular models were built and their MD simulations were performed. The calculated bond energy of the aged bitumen is validated by the contact angle measurements. The molecular mechanism of the effects of the oxidative ageing on the bitumen's bonding performance is discussed based on the developed models. The MD investigation in this chapter has been published as a paper in the *Applied Surface Science* (Gao et al., 2019).

Chapter 4 presents a quantification of the cohesive debonding performance of bitumen under a torsional shear fatigue load. A dynamic shear rheometer (DSR) based crack length (DSR-C) model is developed to accurately predict the fatigue crack length in the bitumen. The crack length predicted by the DSR-C model is able to serve as a direct and fundamental parameter to evaluate the resistance of the bitumen to fatigue cracking. The DSR-C model paves a solid foundation for the cohesive debonding modelling of bitumen to determine fatigue crack initiation and propagation at the microscale and the macroscale (in Chapters 5 and 6), respectively. This chapter is a paper published in the *Road Materials and Pavement Design* (Zhang and Gao, 2019).

Chapter 5 presents the microscale modelling of the cohesive debonding for fatigue crack initiation in bitumen. Based on the bitumen cohesive bond energy predicted from the MD simulations at the nanoscale and the quantification of cohesive debonding in Chapter 4, a crack initiation criterion of the bitumen under a rotational shear fatigue load is proposed using the viscoelastic Griffith's theory. This chapter is summarised in a paper that is being submitted for publication in an international journal.

Chapter 6 presents macroscale modelling of the cohesive debonding for fatigue crack propagation in bitumen. Following the characterisation of fatigue crack initiation in Chapter 5, based on the quantification of cohesive debonding in Chapter 4, a crack propagation model is developed using a pseudo J-integral Paris' law to characterise the crack evolution in the bitumen under a rotational shear fatigue load. This chapter has been published as a paper in the *Transportation Research Record: Journal of the Transportation Research Board* (Gao et al., 2020).

Chapter 7 presents the summaries and conclusions from this thesis as well as the recommendations for future studies.

# Chapter 2 Nanoscale Modelling of Bonding Performance of Bitumen\*

## 2.1 Overview

This chapter aims to model the bonding performance of bitumen using molecular dynamics (MD) simulations and address the effects of minerals on the bitumen bonding performance at the nanoscale. The molecular models of the bitumen are built based on saturates, aromatics, resins and asphaltenes (SARA) four fractions. Surface energy of the bitumen is predicted from the MD simulations and then cohesive bond energy of the bitumen can be obtained. Contact angle measurements are experimentally obtained to validate the predicted cohesive bond energy from the MD simulations. The molecular models of bitumen-mineral interface systems are constructed using four representative minerals (namely quartz, calcite, albite and microcline) in aggregates to investigate the effects of the minerals on adhesive bonding performance of the bitumen. The adhesive bonding performance is quantified by adhesive bond energy, defined as the energy required to separate a unit area of the bitumen-mineral interface.

The results show that the predicted cohesive bond energy of the bitumen from the MD simulations agrees well with the measured results from the contact angle measurements. The predicted cohesive bond energy of the bitumen at the nanoscale can be used as a fundamental and scale-independent input for the mechanics modelling of bitumen fatigue cracking at the next higher scale. The adhesion bonding performance between bitumen and minerals is attributed to the non-bond interaction energy, in which the major component is van der Waals interaction for the acidic minerals (e.g., quartz) and the electrostatic interaction for the alkali minerals (e.g., calcite, albite and microcline). It is found that the adhesive bonding performance of the bitumen with the four minerals is ranked as microcline > albite > calcite > quartz in both dry and wet conditions. Moisture can reduce the adhesion between bitumen and minerals by 82%, 84%, 18% and 1% for quartz, calcite, albite and microcline, respectively. It is concluded that the adhesive bonding performance of the bitumen strongly depends on the chemistry and

---

\* Reprinted with permission from Elsevier: **Y. Gao**, Y. Zhang, F. Gu, T. Xu, H. Wang. (2018). Impact of minerals and water on bitumen-mineral adhesion and debonding behaviours using molecular dynamics simulations. *Construction and Building Materials* 171, 214-222.

mineralogical properties of the minerals.

## 2.2 Introduction

Molecular dynamics (MD) simulation is a technique for analysing the thermodynamic properties of materials at the molecular scale through elucidating the physical movements of atoms and molecules in the system. With the development of high-performance computation, MD simulation has been widely employed to investigate the molecular interactions, thermodynamic properties and mechanical behaviour of bituminous materials.

A simple three-component molecular model was first developed to represent the bitumen. In the three-component model, *n*-C<sub>22</sub> and 1,7-dimethylnaphthalene were used to represent saturates and resin (naphthene aromatics), respectively, and two different asphaltene structures, named asphaltene-1 and asphaltene-2, were employed from the studies of Artok et al. and Groenzin and Mullins (Artok et al., 1999, Groenzin and Mullins, 2000). Asphaltene-1 contains a large aromatic core with a few short branches; while asphaltene-2 has a moderate size aromatic core with larger side chains. Zhang and Greenfield used MD simulation to estimate the properties of the three-component model bitumen system (Zhang and Greenfield, 2007a). It was shown that the densities of naphthalene and 1-methylnaphthalene from simulations were very close to the experimental data. The glass transition temperature was estimated to occur within the temperature range of 25-85 °C. The model bitumen based on the more aromatic asphaltene showed a lower isothermal compressibility and thus had a higher bulk modulus. The molecular orientations within the model bitumen system were analysed using MD simulation (Zhang and Greenfield, 2007b). It was concluded that the orientations between neighbouring molecules were influenced by molecular structure and temperature. Highly aromatic asphaltene molecules preferred to stay almost perpendicular to each other at high temperatures and almost parallel at low temperatures. And average orientation between neighbouring molecules depended on the distance between molecule centres of mass. Zhang and Greenfield also employed MD simulation to calculate relaxation time, diffusion coefficient, and viscosity of the model bitumen system over the range of 298-443 K (Zhang and Greenfield, 2007c). In the model bitumen system, the diffusion coefficient showed the smallest temperature dependence for all components.

To better understand the physical, rheological, and mechanical properties of the real bitumen, three twelve-component model bitumen systems were proposed to represent the AAA-1, AAK-1, and AAM-1 bitumens (Li and Greenfield, 2014a). More molecules were chosen in these models, which were classified into saturates, aromatics (naphthene aromatics), resins

(polar aromatics) and asphaltenes (SARA) four fractions. It was found that the density and thermal expansion coefficient for the model AAA-1 bitumen system agreed better with experimental data than that from the previous three-component model system. The viscosity, relaxation time, and dynamics of the model AAA-1 bitumen system were studied using MD simulations at the temperature range from 298.15 to 533.15 K (Li and Greenfield, 2014b). The increase in size and decrease in temperature induced a large decrease in the rotational relaxation rate of molecules. The activation energies of all twelve molecules in the model were similar, at around 42 kJ/mol. The viscosity result was consistent with experimental data, and the rotational relaxation time and diffusion coefficient changed slightly with temperature above 358.15 K.

Based on the three-component model or the twelve-component model, the MD simulation was applied to investigate a variety of bitumen properties and performance, which contains fraction interactions (Wang et al., 2015c, Xu and Wang, 2016b), oxidative ageing behaviour (Tarefder and Arisa, 2011, Pan and Tarefder, 2016, Xu and Wang, 2017), diffusion and self-healing mechanisms (Ding et al., 2016, Bhasin et al., 2010, Sun et al., 2016), mechanical properties of bitumen (Hou et al., 2017a, Hou et al., 2017b) and compatibility between bitumen and modifier (Zhou et al., 2015, Yao et al., 2017). In addition to the bitumen properties and performance, some researchers also employed the MD simulation to characterise interfacial behaviour of the bitumen, including interfacial adhesion (Xu and Wang, 2016b, Dong et al., 2017, Yao et al., 2015) and mechanical properties (Lu and Wang, 2010, Lu and Wang, 2011, Wang et al., 2015b, Xu and Wang, 2016a). Although these research efforts have produced important results for better understanding the fundamental properties of the bitumen from a more fundamental perspective, it is still found that, for bulk modulus and adhesion strength of the bitumen, the calculated results from MD simulation are greater than the measured results from macroscopic laboratory experiments by about two orders of magnitude. The discrepancy is caused by the difference in the length scale, which is the so-called “size effect”. At the nanoscale, it’s still unclear what parameters can be provided by the MD simulations as a fundamental material property and scale-independent inputs for the computational models at the higher scales.

Various forms of distress in asphalt pavements, such as moisture damage and fatigue cracking, have been widely investigated by developing a series of mechanistic models based on continuum damage theories and fracture mechanics (Kim et al., 1997, Cheng et al., 2002, Lytton et al., 2005, Masad et al., 2006, Howson, 2011, Lytton et al., 2018). It is found that moisture damage and fatigue cracking are closely related to the bonding performance of bitumen in dry and wet conditions (Cheng et al., 2002, Lytton et al., 2005, Bhasin et al., 2007, Little and Bhasin,

2006, Grenfell et al., 2014, Moraes et al., 2017). The bonding performance is generally described by the bond energy, including cohesive bond energy within the bitumen and adhesive bond energy at the bitumen-mineral interface. Thus, the bitumen bond energy is an important material property input in the constitutive modelling of asphalt. The bond energy of the bitumen can be evaluated by its surface energy components. Several experimental methods are used to measure surface energy, such as Wilhelmy plate (WP), universal sorption device (USD) and sessile drop (SD) method (Little and Bhasin, 2006). If the cohesive bond energy of the bitumen can be predicted using the MD simulations at the nanoscale and validated by the experimental methods, this parameter can potentially be identified as an input in the bitumen fatigue cracking modelling at the higher scale. Besides, existing experimental studies have shown that the aggregate mineralogical composition significantly affects the adhesive bonding performance of bitumen (Horgnies et al., 2011, Lyne et al., 2013, Apeagyei et al., 2014, Cui et al., 2014, Zhang et al., 2015). However, the molecular mechanisms of the mineral effects are not well understood. More fundamental studies are needed to investigate the effects of the minerals on the adhesive bonding performance of the bitumen by the MD simulations at the nanoscale.

The objective of this chapter is to model the bonding performance of the bitumen using the molecular dynamics (MD) simulation and to address the effects of minerals on the bitumen's bonding performance at the nanoscale. The molecular models of the bitumen are constructed using the twelve-component model. Cohesive bond energy of the bitumen is predicted by the calculated surface energy from the MD simulations. Contact angle measurements are conducted to validate the predicted cohesive bond energy. The molecular models of bitumen-mineral interface systems are built with four representative minerals in aggregates to investigate the effects of the minerals on adhesive bonding performance of the bitumen in dry and wet conditions. Adhesive bond energy is used to quantify the adhesive bonding performance of the bitumen with minerals.

### **2.3 MD Simulation Method**

Molecular dynamics (MD) simulation is a computational modelling technique for analysing fundamental material properties such as density, modulus, viscosity, diffusion and surface energy and the material performance such as deformation and debonding at the nanoscale through simulating the material atomistic movements and interactions. The principles of MD simulation are statistical mechanics and Newton's law of motion. MD is used to calculate the thermodynamic performance of a material system, in which the motion of each atom obeys Newton's law of motion.

The essential input to the MD simulation is an interatomic potential which defines the forces between atoms and is characterised by force field. A number of force fields have been developed by researchers for different materials (Rapaport and Rapaport, 2004). An appropriate force field should be able to mimic the nature of atomic interaction in a material system. The Condensed-phase Optimised Molecular Potentials for Atomistic Simulation Studies (COMPASS) force field is an *ab initio* force field and is able to predict dynamics of organics, inorganics and their interface systems. The COMPASS force field has a broad coverage in covalent molecules including most common organics (polymers). More importantly, it has extended coverage for inorganic materials (metals, metal oxides, and metal halides using various non-covalent models). The combination of force field parameters for organics and inorganics makes the COMPASS force field possible to study the interfacial interaction in the mixed systems. The COMPASS force field parameters have been validated using various calculation methods (Sun, 1998) and it has been successfully applied for simulating the bituminous materials (Zhang et al., 2009, Dong et al., 2017, Hou et al., 2017b). The COMPASS force field is described as (Sun, 1998):

$$E_{\text{total}} = E_{\text{val}} + E_{\text{non-bond}} \quad (2-1)$$

$$E_{\text{val}} = E_{\text{b}} + E_{\theta} + E_{\phi} + E_{\chi} + E_{\text{bb}'} + E_{\text{b}\theta} + E_{\text{b}\phi} + E_{\theta\phi} + E_{\theta\theta'} + E_{\theta\theta'\phi} \quad (2-2)$$

$$E_{\text{non-bond}} = E_{\text{Q}} + E_{\text{vdW}} \quad (2-3)$$

The total potential energy ( $E_{\text{total}}$ ) consists of valence and non-bond interaction terms. The valence term ( $E_{\text{val}}$ ) is contributed by covalent bonds between atoms, which contains the interactions of bond stretching ( $E_{\text{b}}$ ), angle bending ( $E_{\theta}$ ), internal torsion ( $E_{\phi}$ ), out-of-plane bending ( $E_{\chi}$ ) and the cross-coupling terms ( $E_{\text{bb}'}$ ,  $E_{\text{b}\theta}$ ,  $E_{\text{b}\phi}$ ,  $E_{\theta\phi}$ ,  $E_{\theta\theta'}$ , and  $E_{\theta\theta'\phi}$ ). The non-bond interaction term ( $E_{\text{non-bond}}$ ) quantifies the non-covalent contributions including Coulomb electrostatic energy ( $E_{\text{Q}}$ ) and van der Waals energy ( $E_{\text{vdW}}$ ).

The electrostatic interactions describe the Coulombic forces between two charged atoms. The electrostatic energy ( $E_{\text{Q}}$ ) is calculated using the Coulombic function

$$E_{\text{Q}} = \sum_{ij} \frac{q_i q_j}{r_{ij}} \quad (2-4)$$

where  $r_{ij}$  is the distance between atoms  $i$  and  $j$ , and  $q_i$  and  $q_j$  are the atomic charges, respectively.

The van der Waals interactions describe the van der Waals forces between two atoms, which are the sum of the intra and inter molecular attractive or repulsive interactions. The van der Waals energy ( $E_{\text{vdW}}$ ) is calculated using the Lennard-Jones (LJ) 9-6 potential

$$E_{vdW} = \sum_{ij} \varepsilon_{ij} \left[ 2 \left( \frac{r_{ij}^0}{r_{ij}} \right)^9 - 3 \left( \frac{r_{ij}^0}{r_{ij}} \right)^6 \right] \quad (2-5)$$

where  $r_{ij}$  is the distance between atoms  $i$  and  $j$ ,  $r_{ij}^0$  and  $\varepsilon_{ij}$  denote the LJ-9-6 parameters (constant) for the  $ij$  atom pair, respectively.

In this study, the COMPASS force field is adopted and all the MD simulations were performed at 298 K with a time step of 1 fs. Ewald summation method was applied for the electrostatic interactions, and atom-based summation with a cut-off distance of 15.5 Å was used for the van der Waals interactions. Nose-Hoover-Langevin (NHL) thermostat and Andersen barostat were applied to control the temperature and pressure, respectively. These simulation parameters were extensively tested and successfully applied for MD simulation studies of bituminous materials (Xu and Wang, 2017).

## 2.4 Molecular Models of Bitumen

Bitumen is a chemical mixture composed of a wide variety of hydrocarbons with heteroatoms such as oxygen, sulphur and nitrogen, which leads to the chemical complexity of the bitumen. Modern separation techniques divide bitumen into different fractions according to their similarity in terms of polar and molecular characteristics. Based on the concept of four fractions proposed by American Society for Testing and Materials (ASTM) D4124-09, a bitumen can be separated into saturates, aromatics, resins and asphaltenes (SARA) four fractions.

Asphaltenes act as the viscosity-building agents in bitumen and are the largest and most polar component in the bitumen system. They consist of the condensed aromatic and naphthenic molecules with a trace amount of heteroatoms (O, S and N) (Amin et al., 2011). Three different types of asphaltenes (asphaltene-phenol, asphaltene-pyrrole and asphaltene-thiophene) are used to represent the asphaltene fraction in the bitumen system. These asphaltene molecular structures modelled the laboratory measurements and calculations, thus being capable of representing the true asphaltenes (Li and Greenfield, 2011, Mullins, 2010). The molecular structures of the asphaltene fraction are shown in **Figure 2-1**.

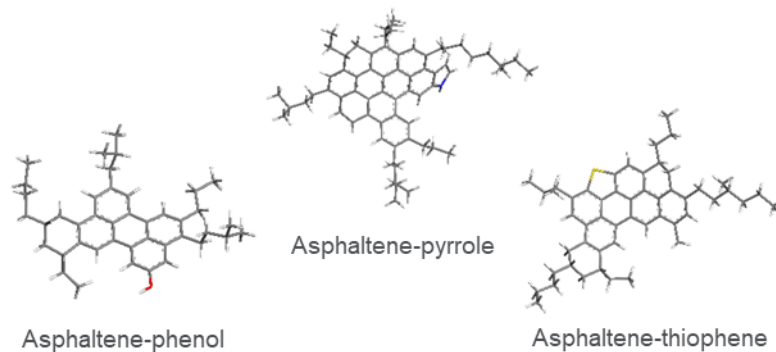


**Figure 2-1 Molecular structures of asphaltene fraction. (Carbon atoms are grey, hydrogen atoms are white, oxygen atoms are red, sulphur atoms are yellow, and blue is nitrogen.)**

Resins (polar aromatics) are the second polar fraction in bitumen and act as the stabilizer for the asphaltenes (Lesueur, 2009). Heteroatoms such as oxygen, sulphur and nitrogen are also found in resin molecules composed of polar aromatic rings and long non-polar paraffinic groups. **Figure 2-2** shows the five different molecules (quinolinohopane, thioisorenieratane, benzobisbenzothiophene, pyridinohopane and trimethylbenzene-oxane) used to represent the resin fraction. These molecular models were selected based on the analyses of petroleum found in sedimentary rock deposits in the geochemistry studies (Oldenburg et al., 2004, Koopmans et al., 1996, Koopmans et al., 1997, Marynowski et al., 2002, Cai et al., 2009).

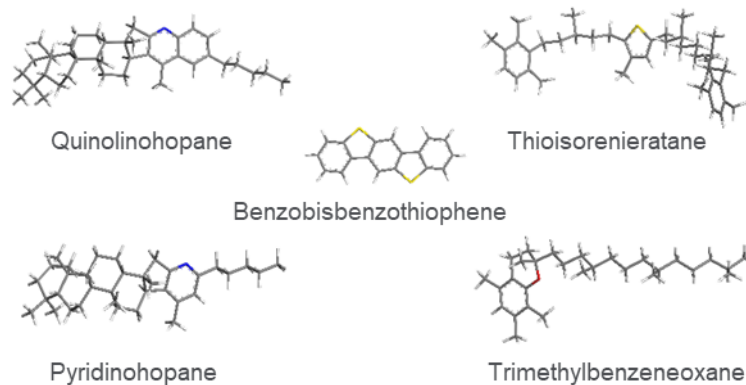


**Figure 2-2 Molecular structures of resin fraction.**

Aromatics (naphthene aromatics) are the softening component in bitumen and have the minimal polarity in the bitumen system. They are hydrocarbon structures with low molecular weights. **Figure 2-3** illustrates the molecular models of the aromatic fraction, which are named as perhydrophenanthrene-naphthalene (PHPN) and dioctyl-cyclohexane-naphthalene (DOCHN), respectively. PHPN was proposed as a main aromatic compound (Lira-Galeana and

Hammami, 2000) and DOCHN was shown as another common naphthene aromatic structure on the basis of the n-d-M method (Simanzhenkov and Idem, 2003).

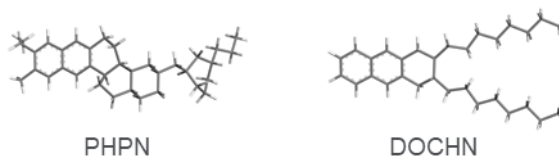


**Figure 2-3 Molecular structures of aromatic fraction.**

Saturates consist of the normal, branched and cyclic alkanes, which rarely change with time due to the lack of polar chemical functional groups. Squalane and hopane shown in **Figure 2-4** are selected as representative saturate fraction, which is consistent with the findings from the direct separation and quantitative determination of n- and iso-alkanes in neat SHRP (Strategic Highway Research Program) bitumen using urea adduction and high temperature gas chromatography (HTGC) by Netzel and Rovani (Netzel and Rovani, 2007). The specific selections of these molecular models for asphaltenes, resins, aromatics and saturates were reported and explained in detail by previous experimental and simulation studies (Li and Greenfield, 2014a).



**Figure 2-4 Molecular structures of saturate fraction.**

Based on the molecular models of the bitumen components, a molecular model of the bitumen can be constructed by using the twelve-component model, which has been demonstrated to have the similar or equivalent chemical and mechanical properties and performance to real bitumen (Li and Greenfield, 2014a). The number of each type of the component molecule in the model bitumen systems can be seen in **Table 2-1**. The bitumen model contains two types of saturates (S), two types of aromatics (A), five types of resins (R), and three types of asphaltenes (A).

A bulk model of bitumen was first constructed. The molecules of the twelve components were filled into a cubic box with an initial density of  $0.1\text{g/cm}^3$  in 3D periodical condition on the basis of the assigned weight proportions of each constituent shown in **Table 2-1**. After a geometry optimisation process, an MD simulation with an NPT ensemble (in which the number of particles, pressure, and temperature were unchanged) was conducted for 100 ps

with a time step of 1 fs to reduce the system volume. Then this configuration was further equilibrated in an NVT ensemble (where the number of particles, system volume, and temperature were unchanged) for another 100 ps to approach a stable state. The target density can be obtained from the last frame of the simulations. **Figure 2-5(a)** shows the equilibrated structure of the bulk bitumen model.

**Table 2-1 Compositions of bitumen molecular model used for MD simulations.**

SARA fractions	Molecules in model	Molecular formula	Number of molecules
Saturate	Squalane	C <sub>30</sub> H <sub>62</sub>	4
	Hopane	C <sub>29</sub> H <sub>50</sub>	4
Aromatic (Naphthene aromatic)	PHPN	C <sub>35</sub> H <sub>44</sub>	11
	DOCHN	C <sub>30</sub> H <sub>46</sub>	13
Resin (Polar aromatic)	Quinolinhopane	C <sub>40</sub> H <sub>59</sub> N	4
	Thioisorenieratane	C <sub>40</sub> H <sub>60</sub> S	4
	Benzobisbenzothiophene	C <sub>18</sub> H <sub>10</sub> S <sub>2</sub>	15
	Pyridinohopane	C <sub>36</sub> H <sub>57</sub> N	4
	Trimethylbenzeneoxane	C <sub>29</sub> H <sub>50</sub> O	5
Asphaltene	Asphaltene-phenol	C <sub>42</sub> H <sub>50</sub> O	3
	Asphaltene-pyrrole	C <sub>66</sub> H <sub>81</sub> N	2
	Asphaltene-thiophene	C <sub>51</sub> H <sub>62</sub> S	3

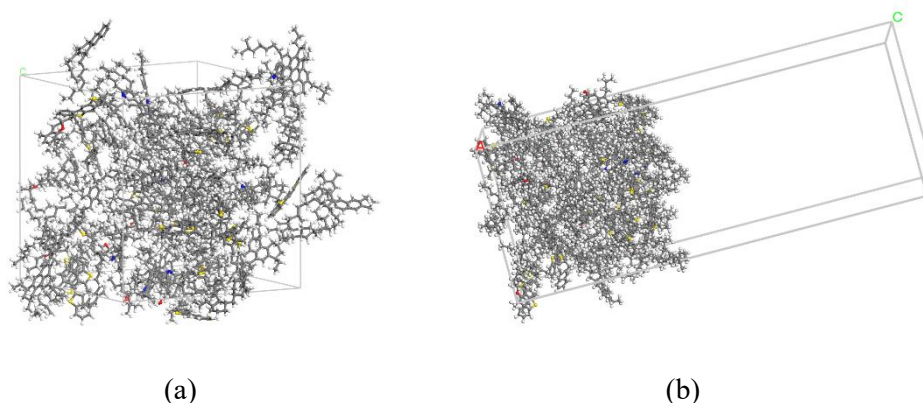


**Figure 2-5 Molecular models of bitumen after equilibration. (a) Bulk model of bitumen. (b) Film model of bitumen with free surfaces.**

A surface film model of bitumen was constructed by extending the periodic box of the equilibrated bulk model in the z direction with a vacuum layer. This creates two free surfaces at the bottom and top of the box to prevent the bitumen molecules of these two surfaces from interacting with their images along the z direction. The film model was subjected to the energy minimization run followed by 200 ps of MD simulation with an NVT ensemble at 298 K. The equilibrated structure of the bitumen film model is shown in **Figure 2-5(b)**. The equilibrated film model with the developed bulk bitumen model will be used to calculate the cohesive bond

energy of the bitumen later.

## 2.5 Materials and Laboratory Tests

The bonding performance of bitumen is characterised by the bond energy, which can be evaluated by its surface energy. Several experimental methods can be used to measure the surface energy, such as Wilhelmy plate (WP), universal sorption device (USD) and sessile drop (SD) method. In this study, the sessile drop (SD) method for contact angle measurements is used to measure the surface energy of the bitumen. This method provides a relatively simple and direct test of the contact angle between a solid and a liquid, which has been widely applied for the study of the surface energy of bituminous binders (Tan and Guo, 2013, Koc and Bulut, 2013, Moraes et al., 2017).

### 2.5.1 Theoretical background

Surface energy is a measure of the work required to create a unit area of new surface in a material. According to the commonly used Good-van Oss-Chaudhury (GvOC) theory (sometimes called acid-base theory) (van Oss et al., 1987), the total surface energy ( $\Gamma$ ) of a solid material is divided into the non-polar Lifshitz-van der Waals (LW) component ( $\Gamma^{LW}$ ) and the polar Lewis acid-base (AB) component ( $\Gamma^{AB}$ ) based on the type of the surface forces, as shown in **Equation (2-6)**. The acid-base component can further be divided into the Lewis acid component ( $\Gamma^+$ ) and the Lewis base component ( $\Gamma^-$ ), which is calculated by **Equation (2-7)**.

$$\Gamma = \Gamma^{LW} + \Gamma^{AB} \quad (2-6)$$

$$\Gamma^{AB} = 2\sqrt{\Gamma^+\Gamma^-} \quad (2-7)$$

It is very difficult or not feasible to directly measure the surface energy components of a solid material. Therefore, the contact angle method is used to indirectly determine the surface energy components. This method is a preferred approach as it is able to analyse the surface properties of the solid material at its exact surface (van Oss, 2002). The liquid-solid contact angle ( $\theta$ ) is related to the surface energy by Young's equation (Thomas, 1805) in **Equation (2-8)**. It is assumed that the solid surface is smooth, rigid, and homogeneous in Young's equation (Kwok and Neumann, 1999).

$$\Gamma_L \cos \theta = \Gamma_S - \Gamma_{SL} \quad (2-8)$$

where  $\Gamma_L$  is the surface energy of the liquid,  $\Gamma_S$  is the surface energy of the solid, and  $\Gamma_{SL}$  is the interfacial energy between the solid and the liquid.

The total interfacial energy ( $\Gamma_{SL}$ ) consists of Lifshitz-van der Waals component ( $\Gamma_{SL}^{LW}$ ) and Lewis acid-base component ( $\Gamma_{SL}^{AB}$ ), as expressed in **Equation (2-9)**. The Lifshitz-van der Waals interaction ( $\Gamma_{SL}^{LW}$ ) between two phases  $S$  and  $L$  is calculated by the Good-Girifalco-Fowkes combining rule (Good and Girifalco, 1960), as shown in **Equation (2-10)**. The acid-base interaction ( $\Gamma_{SL}^{AB}$ ) of the interfacial energy between the solid and the liquid is calculated by **Equation (2-11)** (Van Oss et al., 1988).

$$\Gamma_{SL} = \Gamma_{SL}^{LW} + \Gamma_{SL}^{AB} \quad (2-9)$$

$$\Gamma_{SL}^{LW} = \left( \sqrt{\Gamma_S^{LW}} - \sqrt{\Gamma_L^{LW}} \right)^2 \quad (2-10)$$

$$\Gamma_{SL}^{AB} = 2 \left( \sqrt{\Gamma_S^+} - \sqrt{\Gamma_L^+} \right) \left( \sqrt{\Gamma_S^-} - \sqrt{\Gamma_L^-} \right) \quad (2-11)$$

where  $\Gamma_S^{LW}$  is the Lifshitz-van der Waals component of solid,  $\Gamma_L^{LW}$  is the Lifshitz-van der Waals component of liquid,  $\Gamma_S^+$  is the Lewis acid component of solid,  $\Gamma_L^+$  is the Lewis acid component of liquid,  $\Gamma_S^-$  is the Lewis base component of solid, and  $\Gamma_L^-$  is the Lewis base component of liquid. Based on **Equations (2-6), (2-7), (2-10)** and **(2-11)**, **Equation (2-9)** is then rewritten as

$$\Gamma_{SL} = \Gamma_S + \Gamma_L - 2 \left( \sqrt{\Gamma_S^{LW} \Gamma_L^{LW}} + \sqrt{\Gamma_S^+ \Gamma_L^-} + \sqrt{\Gamma_S^- \Gamma_L^+} \right) \quad (2-12)$$

Combining **Equations (2-8)** and **(2-12)** gives the Young-Dupre equation shown in **Equation (2-13)**, which is widely used for determining the surface energy components of a solid material through contact angle measurements (van Oss, 2002).

$$(1 + \cos \theta) \Gamma_L = 2 \left( \sqrt{\Gamma_S^{LW} \Gamma_L^{LW}} + \sqrt{\Gamma_S^+ \Gamma_L^-} + \sqrt{\Gamma_S^- \Gamma_L^+} \right) \quad (2-13)$$

In **Equation (2-13)**, there are three unknowns (i.e.,  $\Gamma_S^{LW}$ ,  $\Gamma_S^+$  and  $\Gamma_S^-$ ). Thus, the surface energy components of the sample can be obtained by measuring the contact angles with at least three different liquid probes of known surface energy characteristics (i.e.,  $\Gamma_L^{LW}$ ,  $\Gamma_L^+$  and  $\Gamma_L^-$ ).

## 2.5.2 Materials

To determine the surface energy components of the bitumen, three different probe liquids with known surface energy components are needed for the contact angle measurements. The selection of these liquids is crucial as they significantly affect the calculated results (van

Oss, 2002, Lytton et al., 2005, Little and Bhasin, 2006). The liquid probes need to be pure, homogenous and immiscible with the bitumen. Their surface energy components must be known in order to back-calculate the surface energy of the bitumen using **Equation (2-13)**. In this study, distilled water, ethylene glycol, and formamide were selected as the probe liquids according to the recommendation from the literature (Moraes et al., 2017). The surface energy components of the three probe liquids are summarized in **Table 2-2**. The magnitudes of their surface energy components differ significantly, which is advantageous to accurately calculate the surface energy of the bitumen. Two kinds of bitumen were used in this study: a bitumen 40/60 and a bitumen X-70. The bitumen 40/60 is an unmodified bitumen and the bitumen X-70 is a polymer modified bitumen.

**Table 2-2 Surface energy components of probe liquids for contact angle measurements (mJ/m<sup>2</sup>).**

Liquids	$\Gamma$	$\Gamma^{LW}$	$\Gamma^+$	$\Gamma^-$
Distilled Water (W)	72.80	21.80	25.50	25.50
Ethylene Glycol (EG)	48.00	29.00	1.92	47.00
Formamide (F)	58.00	39.00	2.28	39.60

### 2.5.3 Sample preparation

The bulk bitumen was heated at 165 °C for 1 h in an oven, stirred thoroughly, and then divided into a number of small containers approximately 50 mL in capacity (**Figure 2-6 (a)**). These containers were used to prepare the bitumen samples for the contact angle measurements with three probe liquids. The process for the sample preparation was as follows:

- (1) The bitumen in the container was heated in the oven. Note that each container was only heated once to maintain the same level of ageing.
- (2) The liquid bitumen was stirred in the container and then poured on a clean glass slide with 25 mm × 75 mm × 1 mm dimensions to form a flat and smooth surface area of the bitumen with approximately 25 mm × 50 mm in size (**Figure 2-6 (b)**).
- (3) The bitumen sample was allowed to cool down to room temperature for 24 h.

It should be noted that, for each bitumen, three glass slides were used to prepare three replicates for the three probe liquids.

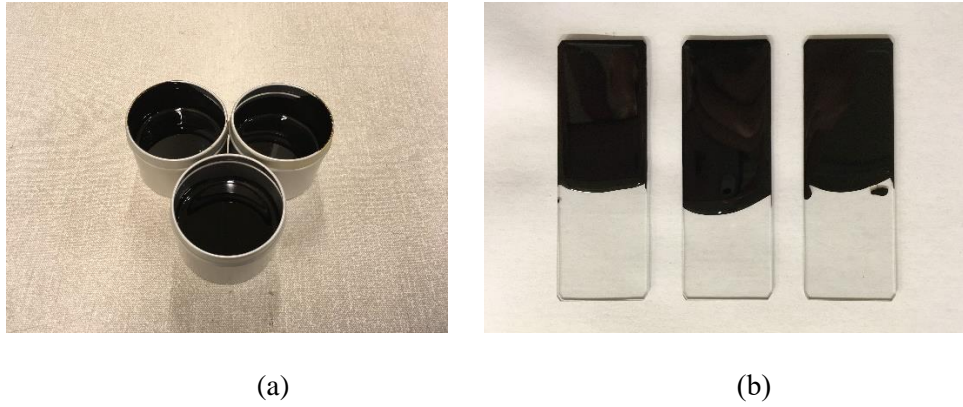


**Figure 2-6 Bitumen sample preparation. (a) Bitumen in small containers. (b) Glass slide samples.**

#### 2.5.4 Contact angle measurements

In this study, the contact angle measurements were conducted using the sessile drop (SD) method, as shown in **Figure 2-7**. The testing procedure is summarised with the following steps:

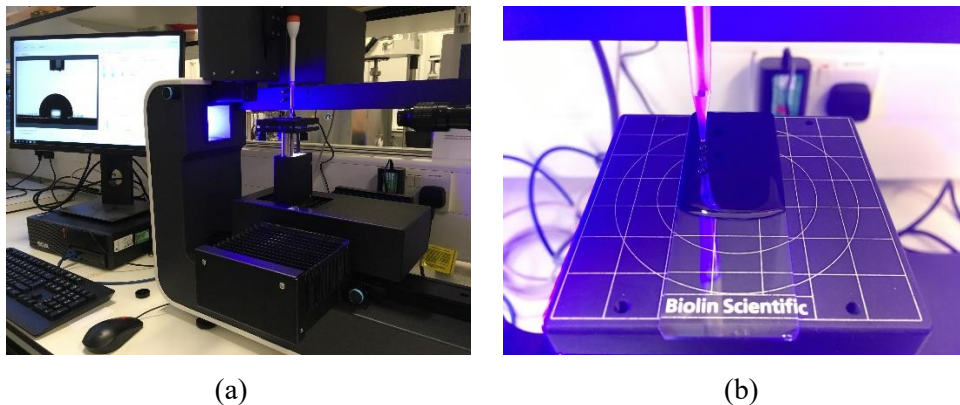


**Figure 2-7 Contact angle measurements of bitumen. (a) Tensiometer from Biolin Scientific. (b) Dispensing a drop of the probe liquid on the bitumen sample surface.**

- (1) The glass slide with the bitumen was placed between the light source and the camera.
- (2) The dispenser was rinsed by the probe liquid. The tip of the dispenser was positioned approximately 5 mm away from the top surface of the sample.
- (3) A small drop of the probe liquid was dispensed from the dispenser. With adding more volume of the probe liquid, the drop on the bitumen surface expanded to a point when the interfacial boundary with the bitumen surface started to expand. Adding the probe liquid was stopped at this point and an image of the drop was captured using the camera.
- (4) Each drop image captured was analysed to obtain the left and right contact angles.
- (5) Three measurements were conducted for each probe liquid. The average value for all

three measurements with the left and right contact angles was reported as the contact angle between the specific bitumen and the probe liquid, which was used to calculate the surface energy components of the bitumen.

The measured contact angles between the bitumens and the liquids by the sessile drop (SD) method are shown in **Table 2-3**.

**Table 2-3 Contact angles between tested bitumen and probe liquids (°).**

Bitumens	Distilled Water (W)	Ethylene glycol (EG)	Formamide (F)
40/60	105.68±0.62	82.43±0.29	90.17±0.73
X-70	104.10±0.39	79.59±0.45	89.04±0.58

### 2.5.5 Cohesive bond energy

The surface energy components of the tested bitumen can be obtained by substituting the probe liquids' surface energy components (**Table 2-2**) and the measured contact angles (**Table 2-3**) into **Equation (2-13)** and solving the three simultaneous equations. **Table 2-4** shows the surface energy of the tested bitumen with its components which are used to determine the cohesive bond energy of the bitumen.

**Table 2-4 Surface energy components of tested bitumen (mJ/m<sup>2</sup>).**

Bitumens	$\Gamma$	$\Gamma^{LW}$	$\Gamma^{AB}$	$\sqrt{\Gamma^+}$	$\sqrt{\Gamma^-}$
40/60	11.51	8.146	3.369	1.492	1.129
X-70	10.80	5.979	4.82	1.964	1.227

The cohesive bond energy of a material is defined as the energy required to create two new surfaces by the separation of the material, which can be used to explain the cohesive bonding performance of bitumen. Thus, the value of the cohesive bond energy equals to two times of the surface energy, as expressed in **Equation (2-14)**.

$$\Delta G^c = 2\Gamma \quad (2-14)$$

where  $\Delta G^c$  is the cohesive bond energy. Based on the measured surface energy shown in **Table 2-4**, the cohesive bond energy of the tested bitumen samples can be determined by using **Equation (2-14)**. **Figure 2-8** shows the measured cohesive bond energy of the bituminous binders.

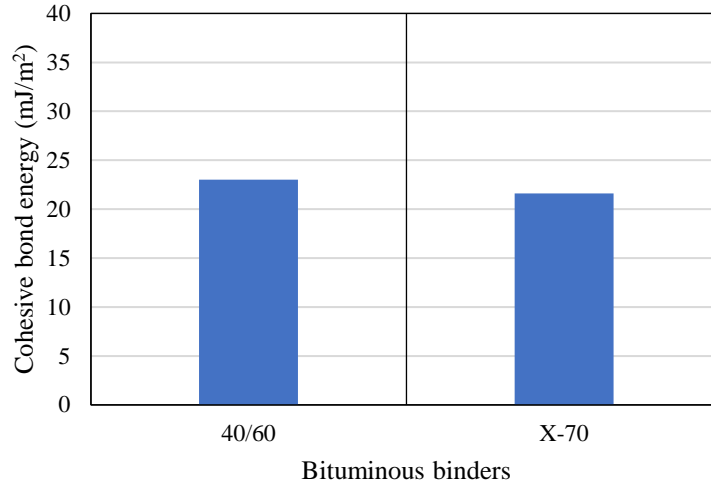


**Figure 2-8 Measured cohesive bond energy of bituminous binders.**

## 2.6 Cohesive Bonding Performance of Bitumen

### 2.6.1 Validation of molecular model

Before investigating the bonding performance of bitumen, the thermodynamic properties of the bitumen model including density and cohesive energy density (CED) were calculated and compared with experimental or simulation results reported in the literature to validate the molecular simulation models with the COMPASS force field.

Density is an important thermodynamic property of bitumen and it can be used to verify the accuracy of simulation models and force field parameters. Density value of the bitumen at temperature of 298.15 K (25 °C) was calculated by the NPT ensemble with 1 atm pressure described in **Section 2.4**. Cohesive energy density (CED) is a measure of the mutual attractiveness of molecules per unit volume to evaluate intermolecular interaction inside a bitumen molecular model. It can be used to investigate molecular attraction properties in the bitumen system and to evaluate colloidal stability in bitumen (Redelius, 2000). **Table 2-5** shows the calculated density and cohesive energy density (CED) of the bitumen with MD simulations. It can be seen that the predicted results concur with the relevant experimental or simulation results from literatures.

**Table 2-5 Thermodynamic properties of bitumen from MD simulations.**

Properties	Simulation results	Experiment or previous simulation results
Density (g/cm <sup>3</sup> )	0.981	1.01~1.04 (Lesueur, 2009)
CED (10 <sup>8</sup> J/m <sup>3</sup> )	3.041	3.19~3.22 (Wang et al., 2015c) 3.32 (Xu and Wang, 2017)

Therefore, the bitumen model and the molecular simulations with the COMPASS force field are reliable to describe the thermodynamic properties of the bitumen, which will be further used for the investigation of bitumen bonding performance.

### 2.6.2 Calculation of cohesive bond energy

The cohesive bond energy is directly related to surface energy, as discussed in **Section 2.5.5**. In the simulation, the bulk model and the film model of the bitumen described in **Section 2.4** were employed for calculating the surface energy of the bitumen. Note that the bulk model does not include any free surface within the bulk of the bitumen, whereas the film model includes two (upper and lower) free surfaces. Based on the definition of the surface energy that is the amount of energy required to create a new surface per unit area of a material, the surface energy was calculated by the difference between potential energies of the film model and its corresponding bulk model divided by the new surface area created, as expressed in **Equation (2-15)** (Deng et al., 2004, Verenich et al., 2008).

$$\Gamma = \frac{E_{\text{Film}} - E_{\text{Bulk}}}{2A_s} \quad (2-15)$$

where  $\Gamma$  is the surface energy of the bitumen;  $E_{\text{Film}}$  and  $E_{\text{bulk}}$  are the potential energies of the film model of the bitumen and the bulk model of the bitumen, respectively; and  $A$  is the new surface area created.

According to **Equation (2-14)**, the cohesive bond energy of the bitumen can be obtained from the surface energy of the bitumen, which is defined as the energy required to create two (upper and lower) new surfaces by separating a material. **Table 2-6** summarises the predicted cohesive bond energy for the bitumen molecular model with the MD simulations. To validate the simulation results, the predicted cohesive bond energy was compared to the measured results for the specific bitumen samples from laboratory tests shown in **Section 2.5** and the experimental data reported in the literature (Howson et al., 2011, Wei et al., 2014), as shown in **Table 2-6**. It can be seen that the predicted results from the virgin bitumen (VB) molecular model built in **Section 2.4** based on MD simulations lie within a range of the experimental values and are slightly greater than the results for the tested bitumens 40/60 and X-70. The small discrepancies could be caused by the difference of SARA mass fractions between the general molecular model and the tested bitumen. To support the assertion, one additional bitumen (AB) molecular model with different SARA mass fractions is built and used to predict the cohesive bond energy. It is found that the SARA fractions have a significant effect on the MD simulation results. In future study, more specific molecular models should be built

using actual measurements of SARA mass fractions to simulate the tested bitumens. Thus, the cohesive bond energy predicted based on MD simulations at the nanoscale can be identified as an input for the mechanistic modelling of bitumen at the higher scale.

**Table 2-6 Cohesive bond energy of bitumen from MD simulations.**

Molecular models	SARA mass fractions (%)				Simulation results (mJ/m <sup>2</sup> )	Experiment results (mJ/m <sup>2</sup> )
	S	A	R	A		
VB	11.1	32.1	39.6	17.2	44.26	39.92-71.56 (Howson et al., 2011) 27.54-54.18
AB	7.5	35.9	47.8	8.8	28.38	(Wei et al., 2014) 23.02 (Bitumen 40-60) 21.60 (Bitumen X-70)

## 2.7 Adhesive Bonding Performance of Bitumen

Experimental studies have shown that the aggregate mineralogical composition significantly affects adhesive bond energy of bitumen (Horgnies et al., 2011, Lyne et al., 2013, Apeagyei et al., 2014, Cui et al., 2014, Zhang et al., 2015). In this section, the molecular mechanisms of the aggregate mineral effects on the adhesive bonding performance of bitumen are investigated using the MD simulations.

Aggregates used in pavement structure are mineral rocks. The composition of the aggregates, based on chemistry and mineralogy, are quite complex and have diverse mineralogical composition. Some aggregates mainly contain one mineral such as quartzite (SiO<sub>2</sub>) and limestone (CaCO<sub>3</sub>). Other aggregate types are composed of several different minerals. For example, the major minerals in granite are quartz, mica and feldspar.

A mineral is an element or chemical compound that is normally crystalline and has been formed as a result of geological processes (Nickel, 1995). The eight most common elements of the minerals in the earth's crust are oxygen, silicon, aluminium, iron, calcium, sodium, potassium and magnesium (Pople and Williams, 2002). Natural rock mineral is polycrystal with local periodicity. A crystal structure is based on the orderly internal atomic or ionic arrangement. The structure of a mineral in the geometric form is often expressed by a box with parallel sides called the unit cell. The box with periodicity in all three dimensions is defined by six lattice parameters (lengths  $a$ ,  $b$ ,  $c$ , and angles  $\alpha$ ,  $\beta$ ,  $\gamma$ ). The crystal structure greatly affects a mineral's physical properties, and it together with the mineral chemical composition defines a mineral. Therefore, a mineral has a characteristic chemical composition and a regular

atomic structure, leading to specific physical properties.

In this study, four representative minerals (quartz, calcite, albite, and microcline) were selected to investigate adhesive bond energy of the bitumen using the MD simulations. These four minerals were selected based on that (1) they are the common minerals existing in the aggregates that are used for constructing asphalt mixtures and (2) the four minerals have been employed for the study of material selection for asphalt pavement by Little and Bhasin (2006).

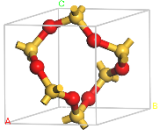
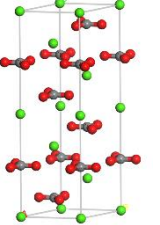
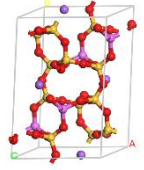
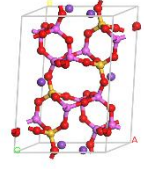
### **2.7.1 Molecular models of aggregate minerals**

Quartz, calcite, albite and microcline are selected as the minerals in this simulation. The unit cell structures and lattice parameters of these four minerals are summarised in **Table 2-7**. To model the mineral substrate, the bulk crystal was first cleaved along Miller plane (100) to expose the corresponding surface. The basis for selecting Miller plane (100) is built upon an evaluation the effects of different Miller planes on the adhesive bond energy of bitumen. Three Miller planes (100), (010) and (001) of a mineral (using quartz as an example) were used and the results obtained from the three Miller planes showed a minor difference, indicating that the use of Miller plane would have little effect on the qualitative analysis of the adhesive bond energy. Since the Miller plane (100) makes the interface model with the minimum lattice mismatch for the four minerals, the Miller plane (100) was therefore selected in the study. After geometry transformation, the crystal surface was extended to generate a two-dimension (2D) structure by repeating the unit cell in x and y directions. Then a vacuum slab was included above this extended surface to create a mineral block called a supercell with three-dimension (3D) periodic boundary conditions. The size of the developed supercells is shown in **Table 2-7**. **Figure 2-9** demonstrates the final microcline model used for the MD simulations.

### **2.7.2 Molecular models of bitumen-mineral interface**

In addition to the mineral substrates, bitumen layer models are prepared to construct the bitumen-mineral interface system models. A confined bitumen layer was created with the target density obtained from the bitumen bulk model shown in **Section 2.4**. The width and length of the confined bitumen layer was constructed to match with that of the mineral substrate developed above. The bitumen layer model first ran a geometry optimisation to minimize system energy, and an MD simulation with an NVT ensemble was then performed for 100 ps to generate an equilibrated model. The confined bitumen layer had a flat surface in the z-direction for the bitumen-mineral interface modelling.

**Table 2-7 The details of four minerals used for MD simulations.**

Minerals	Unit cell structure	Lattice parameters	Supercell size ( $\text{\AA} \times \text{\AA} \times \text{\AA}$ )
Quartz ( $\text{SiO}_2$ )		$a=b=4.910 \text{ \AA}$ , $c=5.402 \text{ \AA}$ $\alpha=\beta=90^\circ$ , $\gamma=120^\circ$	$39.28 \times 37.81 \times 20.36$
Calcite ( $\text{CaCO}_3$ )		$a=b=4.990 \text{ \AA}$ , $c=17.061 \text{ \AA}$ $\alpha=\beta=90^\circ$ , $\gamma=120^\circ$	$34.93 \times 34.12 \times 23.65$
Albite ( $\text{NaAlSi}_3\text{O}_8$ )		$a=8.115 \text{ \AA}$ , $b=12.762 \text{ \AA}$ , $c=7.158 \text{ \AA}$ $\alpha=94.218^\circ$ , $\beta=116.803^\circ$ , $\gamma=87.707^\circ$	$38.29 \times 35.79 \times 22.10$
Microcline ( $\text{KAlSi}_3\text{O}_8$ )		$a=8.573 \text{ \AA}$ , $b=12.962 \text{ \AA}$ , $c=7.219 \text{ \AA}$ $\alpha=90.567^\circ$ , $\beta=115.917^\circ$ , $\gamma=87.750^\circ$	$38.89 \times 36.10 \times 23.89$

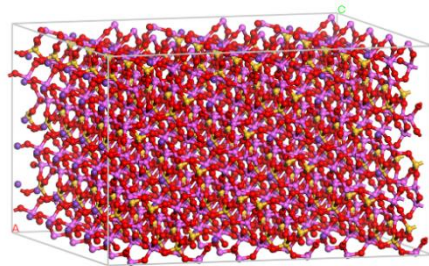


**Figure 2-9 An atomistic model of microcline substrate used for MD simulations.**

The bitumen-mineral interface system was constructed by attaching the confined bitumen layer to the mineral substrate. A vacuum layer of  $30 \text{ \AA}$  was then added to the top open surface of this confined bitumen layer. The interface model is illustrated in **Figure 2-10 (a)** where a microcline mineral was used as an example. Based on the interface model, the moisture effect was studied by adding water molecules at the bitumen-mineral interface. A thin confined layer of 200 water molecules was placed between bitumen and mineral layers to construct a bitumen-water-mineral model, as shown in **Figure 2-10 (b)**. The bitumen-water-mineral model assumed that water interrupted the bitumen-mineral interface and caused the debonding

between bitumen and mineral, which was considered as the major mechanism of the moisture-induced damage (stripping) in asphaltic mixtures (Kringos et al., 2008b, Kringos et al., 2008a). In the MD simulations, the interface models with or without water molecules were first subjected to a geometry optimisation, and then a dynamic equilibration run of 100 ps with an NVT ensemble was carried out to further optimise the model configuration.

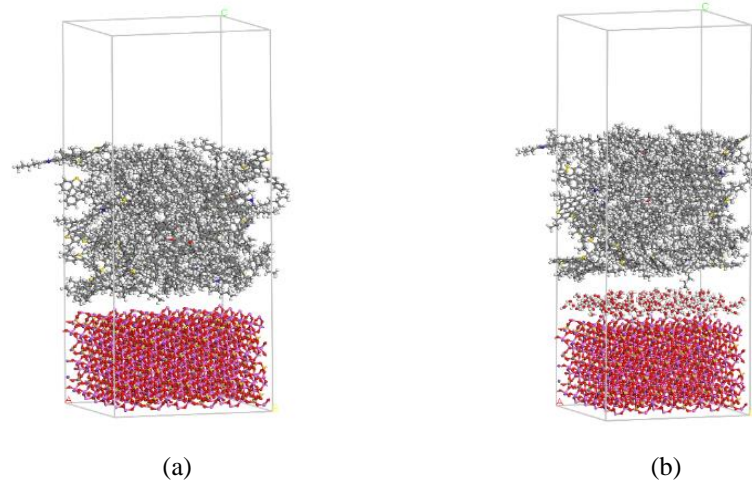


**Figure 2-10 Bitumen-mineral interface models for (a) the bitumen-minicrocline interface system and (b) bitumen-water-minicrocline interface system.**

### 2.7.3 Molecular interaction between bitumen and minerals

The nanostructures of bitumen-mineral interface for the four selected minerals after the MD simulations (namely, geometry optimisation and dynamic equilibration) are shown in **Figure 2-11**. The molecular interactions between bitumen and minerals can be intuitively observed based on the distance between bitumen and minerals which reflects the interfacial bonding performance between the two materials. A smaller distance between the two materials indicates a higher molecular interacting force and therefore a higher bonding strength for the bitumen-minerals system. This is due to the fact that the bitumen-minerals interactions are dominated by the non-bond terms including Coulomb electrostatic and van der Waals forces. They are both associated with the distance between atoms according to **Equation (2-4)** and **(2-5)**, which means that a smaller atomic separation distance leads to a higher atomic force. Thus, it can be found from **Figure 2-11** that the adhesion of microcline with bitumen is the strongest among the four minerals while quartz with bitumen has the weakest adhesion.

**Figure 2-12** shows the structures of bitumen-water-mineral interface systems for the four selected minerals after MD simulations. It can be observed that an obvious gap exists

between quartz or calcite and bitumen in the presence of water. This results from the degraded adhesion and debonding between quartz or calcite and bitumen when water diffuses into the interface. In comparison the albite-water-bitumen and microcline-water-bitumen models did not show any obvious gaps, indicating a strong adhesion between the minerals and bitumen. Thus, it can be concluded that the adhesion of the albite and microcline with bitumen is stronger than those of the quartz and calcite with bitumen under wet condition. These observations will be quantitatively validated by the adhesive bond energy determined from the MD simulations in the next sections.

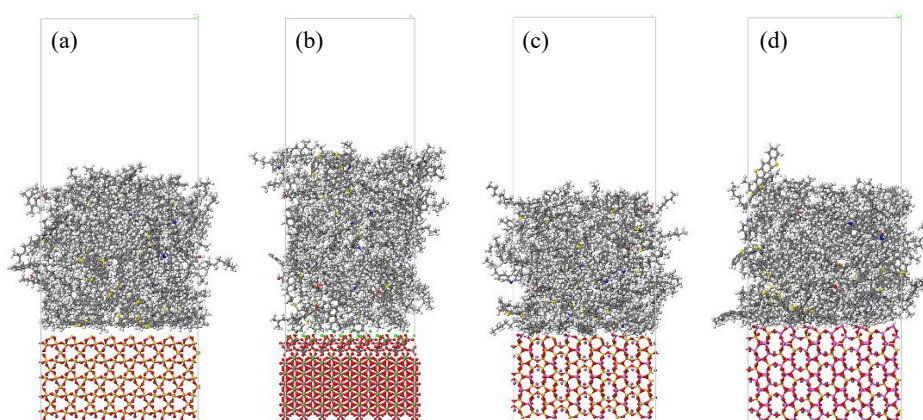


**Figure 2-11 Bitumen-mineral interface systems after MD simulations. (a) Quartz-bitumen model. (b) Calcite-bitumen model. (c) Albite-bitumen model. (d) Microcline-bitumen model.**

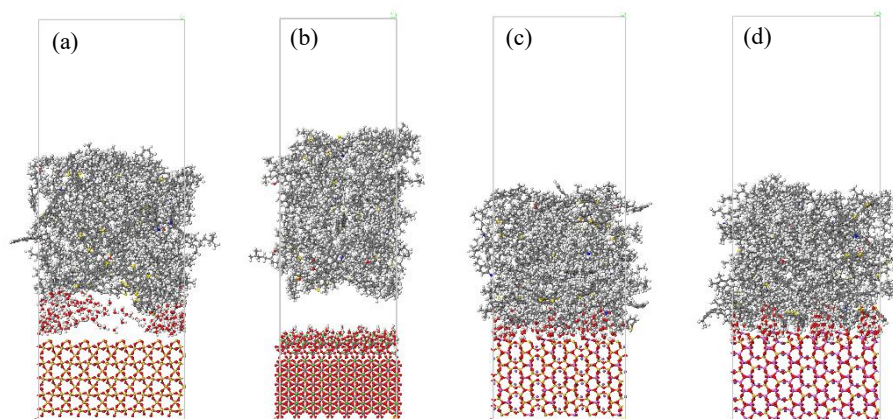


**Figure 2-12 Bitumen-water-mineral interface systems after MD simulations. (a) Quartz-water-bitumen model. (b) Calcite-water-bitumen model. (c) Albite-water-bitumen model. (d) Microcline-water-bitumen model.**

**Figure 2-12** also shows that the water molecules in quartz-water-bitumen model are interspersed in the gap between the quartz and bitumen, while for calcite-water-bitumen model, the water molecules have moved more closely to the calcite mineral surface. This may result from that the quartz has a symmetric molecular structure and exhibits weak adhesion force with water molecules. In contrast, the calcite has an unsymmetrical molecular structure with calcium ions, leading to a higher secondary atomic bond and a relatively higher adhesion force with water molecules.

#### 2.7.4 Calculation of adhesive bond energy

Adhesive bonding performance of bitumen is quantified by adhesive bond energy (i.e. work of adhesion), which is defined as the energy required to separate a unit area of an interface into two free surfaces in a vacuum (Little and Bhasin, 2006). It can be used to quantify the adhesive bonding performance of bitumen with minerals. The adhesive bond energy ( $W_{MB}$ ) is defined by **Equation (2-16)** using an interaction energy ( $\Delta E_{MB}$ ) which is derived from **Equation (2-17)** (Little and Bhasin, 2006, Xu and Wang, 2016b). Note that the parameters in **Equations (2-16)** and **(2-17)** are calculated based on the MD simulation results of the mineral-bitumen models and the mineral-water-bitumen models to obtain the adhesive bond energy in dry and wet conditions, respectively.

$$W_{MB} = \Delta E_{MB} / A \quad (2-16)$$

$$\Delta E_{MB} = E_M + E_B - E_{MB} \quad (2-17)$$

where  $W_{MB}$  is the adhesive bond energy between a mineral and bitumen;  $\Delta E_{MB}$  is the interaction energy between the mineral and bitumen;  $E_M$  and  $E_B$  are the potential energies of the mineral and bitumen at a thermodynamic equilibrium, respectively;  $E_{MB}$  is the total potential energy of mineral-bitumen system at the thermodynamic equilibrium; and  $A$  is the contact area of the interface between mineral and bitumen calculated using the Connolly area of mineral surface. The Connolly area can reflect the morphological feature of mineral and bitumen and thus more reasonably describe the interface contact area (Xu and Wang, 2016b).

#### 2.7.5 Adhesive bond energy in dry condition

**Table 2-8** lists the calculated interaction energy ( $\Delta E_{MB}$ ) and the adhesive bond energy ( $W_{MB}$ ) between minerals and bitumen in dry and wet conditions. In dry condition, the adhesive bond energy ( $W_{MB-dry}$ ) for the quartz-bitumen bond is 42.87 mJ/m<sup>2</sup>, while the adhesive bond energy ( $W_{MB-dry}$ ) of the calcite-bitumen bond is 57.13 mJ/m<sup>2</sup>. Thus, the adhesive bond energy ( $W_{MB-dry}$ ) between calcite and bitumen is greater than that between quartz and bitumen, which

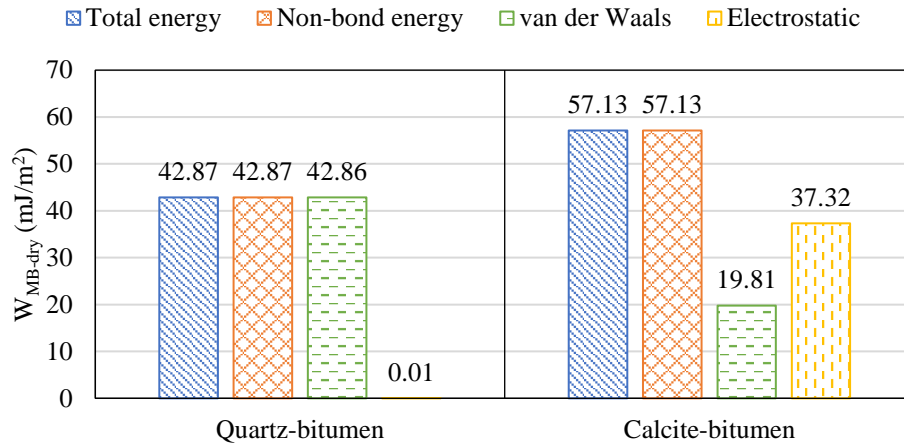
means the calcite-bitumen bond is stronger than the quartz-bitumen bond in dry condition. This agrees well with the laboratory measurements finding that limestone (in which calcite is the major component) shows larger adhesion strength with bitumen than granite with quartz as its main component (Yin et al., 2017). The ranking for the adhesion between the four minerals with bitumen is as follows: microcline > albite > calcite > quartz, as shown in **Table 2-8**. This indicates that mineral type has a significant impact on the adhesion between minerals and bitumen. Furthermore, it is noted that the adhesive bond energy ( $W_{MB-dry}$ ) for the microcline-bitumen bond (3241.55 mJ/m<sup>2</sup>) and the albite-bitumen bond (1257.25 mJ/m<sup>2</sup>) is much higher than that for the quartz-bitumen bond and the calcite-bitumen bond. This is because microcline and albite are strongly alkaline minerals with highly positive electronic charges. This finding verifies the existing experimental results that a mineral with an alkaline nature (with electro-positive charge) has a stronger adhesion with the weakly acidic bitumen than an acidic mineral (Chen et al., 2014, Abo-Qudais and Al-Shweily, 2007).

**Table 2-8 Adhesive bond energy between minerals and bitumen in dry and wet conditions.**

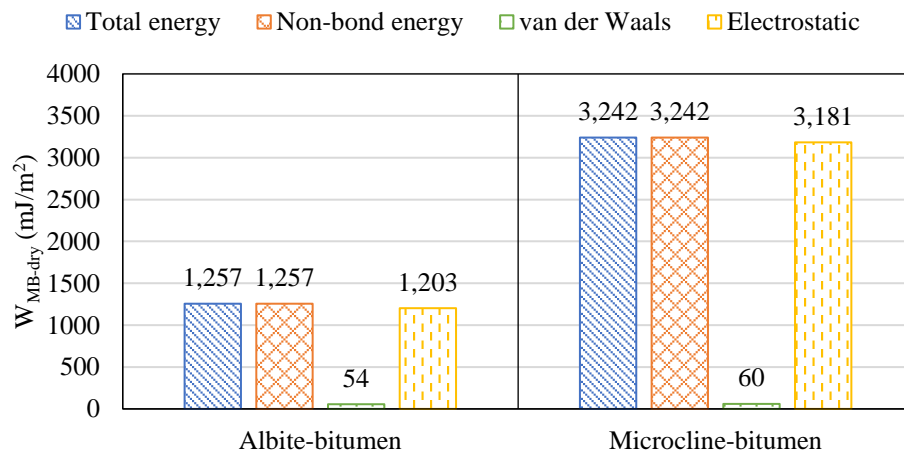
Models	$\Delta E_{MB-dry}$ (kcal/mol)	$W_{MB-dry}$ (mJ/m <sup>2</sup> )	$\Delta E_{MB-wet}$ (kcal/mol)	$W_{MB-wet}$ (mJ/m <sup>2</sup> )
Quartz-bitumen	230.29	42.87	40.58	7.56
Calcite-bitumen	250.54	57.13	41.07	9.36
Albite-bitumen	6361.98	1257.25	5234.93	1033.88
Microcline-bitumen	16520.00	3241.55	16346.78	3206.41

**Figure 2-13** shows the energy components that contribute to the adhesive bond energy ( $W_{MB-dry}$ ) between mineral and bitumen in the dry condition. It can be found that the total energy equals to the non-bond energy for the four mineral-bitumen systems (note that based on **Equation (2-1)**, the total energy = covalent energy + non-bond energy which includes van der Waals and electrostatic energy). This indicates that the adhesion between minerals and bitumen completely results from the non-bond interaction. The covalent interaction contributes little or nothing to the mineral-bitumen adhesive bond, indicating that no chemical bond is formed between minerals and bitumen. Within the non-bond energy components, the van der Waals interaction contributes to the main adhesion between quartz and bitumen. This is reasonable since the quartz is an acidic mineral, having a very weak or none electrostatic interaction with other materials. However, the electrostatic interaction becomes the major contribution for the adhesion between the bitumen and those alkali minerals (i.e., calcite, albite and microcline), as demonstrated in **Figure 2-13**. This finding is consistent with the previous study, in which Mirzababaei (2016) has reported that calcareous aggregates that have a high amount of calcite

show a strong electrostatic adhesion with bitumen. In summary, the adhesion between minerals and bitumen is attributed to non-bond interaction energy, where the major contribution results from van der Waals interaction for the acidic minerals like quartz and from the electrostatic interaction for the alkali minerals such as calcite, albite and microcline.



(a) Quartz-bitumen model and calcite-bitumen model.



(b) Albite-bitumen model and microcline-bitumen model.

**Figure 2-13 Contribution of non-bond components including van der Waals and electrostatic energy to total adhesive bond energy ( $W_{MB-dry}$ ) for different mineral-bitumen systems.**

### 2.7.6 Adhesive bond energy in wet condition

In wet condition, the adhesive bond energy ( $W_{MB-wet}$ ) between mineral and bitumen is also calculated, as shown in **Table 2-8**. The adhesive bond energy ( $W_{MB-wet}$ ) of the quartz-

bitumen bond is 7.56 mJ/m<sup>2</sup>, while the adhesive bond energy ( $W_{\text{MB-wet}}$ ) of the calcite-bitumen bond is 9.36 mJ/m<sup>2</sup>. It is concluded that calcite-bitumen bond is still stronger than the quartz-bitumen bond even in the presence of water. This is in agreement with the previous study from Lu and Wang (2017) who found that calcite was more prone to adsorb bitumen than quartz in the wet condition. The microcline-bitumen model has the largest adhesive bond energy ( $W_{\text{MB-wet}}$ ) of 3206.41 mJ/m<sup>2</sup> and the adhesive bond energy ( $W_{\text{MB-wet}}$ ) of the albite-bitumen model is 1033.88 mJ/m<sup>2</sup>. The ranking for the adhesion between the four minerals and bitumen in wet condition remains unchanged from that in the dry condition, which is: microcline > albite > calcite > quartz. However, it can be found that the moisture reduces the adhesion between minerals and bitumen and the decrease of the adhesive bond energy between minerals and bitumen from dry to the wet condition is different depending on the mineral types.

To quantify the susceptibility of the mineral-bitumen adhesion to the presence of water, adhesion degradation percentage ( $R_{\text{AD}}$ ) from dry to wet conditions is proposed using the adhesive bond energy. In this study, the degradation ratio ( $R_{\text{AD}}$ ) is calculated as the difference of the adhesive bond energy for the mineral-bitumen model in dry and wet conditions divided by the adhesive bond energy in the dry condition, as shown in **Equation (2-18)**. A higher value of ( $R_{\text{AD}}$ ) means a greater degradation of the mineral-bitumen adhesion and indicates a higher susceptibility of the mineral-bitumen interface to water.

$$R_{\text{AD}} = (W_{\text{MB-dry}} - W_{\text{MB-wet}}) / W_{\text{MB-dry}} \quad (2-18)$$

where  $W_{\text{MB-dry}}$  is the adhesive bond energy between mineral and bitumen in the dry condition, and  $W_{\text{MB-wet}}$  is the adhesive bond energy between mineral and bitumen in the wet condition.

**Figure 2-14** shows the adhesion degradation ratio ( $R_{\text{AD}}$ ) for the four interface models. The quartz-bitumen model has a  $R_{\text{AD}}$  value of 82%, which is very close to that of the calcite-bitumen model (84%). However, the  $R_{\text{AD}}$  values for the albite-bitumen and microcline-bitumen models are 18% and 1%, respectively, which are much smaller than those of the quartz-bitumen and calcite-bitumen models. This is due to the fact that the highly alkali minerals such as microcline and albite induce very high and stable electrostatic interactions with bitumen as shown in **Figure 2-13**, which can little be reduced by the presence of water. This result proves that the susceptibility of the adhesion to moisture depends on the mineral types and highly alkali minerals provide a stronger adhesion stability and less moisture susceptibility than weak alkali or acidic minerals.

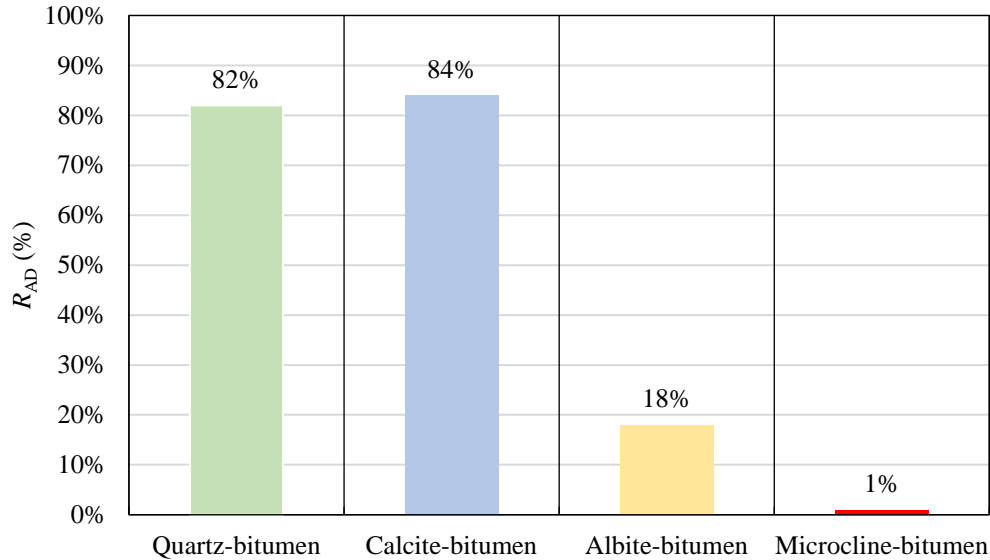


**Figure 2-14 Adhesion degradation ratio ( $R_{AD}$ ) for four mineral-bitumen systems.**

## 2.8 Conclusions

In this chapter, the bonding performance of bitumen is modelled using molecular dynamics (MD) simulation and the effect of aggregate minerals on the bitumen bonding performance is investigated at the nanoscale. The molecular models of the bitumen are built based on saturates, aromatics, resins and asphaltenes (SARA) four fractions. Based on the results of MD simulations, the cohesive bond energy of bitumen is calculated. Contact angle measurements are conducted to validate the predicted results from MD simulations. The molecular models of bitumen-mineral interface systems are constructed by using four representative minerals (namely quartz, calcite, albite and microcline) in aggregates to investigate the effects of the minerals on adhesive bonding performance of the bitumen. The adhesive bonding performance is quantified by adhesive bond energy, which is defined as the energy required to separate a unit area of the bitumen-mineral interface. The main findings from this study are as follows:

- (1) The predicted cohesive bond energy of bitumen based on MD simulations agrees well with the measured results from the contact angle measurements. The cohesive bond energy predicted at the nanoscale can be used as a fundamental and scale-independent input for the mechanics modelling of bitumen fatigue cracking at the next higher scale.
- (2) The adhesive bonding performance of the bitumen with minerals strongly depends on the chemical and mineralogical properties of the minerals. The adhesive bonding

performance between the bitumen and minerals is attributed to non-bond interaction energy, where the major contribution is from van der Waals interaction for the acidic minerals like quartz while from the electrostatic interaction for the alkali minerals such as calcite, albite and microcline.

- (3) For both dry and wet conditions, the calcite-bitumen bonding performance is stronger than the quartz-bitumen bonding performance, and the adhesion of the four minerals with bitumen is ranked as: microcline > albite > calcite > quartz. The moisture can reduce the adhesion between bitumen and minerals by 82%, 84%, 18% and 1% for the quartz, calcite, albite and microcline, respectively.

# Chapter 3 Nanoscale Modelling of Oxidative Ageing Effect on Bitumen Bonding Performance\*

## 3.1 Overview

This chapter aims to investigate the effects of oxidative ageing on the bitumen bonding performance using the molecular dynamics (MD) simulations at the nanoscale. The molecular models of the aged bitumen with saturates, aromatics, resins and asphaltenes (SARA) four fractions are built according to the oxidation formulation of the bitumen. The MD simulations are performed to calculate the cohesive bond energy of the aged bitumen, which is validated by the contact angle measurements. The molecular models of the aged bitumen-mineral interface systems with quartz, calcite, albite and microcline four minerals are constructed to investigate the effects of the oxidative ageing on adhesive bonding performance of the bitumen with different minerals. Adhesive bond energy is computed to quantify the adhesive bonding performance in dry and wet conditions.

The results show that the oxidised products (i.e., ketone and sulfoxide) strengthen the intermolecular bonding performance, resulting in molecular aggregation and physical hardening of the aged bitumen, which could eventually lead to block cracking. The predicted cohesive bond energy of the aged bitumen from the MD simulations has a good agreement with the measured result from the contact angle measurements. The predicted cohesive bond energy of the aged bitumen at the nanoscale can be used as a fundamental and scale-independent input for the cohesive debonding modelling for fatigue cracking of the aged bitumen at higher scale.

In dry condition, when the bitumen becomes oxidised, the adhesive bonding performance of bitumen-acidic minerals (quartz) is dominated by van der Waals interaction which decreases due to the increased bitumen-quartz intermolecular distance caused by the aggregated bitumen molecules during the ageing. In comparison, the interfacial adhesion of bitumen-strong alkali minerals (albite and microcline) is dominated by electrostatic energy which increases due to the higher polarity introduced by the oxidised products. For the bitumen-weak alkali mineral (calcite), the interfacial adhesion is attributed to both electrostatic energy

---

\* Reprinted with permission from Elsevier: **Y. Gao**, Y. Zhang, Y. Yang, J. Zhang, F. Gu. (2019). Molecular dynamics investigation of interfacial adhesion between oxidised bitumen and mineral surfaces. *Applied Surface Science* 479, 449-462.

and van der Waals energy, where compared to the virgin bitumen, the electrostatic energy becomes lower for the lightly-oxidised bitumen due to the increased bitumen-mineral distance but becomes higher for the heavily-oxidised bitumen due to the higher polarity.

In wet condition, water is the dominating factor that affects (weakens) the interfacial adhesion between the bitumen and the acidic minerals (quartz), and the oxidative ageing of the bitumen is the major factor that affects (strengthens) the interfacial adhesion between the bitumen and the strongly alkaline minerals (albite and microcline). For the weak alkali minerals (calcite), both the water and the bitumen ageing can significantly affect the interfacial adhesion.

### **3.2 Introduction**

Bitumen's durability is significantly affected by oxidative ageing where bitumen molecules react with atmospheric oxygen (Petersen, 2000). The oxidative ageing can cause chemical changes of the bitumen including the formation of new molecular functional groups such as ketone and sulfoxide, which have a considerable impact on the physical and mechanical properties of the bituminous materials, including viscoelastic properties, cohesive and adhesive bond strengths, and fracture properties (Knorr Jr et al., 2002, Das et al., 2015).

A number of experimental studies have been performed to understand the bitumen ageing at the micro and macro dimensions in the pavement engineering applications. Rheological tests were developed to characterize and quantify the ageing behaviour of the bitumen (Andersen and Birdi, 1991, Jennings et al., 1993, Collop et al., 2007, Houston et al., 2007). Recently, the ageing effects of bitumen on the rheology (Qin et al., 2014), intrinsic healing (Bhasin et al., 2011), and surface energy and bonding property (Yi et al., 2018) were also evaluated using a variety of material characterisation technologies including Dynamic Shear Rheometer (DSR), Fourier Transform Infrared Spectroscopy (FTIR) and Atomic Force Microscopy (AFM) tests. It has been recognised that the oxidation causes the hardening of the bitumen, leading to a higher cracking susceptibility of the asphalt pavements (Petersen, 2009). While these experimental studies at the microscale and macroscale were commendable, they have not fully addressed the oxidative ageing effects on the thermodynamic properties (such as intermolecular energies, interactions and cohesion) of bitumen at the molecular level.

Molecular dynamics (MD) simulation is advantageous over the traditional laboratory-based methods in understanding the nanostructure and properties of the bitumen at the molecular scale. Several studies using MD simulation have been carried out to investigate the physical property changes of the bitumen from the perspectives of chemical compositional or

molecular structural changes due to the oxidative ageing. Tarefder and Arisa (2011) determined the changes in thermodynamic properties of asphaltene and resin in bitumen before and after oxidative ageing based on the defined molecule structures (Groenzin and Mullins, 2000, Murgich et al., 1996). Pan et al. (2012) used the three-component model bitumen system to explore the molecular-scale processes of bitumen oxidation in the quantum chemistry (QC)-based environment and analysed the hardening mechanisms of bitumen's oxidation. Pan and Tarefder (2016) investigated the density, bulk modulus, viscosity and mechanical property changes of the twelve-component AAA-1 model bitumen system before and after oxidative ageing at room temperature (298 K). Xu and Wang (2017) used the twelve-component AAA-1 model bitumen system to analyse the intermolecular interactions of virgin and aged bitumen and to study the ageing effects on self-healing and moisture damage of bitumen due to oxidation.

However, limited work has been focused on the effects of bitumen oxidative ageing on the bonding performance of the bitumen at the molecular level, particularly when minerals and water are present. In **Chapter 2**, the MD simulation has been used to investigate the adhesive bonding performance of the bitumen with four different minerals. It was found that the adhesive bonding performance of the bitumen is primarily attributed to van der Waals force for acidic minerals (quartz) and to electrostatic interaction for alkali minerals (calcite, albite and microcline). The adhesive bond energy was greater for the alkali minerals than that of the acidic minerals. It is unknown how the oxidative ageing of the bitumen will alter the aforementioned findings or how water will affect the bonding performance of the aged bitumen with different mineral surfaces. Therefore, there is a need for understanding the changes of the bitumen bonding performance at the nanoscale when the bitumen becomes oxidatively aged to different levels and when water is present, which is investigated in this chapter.

The objective of this chapter is to investigate the effects of oxidative ageing on the bitumen's bonding performance using the MD simulations at the nanoscale. The molecular models of the aged bitumen using the twelve-component model are constructed based on the oxidation mechanism of the bitumen. Cohesive bond energy of the aged bitumen is calculated by the MD simulation results. Laboratory tests (i.e., contact angle measurements) are conducted to validate the predicted cohesive bond energy. The molecular models of the aged bitumen-mineral interface systems are built to investigate the effects of the oxidative ageing on adhesive bonding performance of the bitumen that is quantified by the adhesive bond energy in dry and wet conditions.

### 3.3 Bitumen Oxidative Ageing

Bitumen composition changes when it is exposed to atmospheric oxygen. New chemical functional groups are formed in bitumen, which is responsible for the increase of the viscosity (Petersen, 2000). Extensive experimental studies have been conducted to investigate the mechanism of bitumen ageing due to oxidation. It was found that there are two types of the readily oxidizable locations in bitumen. One is the carbon atom adjacent to an aromatic ring. The hydrogen atom attached to the benzylic carbon atom is displaced by oxygen to form a ketone. The other is sulphide that reacts with oxygen to form sulfoxide. The sulfoxides formed at sulphur atoms and ketones formed at benzylic carbon atoms have been identified as the major oxidation products (Petersen and Harnsberger, 1998, Petersen and Glaser, 2011).

Asphaltene and resin contain the chemically functional groups of oxygen, sulphur and nitrogen atoms, which results in their high polarity. Therefore, they have strong interaction and are highly reactive with the electronegative oxygen. King and Corbett showed that aromatic was slightly oxidised and saturate were relatively inert to the reaction with oxygen due to the lack of sensitive functional groups (King and Corbett, 1969). Based on the oxidation mechanism discussed above, the ketones and sulfoxides were added to the possible oxidised sites of the twelve-component bitumen model to build the oxidised bitumen molecular models due to ageing. **Figures 3-1, 3-2 and 3-3** show the molecular structures of the oxidised asphaltene, resin and aromatic fractions in the aged bitumen, respectively (Pan and Tarefder, 2016). The saturate fraction has been assumed to remain unchanged during the oxidative ageing.

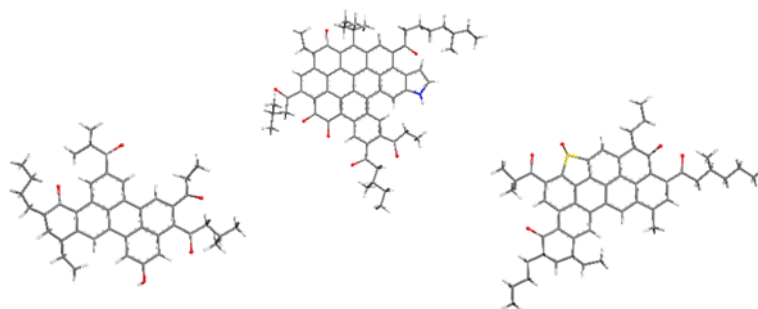


**Figure 3-1 Molecular structures of oxidised asphaltene fraction.**

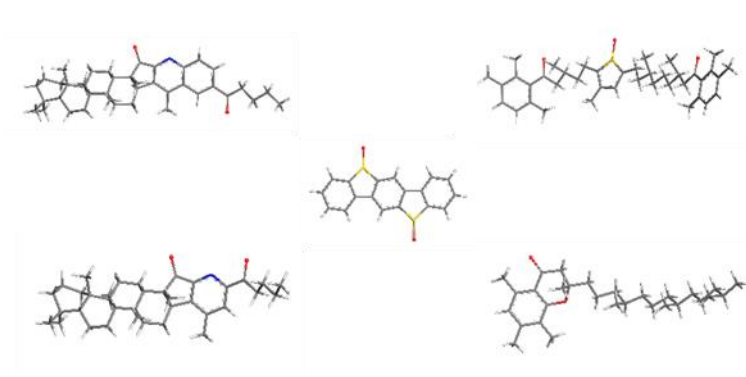


**Figure 3-2 Molecular structures of oxidised resin fraction.**

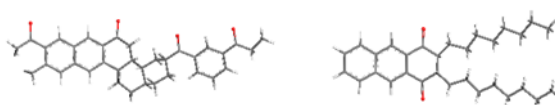


**Figure 3-3 Molecular structures of oxidised aromatic fraction.**

### 3.4 Molecular Models of Aged Bitumen

Using the molecular models of the oxidised bitumen components, the molecular models of the aged bitumen were constructed based on the twelve-component model. Two oxidation levels, namely lightly-oxidised bitumen (LOB) and heavily-oxidised bitumen (HOB), are considered in this study by assigning a different number of the oxidised molecules in a model bitumen system, as shown in **Table 3-1**. The number of the oxidised molecules in the lightly-oxidised bitumen is half of that in the heavily-oxidised bitumen. This method has been employed to model the ageing of bitumen at different oxidation levels in the previous studies (Tarefder and Arisa, 2011, Pan and Tarefder, 2016).

To build the aged model bitumen system, the molecules of the oxidised bitumen components shown in **Table 3-1** were put into a cubic simulation box to form a bulk bitumen model. A geometry optimisation process for 5000 iterations was first conducted to minimize the system energy. The system was then subjected to a molecular dynamic (MD) equilibration under an NPT ensemble at a temperature of 298 K and a pressure of 1.0 atm for 100 ps with 1.0 fs time step to obtain a stable system volume. Subsequently, an NVT ensemble at 298 K was used to further equilibrate the system for 100 ps to generate an equilibrated model bitumen system with stable volume and energy fluctuation. **Figure 3-4** shows the equilibrated structure

of the bulk model for the aged bitumen at different oxidation levels (a virgin bitumen model is also presented here to illustrate the effect of oxidative ageing). A surface film model of the aged bitumen was constructed by adding a vacuum layer on the bulk model. The aged film model was subjected to the energy minimization run followed by 200 ps of MD simulation with an NVT ensemble at 298 K. The equilibrated film model and the developed bulk bitumen model will be used to calculate the cohesive bond energy of the aged bitumen later.

**Table 3-1 Compositions of aged bitumen molecular model at different oxidation levels used for MD simulations.**

SARA fractions	Molecules in model	Molecular formula	Number of molecules		
			VB <sup>a</sup>	LOB <sup>b</sup>	HOB <sup>c</sup>
Saturate	Squalane	C <sub>30</sub> H <sub>62</sub>	4	4	4
	Hopane	C <sub>29</sub> H <sub>50</sub>	4	4	4
Aromatic (Naphthene aromatic)	PHPN	C <sub>35</sub> H <sub>44</sub>	11	6	0
	Oxidised PHPN	C <sub>35</sub> H <sub>36</sub> O <sub>4</sub>	0	5	11
	DOCHN	C <sub>30</sub> H <sub>46</sub>	13	7	0
	Oxidised DOCHN	C <sub>30</sub> H <sub>42</sub> O <sub>2</sub>	0	6	13
Resin (Polar aromatic)	Quinolinohopane	C <sub>40</sub> H <sub>59</sub> N	4	2	0
	Oxidised Quinolinohopane	C <sub>40</sub> H <sub>55</sub> NO <sub>2</sub>	0	2	4
	Thioisorenieratane	C <sub>40</sub> H <sub>60</sub> S	4	2	0
	Oxidised Thioisorenieratane	C <sub>40</sub> H <sub>56</sub> SO <sub>3</sub>	0	2	4
	Benzobisbenzothiophene	C <sub>18</sub> H <sub>10</sub> S <sub>2</sub>	15	8	0
	Oxidised Benzobisbenzothiophene	C <sub>18</sub> H <sub>10</sub> S <sub>2</sub> O <sub>2</sub>	0	7	15
	Pyridinohopane	C <sub>36</sub> H <sub>57</sub> N	4	2	0
	Oxidised Pyridinohopane	C <sub>36</sub> H <sub>53</sub> NO <sub>2</sub>	0	2	4
	Trimethylbenzene-oxane	C <sub>29</sub> H <sub>50</sub> O	5	3	0
	Oxidised Trimethylbenzene-oxane	C <sub>29</sub> H <sub>48</sub> O <sub>2</sub>	0	2	5
	Asphaltene	Asphaltene-phenol	C <sub>42</sub> H <sub>50</sub> O	3	2
Oxidised Asphaltene-phenol		C <sub>42</sub> H <sub>46</sub> O <sub>5</sub>	0	1	3
Asphaltene-pyrrole		C <sub>66</sub> H <sub>81</sub> N	2	1	0
Oxidised Asphaltene-pyrrole		C <sub>66</sub> H <sub>67</sub> NO <sub>7</sub>	0	1	2
Asphaltene-thiophene		C <sub>51</sub> H <sub>62</sub> S	3	2	0
Oxidised Asphaltene-thiophene		C <sub>51</sub> H <sub>54</sub> SO <sub>5</sub>	0	1	3

<sup>a</sup> VB, virgin bitumen; <sup>b</sup> LOB, the lightly-oxidised bitumen; <sup>c</sup> HOB, the heavily-oxidised bitumen.

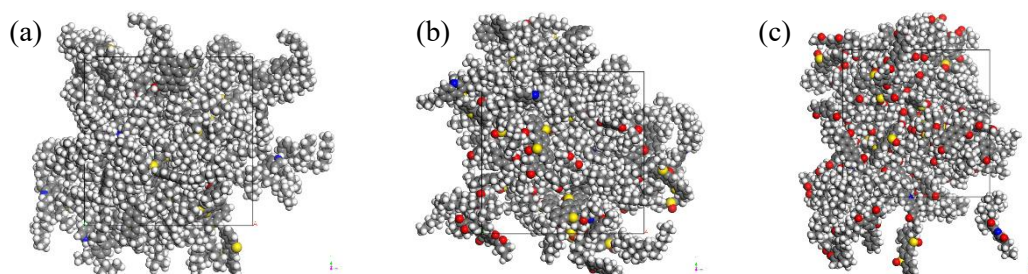


**Figure 3-4 Bitumen bulk models at different oxidation levels. (a) Virgin model. (b) Lightly-oxidised (LO) model. (c) Heavily-oxidised (HO) model.**

### 3.5 Materials and Laboratory Tests

The aged bituminous binders were tested in this section to determine their cohesive bonding performance. The unmodified bitumen 40/60 and the polymer modified bitumen X-70 used in **Section 2.5** were first aged by Thin-Film Oven Test (TFOT) that was conducted at the temperature of 163 °C for 5 hours. Following the procedure for the unaged bitumen binders shown in **Section 2.5**, the aged bitumen samples were prepared and their contact angles were measured using the sessile drop (SD) method. **Table 3-2** shows the measured contact angles between the aged bitumen and the liquids.

**Table 3-2 Contact angles between aged bitumen and liquid probes (°).**

Bitumens	Distilled Water (W)	Ethylene glycol (EG)	Formamide (F)
Aged 40/60	106.73±0.78	82.23±0.28	90.40±0.55
Aged X-70	102.57±0.89	79.74±0.22	88.38±0.50

Based on the measured contact angles, the surface energy components of the aged bitumen were obtained using **Equation (2-13)**, as shown in **Table 3-3**. According to **Equation (2-14)**, the cohesive bond energy of the aged bitumen can be determined. **Figure 3-5** shows the measured cohesive bond energy of the aged bitumen.

**Table 3-3 Surface energy components of aged bitumen (mJ/m<sup>2</sup>).**

Bitumens	$\Gamma$	$\Gamma^{LW}$	$\Gamma^{AB}$	$\sqrt{\Gamma^+}$	$\sqrt{\Gamma^-}$
Aged 40/60	10.65	7.47	3.182	1.63	0.976
Aged X-70	12.21	7.338	4.876	1.708	1.428

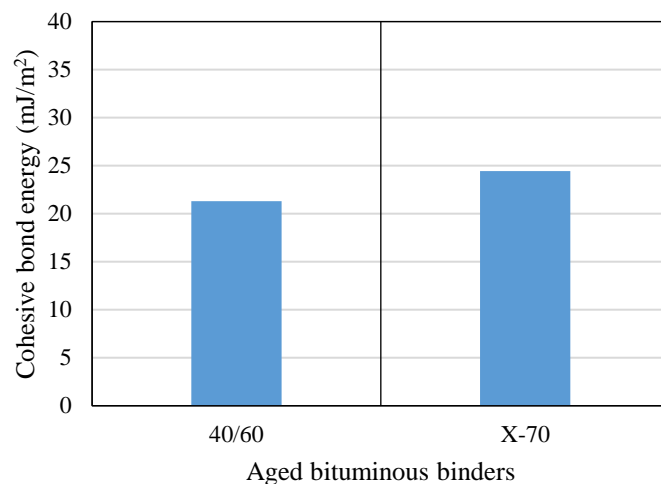


**Figure 3-5 Measured cohesive bond energy of aged bituminous binders.**

### 3.6 Cohesive Bonding Performance of Aged Bitumen

#### 3.6.1 Hardening mechanism of the aged bitumen

To validate the molecular simulation and analyse the hardening mechanisms of the bitumen due to oxidative ageing at the nanoscale, the thermophysical properties of the aged bitumen were calculated including density, cohesive energy density (CED) and fraction of free volume (FFV).

The density of the bulk bitumen model at different oxidation levels was calculated at the temperature of 298 K (25 °C) based on MD simulations. **Figure 3-6** shows the bitumen density changes due to oxidative ageing. The bitumen density became higher after oxidative ageing, where the density was 1.016 g/cm<sup>3</sup> for the lightly-oxidised bitumen and 1.048 g/cm<sup>3</sup> for the heavily-oxidised bitumen and the density was 0.981 g/cm<sup>3</sup> for the virgin (unaged) bitumen. This trend is in good agreement with the simulation results from Pan and Tarefder (2016) as well as the experimental results for the virgin and aged PG 58-28 bitumen (Jones, 1993). It can also be seen from **Figure 3-6** that the density change for simulation results before and after oxidative ageing was greater than that of the experimental results. This might be because the loss of volatile components due to the volatilisation during the ageing process was not considered in the simulation.

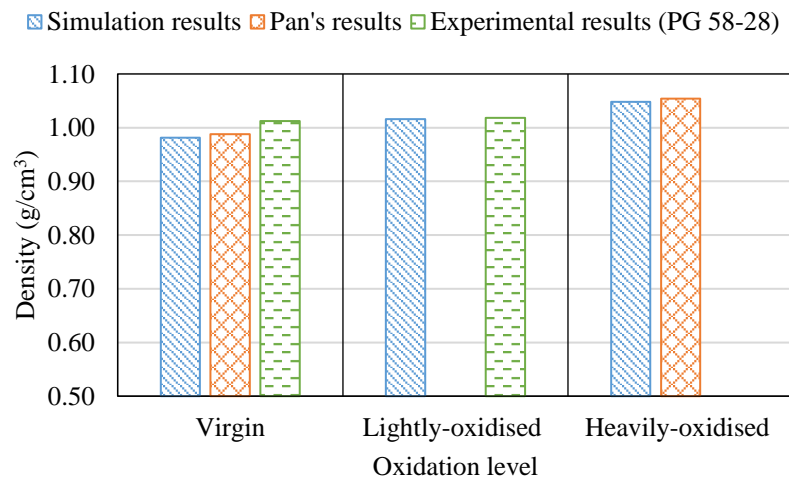


**Figure 3-6 Density of bulk bitumen model at different oxidation levels.**

Cohesive energy density (CED) is used to calculate an energy per unit volume to evaluate the intermolecular bonding performance of a bulk bitumen model. The cohesive energy is attributed to the non-bonded interactions including van der Waals and electrostatic

interactions. **Figure 3-7** shows the calculated CED for the bulk bitumen model at different oxidation levels including the van der Waals and electrostatic components. It was found that the CED value increased with the increasing oxidation level and the majority of the CED resulted from van der Waals interaction. This indicates that the intermolecular bonding in oxidised bitumen is stronger than that in the virgin bitumen. This is mainly due to that, when the oxygen atoms are introduced to bitumen, both the molecular weight and the polarity of the oxidised bitumen became higher than that of the virgin bitumen, which results in a greater van der Waals and electrostatic intermolecular interactions in the bulk bitumen model.

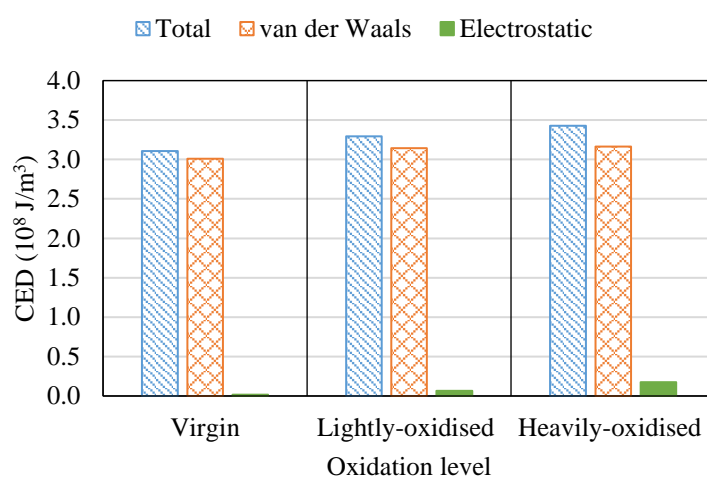


**Figure 3-7 Cohesive energy density (CED) of bulk bitumen model at different oxidation levels including two components, namely van der Waals and electrostatic intermolecular interactions.**

The fraction of free volume (FFV) is used as a measure of the volume that has not been occupied by the molecules and to determine the percentage of volume available in a bulk bitumen model. **Figure 3-8** shows the calculated FFV of the bulk bitumen model at different oxidation levels. The FFV value for the oxidised bitumen (approximately 37.5% for both the lightly-oxidised bitumen and the heavily-oxidised bitumen) was lower than that of virgin bitumen (38.2%). This means that the oxidised bitumen is agglomerate further than the virgin bitumen due to a higher molecular weight and polarity of the oxidised bitumen system.

The lower FFV for the oxidised bitumen is consistent with the higher density and CED, which demonstrates a stronger intermolecular bonding in the oxidised bitumen system that leads to a further shrinkage of the bitumen system when oxygen is present in the material. The analysis of the thermophysical properties of the aged bitumen from the molecular perspective explains the physical hardening happened during the oxidative ageing which was recognised

through a number of experimental studies at the macroscopic level (Petersen, 2009). This also demonstrates the molecular simulation method is suitable for describing the ageing behaviour of the bitumen due to oxidation and can be further applied for the investigation of the oxidative ageing effects on the bitumen bonding performance.

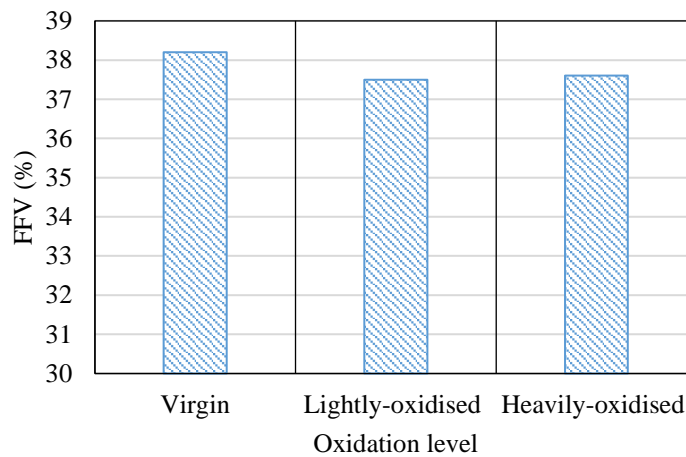


**Figure 3-8 Fraction of free volume (FFV) of bulk bitumen model at different oxidation levels.**

### 3.6.2 Calculation of cohesive bond energy

Based on the MD simulation results of the bulk model and the film model of the aged bitumen described in **Section 3.4**, the surface energy of the aged bitumen was first calculated using **Equation (2-15)**. According to **Equation (2-14)**, the corresponding cohesive bond energy of the aged bitumen can be obtained from their surface energy results. **Table 3-4** summarises the predicted cohesive bond energy from the MD simulations for the molecular models of the lightly-oxidised bitumen (LOB) and the heavily-oxidised bitumen (HOB) and one additional oxidised bitumen (AOB) molecular model with different SARA mass fractions. To validate the simulation results, the predicted values was compared to the measured results for the aged bitumen samples from laboratory tests shown in **Section 3.5** and the experimental data reported in the literatures (Howson et al., 2011), as shown in **Table 3-4**. It can be seen that the predicted results from the MD simulations lie within the range of the experimental values and SARA fractions have a significant effect on the MD simulation results. This again proves that the cohesive bond energy predicted based on MD simulations at the nanoscale can be identified as an input for the mechanistic modelling of bitumen at the higher scale. To better simulate the aged bitumens, more specific molecular models should be built using actual measurements of SARA mass fractions in future study.

**Table 3-4 Cohesive bond energy of aged bitumen from MD simulations.**

Molecular models	SARA mass fractions (%)				Simulation results (mJ/m <sup>2</sup> )	Experiment results (mJ/m <sup>2</sup> )
	S	A	R	A		
LOB	10.7	32.2	39.8	17.3	40.47	36.96-57.60 (Howson et al., 2011) 21.30 (Aged 40-60) 24.42 (Aged X-70)
HOB	10.3	32.4	39.6	17.7	39.13	
AOB	11.6	36.4	44.3	7.7	20.54	

### 3.7 Adhesive Bonding Performance of Aged Bitumen

Molecular mechanisms of the oxidative ageing effects on the adhesive bonding performance of bitumen are investigated using the MD simulations in this section.

#### 3.7.1 Molecular models of aged bitumen-mineral interface

In order to construct the aged bitumen-mineral interface system models, the mineral substrate models and the aged bitumen layer models are first built following the method described in **Sections 2.7**. Quartz, calcite, albite and microcline are selected to build the mineral substrate models. The four types of minerals commonly exist in the aggregates such as granite, limestone and basalt used for constructing asphalt concrete. To model the mineral substrate, the crystal unit cell was firstly cleaved along the Miller plane (100) to expose the corresponding surface and then this surface was extended to create an orthogonal mineral supercell with the periodic boundary condition in all three dimensions. The aged bitumen layer was built with the same width and length as the mineral substrate. The layer model was subjected to a geometry optimisation followed by an MD simulation of 100 ps with NVT ensemble to equilibrate the system.

Once the aged bitumen layer and mineral substrate models were obtained, the aged bitumen-mineral interface system models could be constructed. The aged bitumen layer was firstly combined with the mineral substrate and then a vacuum layer of 30 Å was placed over the top surface of the bitumen layer in order to avoid interaction across the mirror image in the z-direction. For the wet interface model, a layer containing 200 water molecules was added at the aged bitumen-mineral interface to form an aged bitumen-water-mineral interface system. The dry and wet interface systems for the heavily-oxidised bitumen with albite substrate are illustrated in **Figures 3-9(a)** and **(b)**. After a geometry optimisation process, the interface systems were subjected to dynamics equilibration with an NVT ensemble for 100 ps to reach the stable state. The simulation time was sufficiently long to reach an equilibration, which was

demonstrated by a stable energy of the system being reached, as shown in **Figure 3-9(c)**. After the system became equilibrium, an additional 400 ps simulation under an NVT ensemble was then performed for the subsequent trajectory analysis.

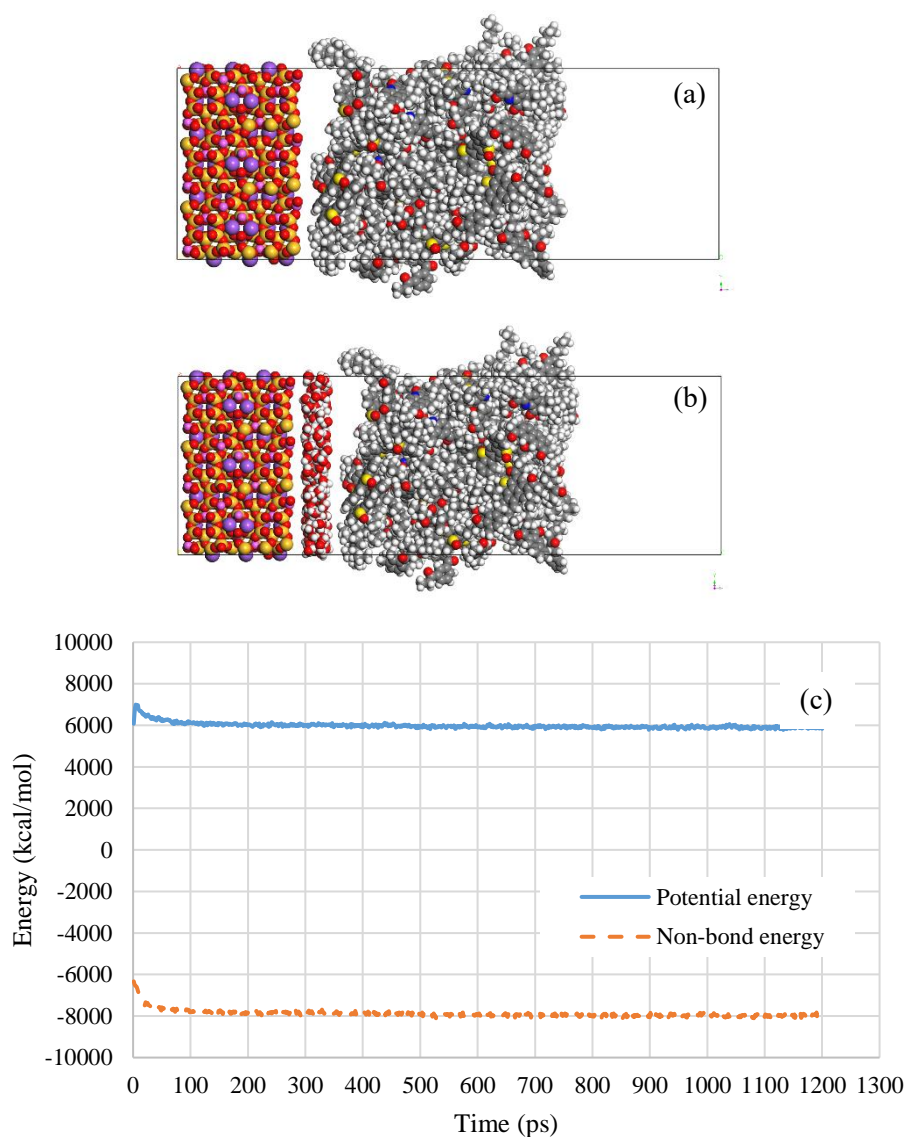


**Figure 3-9 Aged bitumen-mineral interface models and simulations. (a) The heavily-oxidised bitumen-albite model. (b) The heavily-oxidised bitumen-water-albite model. (c) The change of energy during the simulations.**

### 3.7.2 Molecular structure of bitumen on mineral surfaces

Bitumen is regarded as a colloidal structure where asphaltene is dispersed in the maltene composed of resins, aromatics and saturates (Lesueur, 2009, Wang et al., 2015c). **Figure 3-10** illustrates the nanostructures of the bitumen at the heavily-oxidised bitumen-quartz

interface and the heavily-oxidised bitumen-water-quartz interface obtained from the last frame of simulation trajectories, respectively. It can be observed that within the interfacial systems, asphaltene molecules (in blue colour) were dispersed in the maltene medium. Asphaltenes tended to form the nano-aggregation structures without a continuous network. This type of structure is also referred to bitumen sol-gel structure, which has been reported in prior experimental and simulation studies (Lesueur, 2009, Wang et al., 2015c).

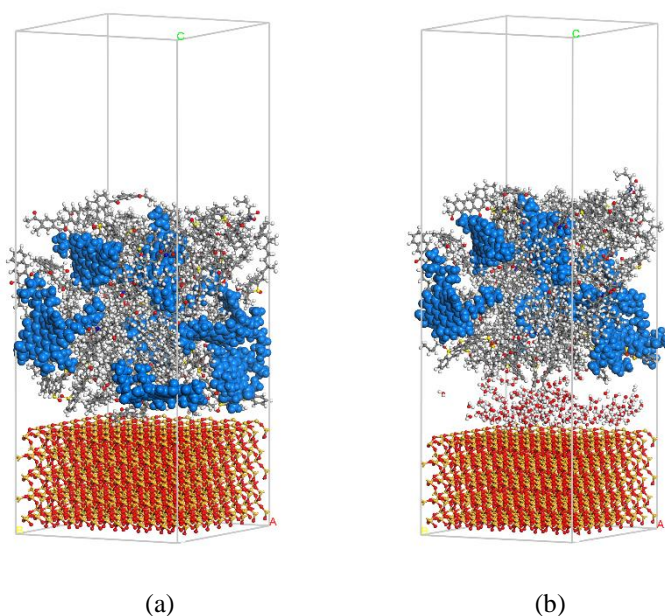


**Figure 3-10 Nanostructures of bitumen at (a) heavily-oxidised bitumen-quartz interface and (b) heavily-oxidised bitumen-water-quartz interface obtained from MD simulations.**

To characterise the molecular arrangement and mobility of bitumen on the mineral surfaces, the radial distribution function (RDF) and mean squared displacement (MSD) of the asphaltenes were analysed, respectively. RDF describes the probability of finding a particle at a radial distance  $r$  away from a reference particle in a system of particles. In this study, the intermolecular distance was calculated based on the asphaltene molecule's centre of mass. The trajectory obtained from the last 200 ps of MD simulations under an NVT ensemble was applied for RDF analysis. **Figure 3-11** shows the RDFs of asphaltene-asphaltene pair in the bitumen-microcline interfacial models at different oxidation levels. Radial distances corresponding to the first peak value of RDF curves for asphaltene-asphaltene pair in bulk bitumen model and four interfacial models at different oxidation levels were summarised in **Table 3-5**. In the bulk bitumen models, the first peak value of RDF for the virgin bitumen occurred around 10-11 Å, while the distance became smaller for the heavily-oxidised bitumen (8-9 Å) and the lightly-

oxidised bitumen (4-5 Å). This indicates that the oxidative ageing strengthened the bitumen's aggregation due to the higher molecular polarity, which is consistent with the finding in **Section 3.6.1**. In the interfacial models, it can be found from **Table 3-5** that the mineral surfaces had a significant influence on the nano-aggregation structure of the bitumen, especially under the oxidation conditions. The aggregation of the bitumen on the quartz surface was consistent with that of the bulk bitumen because of the very weak interaction between quartz and bitumen. The aggregation of the oxidised bitumen on the calcite surface was weakened since calcite attracted a part of the oxidised bitumen from the bulk bitumen due to the slightly strong electrostatic interaction. While for albite and microcline the very strong electrostatic interaction with bitumen has significantly strengthened the aggregation of the oxidised bitumen through attracting all the bitumen molecules to their surfaces, demonstrated by the reduced first peak position when the bitumen became oxidised.

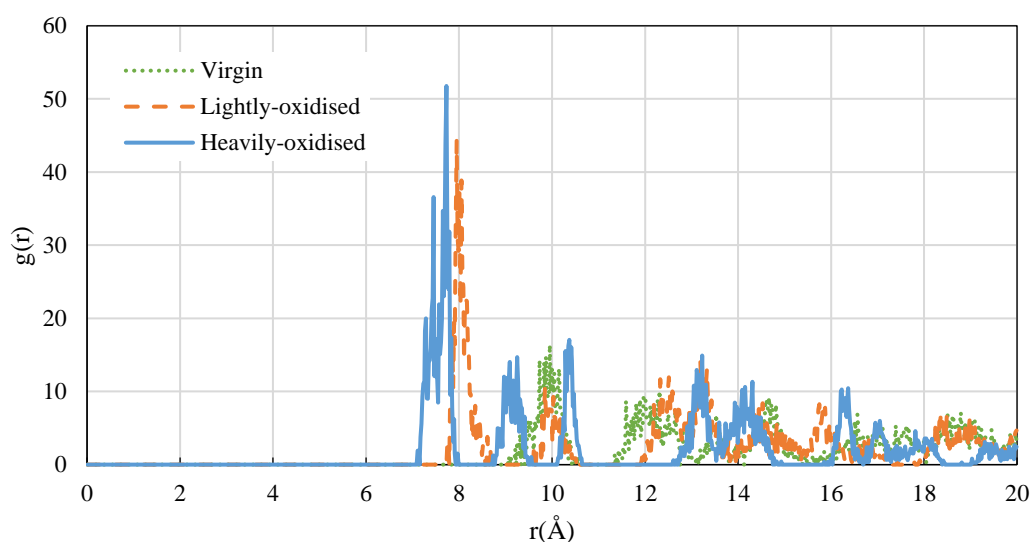


**Figure 3-11 RDFs of asphaltene-asphaltene pair in bitumen-microcline interfacial model at different oxidation levels.**

**Table 3-5 First peak positions of RDF curves for asphaltene-asphaltene pair in bulk bitumen model and four interfacial models at different oxidation levels.**

Models	Virgin	Lightly-oxidised	Heavily-oxidised
Bulk Bitumen Model	10-11 Å	4-5 Å	8-9 Å
Bitumen-Quartz Model	9-10 Å	6-7 Å	10 Å
Bitumen-Calcite Model	9-10 Å	9 Å	11-12 Å
Bitumen-Albite Model	10-11 Å	11-12 Å	8 Å
Bitumen-Microcline Model	10 Å	8 Å	7-8 Å

MSD is used to study the molecular mobility of bitumen on the mineral surfaces over time that is associated with the interaction between bitumen and minerals. In this study, MSD of the bitumen was measured based on the asphaltene molecule's centre of mass. A higher slope of MSD curves means a greater mobility of molecules. **Figure 3-12** illustrates the MSDs of asphaltenes in bitumen-microcline interfacial model at different oxidation levels. **Table 3-6** shows the slopes of MSD curves for asphaltenes in bulk bitumen model and four interfacial models at different oxidation levels. It can be seen that in all these models except for the bitumen-calcite model, the mobility of the oxidised bitumen was smaller than that of the virgin bitumen, which means that the oxidative ageing slowed down the mobility of the bitumen molecules. This is because the oxidised bitumen had an enhanced aggregation due to oxidation as well as a larger molecular weight with the introduction of the oxygen atoms. It is noted that the lightly-oxidised bitumen on the calcite surface had a greater molecular mobility since calcite caused the weak aggregation of the lightly-oxidised bitumen that has been shown in **Table 3-5**. It was also found from **Table 3-6** that the bitumen molecules on different mineral surfaces exhibits distinctive molecular mobility. The mobility of the bitumen on the quartz and calcite surfaces was faster than that on the albite and microcline surfaces as the strong attraction between bitumen and alkaline minerals (albite and microcline) constrained the mobility of the bitumen molecules.

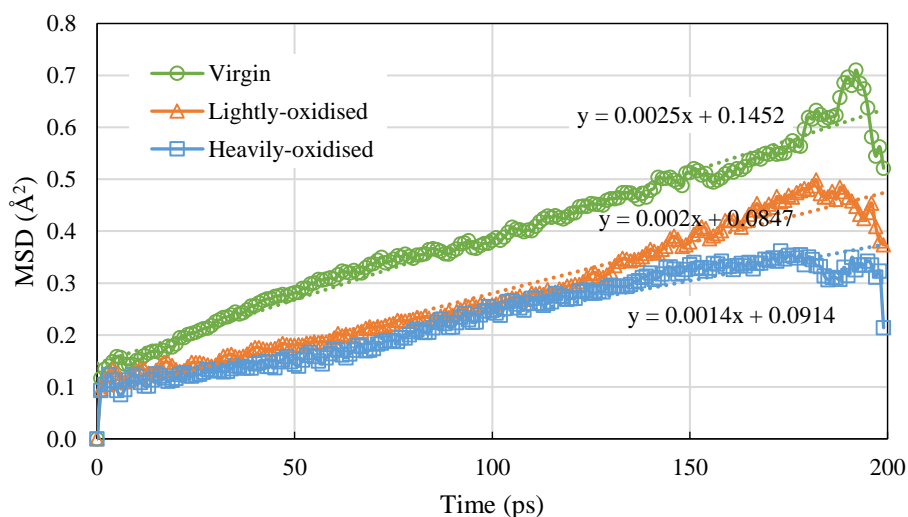


**Figure 3-12 MSDs of asphaltenes in bitumen-microcline interfacial model at different oxidation levels.**

**Table 3-6 Slopes of MSD curves for asphaltenes in bulk bitumen model and four interfacial models at different oxidation levels.**

Models	Virgin	Lightly-oxidised	Heavily-oxidised
Bulk Bitumen Model	0.0052	0.0013	0.0050
Bitumen-Quartz Model	0.0124	0.0014	0.0092
Bitumen-Calcite Model	0.0049	0.0139	0.0057
Bitumen-Albite Model	0.0034	0.0031	0.0006
Bitumen-Microcline Model	0.0025	0.0020	0.0014

### 3.7.3 Effect of oxidative ageing on bitumen adhesive bonding performance in dry condition

To quantify adhesive bonding performance between the bitumen (at different oxidation levels) and the different minerals in the dry condition, the adhesive bond energy of the bitumen-mineral interface systems was calculated using **Equations (2-16) and (2-17)**. **Figures 3-13, 3-15, 3-16 and 3-17** illustrate the adhesive bond energy for the bitumen-quartz, bitumen-calcite, bitumen-albite and bitumen-microcline interface models in the dry condition and at different oxidative ageing levels of the bitumen. It's noted that, based on **Equations (2-1) and (2-3)**, the total energy of a molecular system equals the summation of valence energy and non-bonded energy, where the non-bonded energy is composed of van der Waals and electrostatic interaction energy. It was found that total energy equalled to the non-bond energy for all of the four bitumen-mineral interface systems, which indicates that the interfacial adhesion between bitumen and mineral purely results from the non-bond interaction and the valence energy does not contribute to the total energy of the bitumen-mineral system.

The adhesive bond energy of the bitumen-quartz model in the dry condition and at different oxidation levels of the bitumen is shown in **Figure 3-13**. It was found that the adhesive bond energy ( $W_{BM-dry}$ ) decreased with the increase of the oxidation level, which indicates that the bitumen ageing weakens the interfacial adhesion between the bitumen and the quartz. This is in agreement with the experimental finding from (Yi et al., 2018) who found that the ageing of bitumen weakened the bonding performance between bitumen and granite (in which quartz is the major component). The negative effect of ageing is due to the decreased van der Waals energy after ageing, where the van der Waals is the primary component of the adhesion between the bitumen and the quartz as the electrostatic energy contributes little to the total energy, as indicated in **Figure 3-13**.

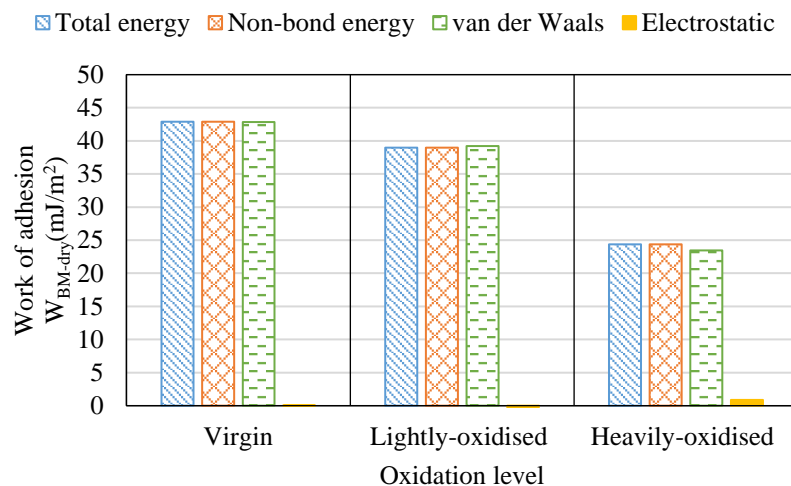


**Figure 3-13 Adhesive bond energy for bitumen-quartz interface model in the dry condition and different oxidation levels.**

The decreased van der Waals energy is fundamentally caused by the increased distance between the bitumen and quartz molecules when the bitumen becomes aged. In **Figure 3-14(a)**, the centre-to-centre distance between the bitumen mass and the quartz matrix was computed. It was found that the centre-to-centre distance of the bitumen-quartz models increased from 30.65 Å ( $10^{-10}$  m) for the virgin bitumen to 31.15 Å and 34.34 Å for the lightly-oxidised bitumen and the heavily-oxidised bitumen, respectively. According to **Equation (2-5)**, a greater distance between atoms leads to a lower van der Waals energy. Thus the van der Waals energy between bitumen and quartz is reduced when the bitumen becomes more severely aged. Furthermore, the increased centre-to-centre distance between bitumen and quartz at a higher oxidation level is believed due to the stronger aggregation of the oxidised bitumen molecules, resulting from higher polarity and molecular weight when the oxygen atoms are introduced into the bitumen. In summary, the severer agglomeration of the oxidised bitumen caused by more polar ketone and sulfoxide functional groups leads to a greater distance between the mass centre of the bitumen and quartz, which decreases the van der Waals interaction and eventually weakens the adhesive bond energy of the bitumen-quartz model in the dry condition.

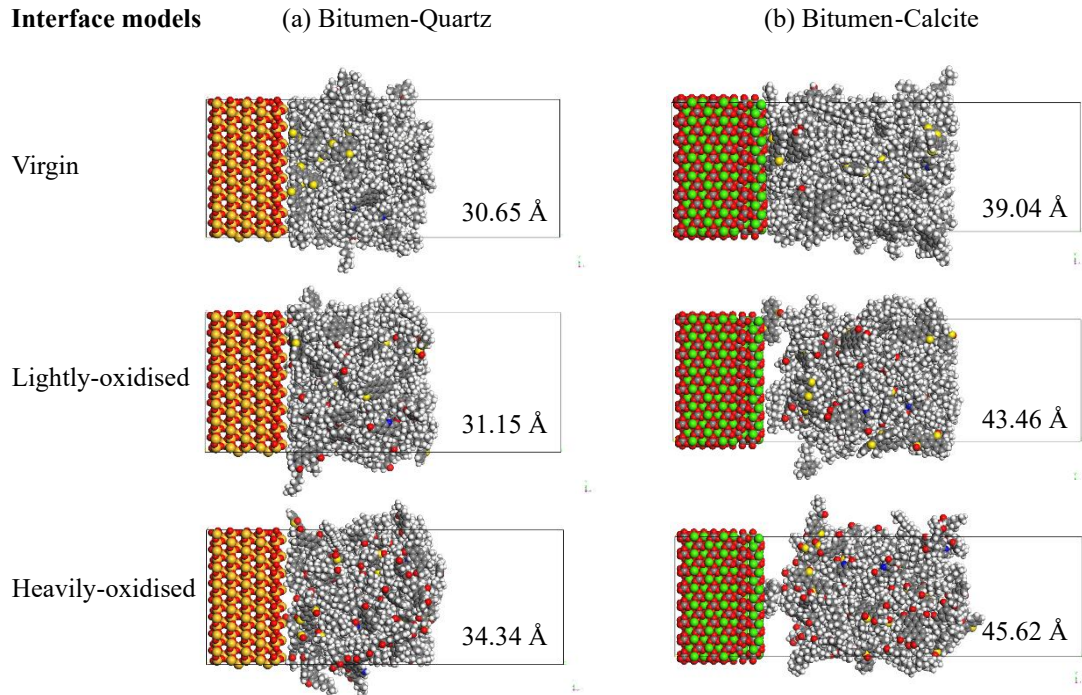


**Figure 3-14** Centre-to-centre distance (Å or  $10^{-10}$  m) between bitumen mass and mineral matrix for (a) bitumen-quartz interface model and (b) bitumen-calcite interface model at different oxidation levels.

**Figure 3-15** shows the adhesive bond energy of the bitumen-calcite interface model in the dry condition and at different oxidation levels. The adhesive bond energy ( $W_{\text{BM-dry}}$ ) first decreased from 57.13 mJ/m<sup>2</sup> for the virgin interface model to 34.97 mJ/m<sup>2</sup> for the lightly-oxidised interface model but then increased to 61.08 mJ/m<sup>2</sup> for the heavily-oxidised interface model. This change results from the combined ageing-induced changes of the van der Waals energy and the electrostatic energy that both contribute to the adhesion between the bitumen and the calcite, as shown in **Figure 3-15**. (Cucalon et al., 2017) also found that, compared to the virgin bitumen, the long-term aged bitumen using a Pressure Ageing Vessel (PAV) test has a higher adhesive bond energy with limestone (in which calcite is the main component). The results in **Figure 3-15** verifies the findings of (Cucalon et al., 2017) from the molecular modelling perspective.

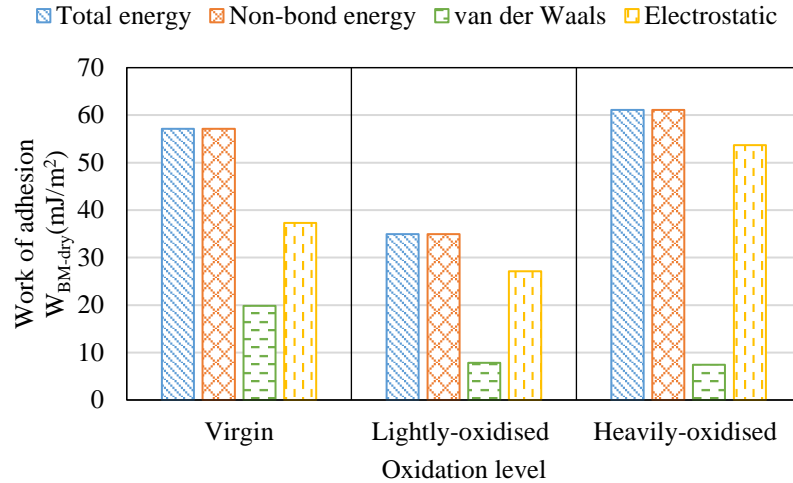


**Figure 3-15 Adhesive bond energy for bitumen-calcite interface model in dry condition and different oxidation levels.**

The van der Waals energy is inversely proportional to the distance between atoms according to **Equation (2-5)**. It can be seen from **Figure 3-14(b)** that the centre-to-centre distance between the bitumen mass and calcite matrix has increased from 39.04 Å for the virgin bitumen-calcite model to 43.46 Å for the lightly-oxidised bitumen-calcite model and 45.62 Å for the heavily-oxidised bitumen-calcite model, respectively. This leads to a constant decrease of the van der Waals energy with the increasing oxidation level in the bitumen-calcite interface system, which is consistent with the findings for the bitumen-quartz interface system as shown in **Figure 3-13**.

However, the electrostatic energy is inversely proportional to the distance between the atoms and directly proportional to the atomic charges according to **Equation (2-4)**. When the bitumen becomes more severely aged, the greater bitumen-calcite distance (due to more aggregation of bitumen molecules) causes a lower electrostatic energy and the higher atomic charges (due to more oxygen atoms and higher polarity) results in a higher electrostatic energy. **Figure 3-15** shows that the electrostatic energy of the bitumen-calcite interface system decreased when the bitumen became lightly-oxidised and then increased when the bitumen was heavily-oxidised. Thus it may be concluded that the centre-to-centre distance is the dominating factor for determining the electrostatic energy of the lightly-oxidised bitumen-calcite interface system, whereas the atomic charge is the dominating factor for determining the electrostatic energy of the heavily-oxidised bitumen-calcite interface system.

**Figure 3-15** also indicates that the electrostatic energy is the primary contributor and

the van der Waals energy is the secondary contributor for the non-bonded energy (that is the same as the total energy). Thus the change of the adhesive bond energy for the bitumen-calcite model is dominantly determined by and follows the same trend as the electrostatic energy, which decreases when bitumen is lightly-oxidised and then increases when the bitumen becomes heavily-oxidised.

The values of adhesive bond energy for the bitumen-albite model and the bitumen-microcline model in the dry condition and at different oxidation levels are shown in **Figures 3-16** and **3-17**, respectively. It was found that the adhesive bond energy ( $W_{\text{BM-dry}}$ ) significantly increased with the increase of the oxidation level, which indicates that the oxidation of bitumen is able to strengthen the adhesion for the bitumen-albite interface and the bitumen-microcline interface. This is because of the considerable increase of the electrostatic energy that contributes to the primary interfacial adhesion in the bitumen-albite model and the bitumen-microcline model, as shown in **Figures 3-16** and **3-17**. The strong electrostatic interaction for the oxidised bitumen-albite or bitumen-microcline interface system is caused by the very strong electrostatic attraction between the negatively charged oxidised bitumen due to the introduction of oxygen atoms during ageing and the positively charged alkaline minerals (albite and microcline). It is noted that the van der Waal energy is a very minor contributor to the total energy as shown in **Figures 3-16** and **3-17**. Thus the adhesive bond energy is primarily dominated by the electrostatic energy for the bitumen-albite or bitumen-microcline interface system.

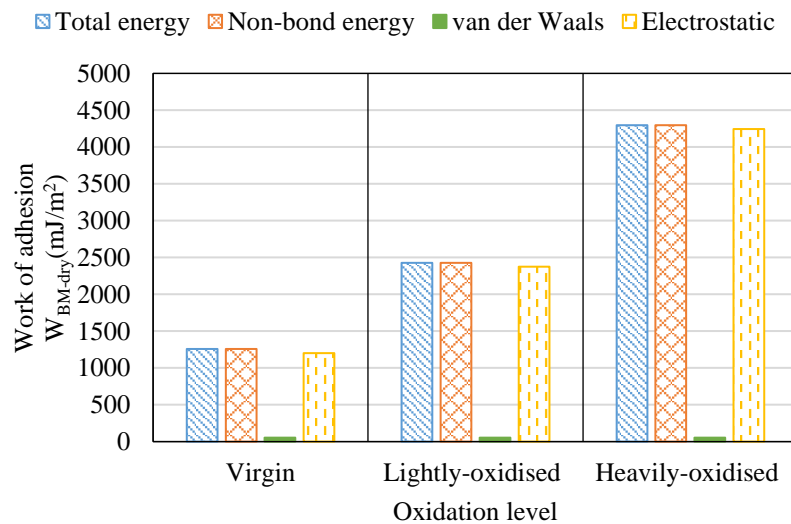


**Figure 3-16 Adhesive bond energy for bitumen-albite interface model in dry condition and different oxidation levels.**

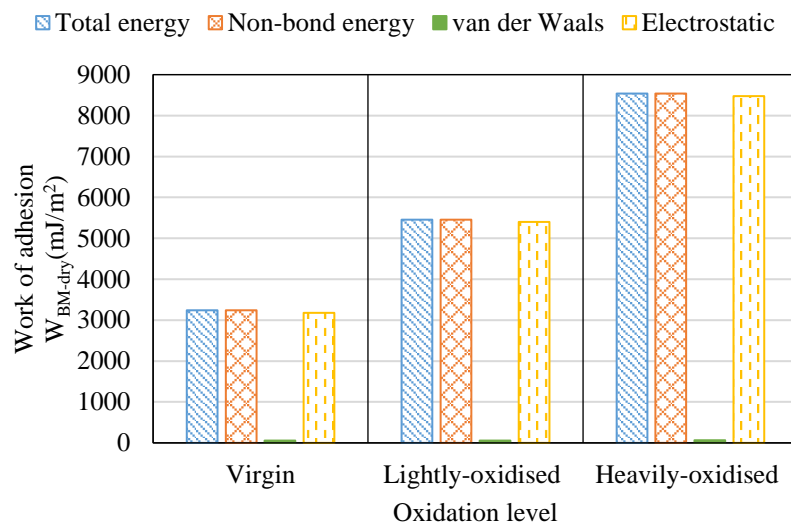


**Figure 3-17 Adhesive bond energy for bitumen-microcline interface model in dry condition and different oxidation levels.**

As observed above, the variation of the adhesive bond energy for the four bitumen-mineral models in dry condition is significantly distinct when bitumen becomes more severely aged (decrease for the bitumen-quartz model, decrease and then increase for the bitumen-calcite model, and increase for the bitumen-albite model and the bitumen-microcline model). The difference results from the different chemical properties of the minerals. Quartz is an acidic mineral, having a rather weak or negligible electrostatic interaction with the acidic bitumen, while albite and microcline are the strongly alkaline minerals, having a considerably strong electrostatic interaction with the oxidised bitumen containing more polar molecules. Calcite presents weakly alkaline, having a relatively weak electrostatic interaction with the acidic bitumen. The previous experimental studies (Mirzababaei, 2016) have shown that a mineral with an alkaline nature has a stronger electrostatic adhesion with the weakly acidic bitumen than an acidic mineral. Therefore, it can be concluded that the effect of bitumen oxidative ageing on the adhesive bonding performance strongly depends on the mineral types.

#### **3.7.4 Effect of oxidative ageing on bitumen adhesive bonding performance in wet condition**

To study the effect of oxidative ageing in wet condition, the adhesive bond energy of the four bitumen-water-mineral interface systems at different oxidation levels was also calculated based on the MD simulation results and was compared with the adhesive bond energy in dry condition, as shown in **Figures 3-18, 3-19, 3-20 and 3-21**.

The adhesive bond energy of the bitumen-quartz model in dry and wet conditions with different oxidation levels is shown in **Figure 3-18**. It can be seen that the adhesive bond energy in wet condition had little change with the oxidation level, which indicates that the oxidative ageing has a very weak or none influence on the bitumen-quartz interfacial adhesion in the wet condition. This is because the already very low van der Waals interaction (serving as the major contributor to the bitumen-quartz adhesion) in wet condition cannot be further reduced by the stronger aggregation of the oxidised bitumen at the ageing condition. **Figure 3-18** also shows that the adhesive bond energy was much smaller in the wet condition as compared to that in the dry condition. This is because the presence of water molecules has separated the bitumen from the quartz and increased the distance between the bitumen molecules and the quartz atoms, leading to the very weak van der Waals interaction according to **Equation (2-5)**.

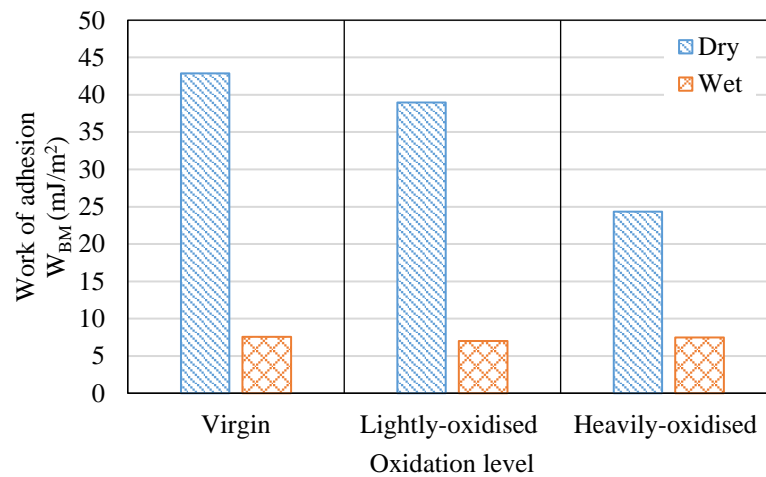


**Figure 3-18 Adhesive bond energy of bitumen-quartz model in dry and wet conditions and at different oxidation levels.**

**Figure 3-19** shows the adhesive bond energy of the bitumen-calcite model in dry and wet conditions with different oxidation levels. It was found that the adhesive bond energy for the oxidised bitumen-calcite model was slightly greater than that of the virgin model in the wet condition, which indicates that the oxidation of bitumen has made the bitumen-calcite adhesion stronger in the wet condition. This is because of the increase of the electrostatic interaction between bitumen and calcite. This explains the findings from (Cucalon et al., 2017) that the resistance of the interfacial bonding between bitumen and limestone to moisture damage improves when the bitumen becomes aged. **Figure 3-19** also shows that the adhesive bond energy in wet condition was always smaller than that in dry condition since the presence of water molecules makes the bitumen-calcite van der Waals interaction weaker. This means that

water tends to weaken the adhesion between bitumen and calcite, which remains consistent with the bitumen-quartz model.

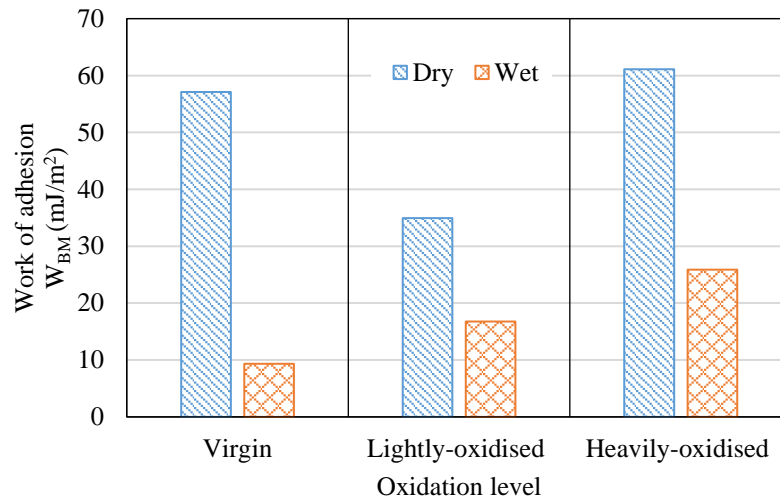


**Figure 3-19 Adhesive bond energy of bitumen-calcite model in dry and wet conditions and at different oxidation levels.**

The values of adhesive bond energy for the bitumen-albite model and the bitumen-microcline model in dry and wet conditions and at different oxidation levels are shown in **Figures 3-20** and **3-21**, respectively. It was found that the adhesive bond energy in both dry and wet conditions significantly increased with the increase of oxidation level, which indicates that the oxidative ageing has been able to strengthen the interfacial adhesion for the bitumen-albite model and the bitumen-microcline model, regardless the effect of water. This results from the considerable increase of the electrostatic interaction which is the major contributor to the interfacial adhesion of the bitumen-albite model and the bitumen-microcline model. From **Figure 3-20** and **3-21**, it can be seen that the adhesive bond energy in wet condition was very close to and consistent with that in dry condition. This differs from the case of the bitumen-quartz model and the bitumen-calcite model where the adhesive bond energy in wet condition was always weaker than that in the dry condition, as shown in **Figures 3-18** and **3-19**. This difference is mainly caused by the much stronger electrostatic interaction at the bitumen-albite interface and the bitumen-microcline interface, resulting from the stronger attraction between the highly alkaline minerals (albite and microcline) and the oxidised bitumen with the high polarity due to oxidative ageing.

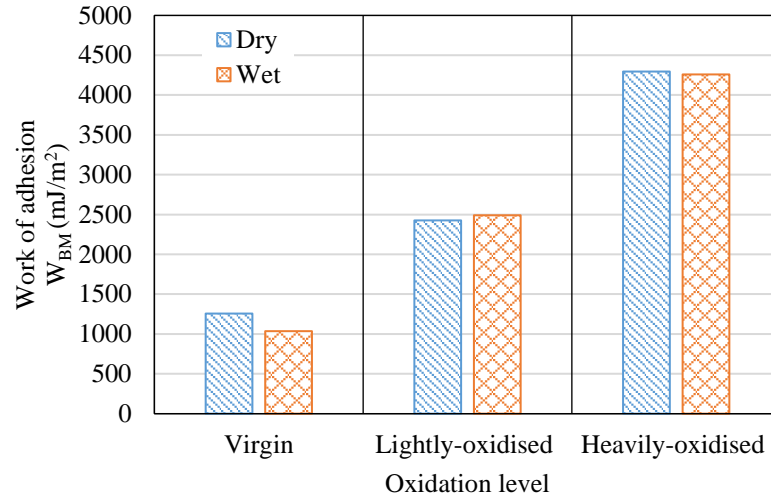


**Figure 3-20 Adhesive bond energy of bitumen-albite model in dry and wet conditions and at different oxidation levels.**

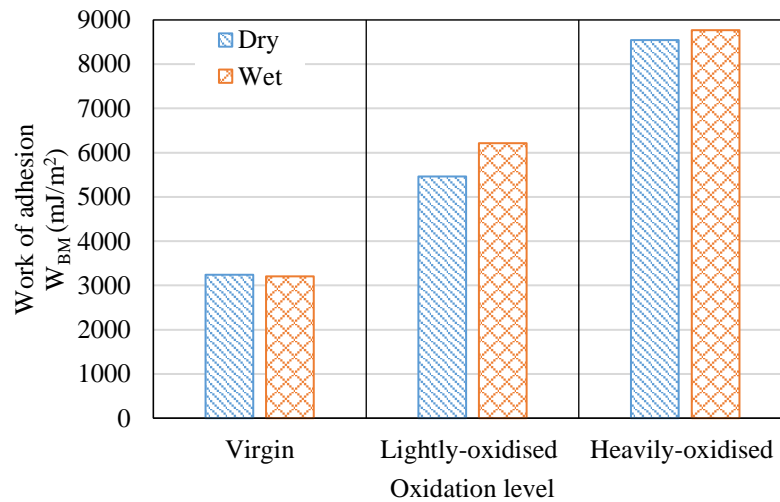


**Figure 3-21 Adhesive bond energy of bitumen-microcline model in dry and wet conditions and at different oxidation levels.**

### 3.7.5 Combined effect of oxidative ageing and water on bitumen adhesive bonding performance

To clearly describe the combined effects of oxidative ageing and water on the bitumen adhesive bonding performance in wet condition, the sensitivity of adhesion to oxidative ageing ( $S_o$ ) and the sensitivity of adhesion to water ( $S_w$ ) are proposed using the adhesive bond energy. The sensitivity of adhesion to oxidative ageing ( $S_o$ ) in wet condition is defined as the difference of the adhesive bond energy before and after oxidative ageing divided by the adhesive bond

energy before oxidative ageing, as shown in **Equation (3-1)**. The sensitivity of adhesion to water ( $S_W$ ) is calculated as the ratio of the change of the adhesive bond energy from dry to wet conditions as compared to the adhesive bond energy in dry condition, as expressed in **Equation (3-2)**. A higher absolute value of the sensitivity of adhesion ( $S_O$  or  $S_W$ ) means a greater effect of oxidative ageing or water on the bitumen-mineral adhesion. A positive (or negative) value of the sensitivity of adhesion ( $S$ ) indicates the strengthening (or weakening) effect.

$$S_{O-H} = (W_{BM-H} - W_{BM-V}) / W_{BM-V} \quad \text{or} \quad S_{O-L} = (W_{BM-L} - W_{BM-V}) / W_{BM-V} \quad (3-1)$$

$$S_W = (W_{BM-wet} - W_{BM-dry}) / W_{BM-dry} \quad (3-2)$$

where  $W_{BM-H}$ ,  $W_{BM-L}$ , and  $W_{BM-V}$  are the adhesive bond energy between bitumen and mineral in wet condition for heavily-oxidised, lightly-oxidised and virgin bitumens, respectively; and  $W_{BM-dry}$  and  $W_{BM-wet}$  are the adhesive bond energy between bitumen and mineral in dry and wet conditions, respectively.

**Figure 3-22** shows the sensitivity of adhesion to the oxidative ageing ( $S_{O-H}$  and  $S_{O-L}$ ) and water ( $S_W$ ) for quartz (acidic), calcite (weak alkali) and albite (strong alkali) minerals. It can be seen that the sensitivity of the bitumen-mineral adhesion to the oxidative ageing becomes higher and the absolute sensitivity of the bitumen-mineral adhesion to water becomes lower when the mineral changes from acidic to weak alkali and to strong alkali types.

This is fundamentally due to that, for the acidic minerals, van der Waals energy is the major contributor for bitumen-mineral adhesion which can be significantly reduced by water through increasing the distance between the bitumen and the acidic minerals. In this case, the electrostatic energy of the acidic mineral with the acidic bitumen is so weak that the increase of the polarity of the bitumen due to ageing will not alter the overall adhesion between the bitumen and the acidic minerals. Therefore, the adhesion of the acidic minerals (such as quartz) with bitumen is more susceptible to the water but much less sensitive to the bitumen ageing.

For the strong alkali minerals, the electrostatic energy is much higher than the van der Waals energy and becomes the dominating contributor to the bitumen-mineral adhesion. The electrostatic energy becomes even higher when the bitumen is aged due to higher polarity of the oxidised bitumen. However, the van der Waals is so minor for the adhesion between bitumen and the strong alkali minerals that the decrease of the van der Waals due to water cannot alter the adhesion significantly. Thus the adhesion of the strong alkali minerals (such as albite and microcline) with bitumen is more susceptible to bitumen ageing but less sensitive to water.

For the weak alkali minerals, both the van der Waals and the electrostatic energy

contribute to the adhesion with bitumen. The van der Waal energy can be significantly reduced by water due to greater distance and the electrostatic energy can be dramatically increased by bitumen ageing due to higher polarity. Thus the adhesion of the weak alkali mineral (such as calcite) with bitumen is susceptible to both bitumen ageing and the water.

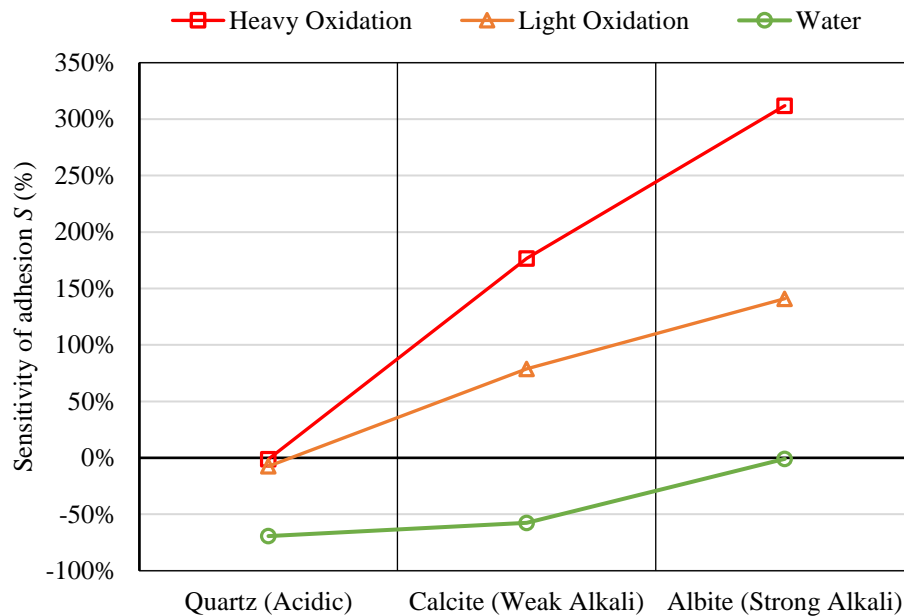


**Figure 3-22 Sensitivity of adhesion to oxidative ageing ( $S_{O-H}$  and  $S_{O-L}$ ) and water ( $S_w$ ) for quartz (acidic), calcite (weak alkali) and albite (strong alkali) minerals.**

### 3.8 Conclusions

In this chapter, a study has been conducted to investigate the molecular mechanism of the oxidative ageing effect on bitumen bonding performance using molecular dynamics (MD) simulations at the nanoscale. Based on the results, the main conclusions are as follows:

- (1) The oxidised functional groups (i.e., ketone and sulfoxide) in bitumen due to oxidative ageing strengthens the intermolecular bonding performance of the bitumen including van der Waals and electrostatic interactions, which results in the aggregation of bitumen molecules and physical hardening of the aged bitumen.
- (2) The predicted cohesive bond energy of the aged bitumen from MD simulations has a good agreement with the measured results from the contact angle measurements. The cohesive bond energy of the aged bitumen predicted at the nanoscale can be used as an input for the mechanics modelling of fatigue cracking of the aged bitumen at the next

higher scale.

- (3) The adhesive bonding performance of bitumen-acidic minerals (e.g., quartz) at dry condition is dominated by van der Waals interaction which decreases when bitumen becomes aged. This is due to the increased bitumen-quartz distance caused by the aggregated bitumen molecules. In comparison, the interfacial adhesion of bitumen-strong alkali minerals (e.g., albite and microcline) is dominated by electrostatic energy which increases during ageing. This results from the higher polarity introduced by the oxidised products including ketone and sulfoxide in an aged bitumen.
- (4) The adhesive bonding performance of bitumen-weak alkali mineral (calcite) at dry condition is attributed primarily to electrostatic energy and secondarily to van der Waals energy. The electrostatic energy between aged bitumen and the weak alkali mineral decreases due to the increased bitumen-mineral distance when the bitumen is lightly-oxidised and increases due to the higher bitumen polarity when the bitumen is heavily-oxidised.
- (5) For the adhesive bonding performance in wet condition, water is the dominating factor that affects (weakens) the interfacial adhesion between the bitumen and the acidic minerals such as quartz. While the oxidative ageing of bitumen is the major factor that affects (strengthens) the interfacial adhesion between the bitumen and the strongly alkaline minerals (i.e., albite and microcline). For the weak alkali minerals such as calcite, both water and bitumen ageing can significantly affect the interfacial adhesion.

# Chapter 4 Quantifying Cohesive Debonding in Bitumen Under a Rotational Shear Fatigue Load\*

## 4.1 Overview

This chapter presents a quantification of bitumen's cohesive debonding due to fatigue using a crack length. A damage mechanics-based model (i.e., DSR-C model) is developed to predict the crack length in bitumen under a rotational shear fatigue load. The DSR-C model paves a quantitative foundation for the mechanics modelling of debonding performance of bitumen to determine fatigue crack initiation and propagation at the microscale and the macroscale (in **Chapters 5** and **6**), respectively. This model is derived using torque and dissipated strain energy equilibrium principles. The crack length is predicted using bitumen's shear moduli and phase angles in undamaged and damaged conditions, measured by linear amplitude sweep (LAS) tests and time sweep (TS) tests, respectively. The two tests are both performed using dynamic shear rheometer (DSR), thus the crack length model is named as a DSR-C model. To validate the DSR-C model, the crack lengths after the TS tests are measured using digital visualisation of cracking surfaces for one virgin bitumen 40/60 and one polymer-modified bitumen X-70 at two temperatures (15, 20 °C), two frequencies (10, 20 Hz) and two strain levels (5%, 7%) under unaged and aged conditions.

Results show that the DSR-C model can accurately predict the crack length in bitumen under a rotational shear fatigue load at different loading and material conditions. The crack length predicted by the DSR-C model has potential to serve as a direct and fundamental parameter to evaluate bitumen's resistance to fatigue cracking. The degradation in material properties of the bitumen results from the crack growth that initiates from the outer edge toward the centre of the sample under the rotational shear load.

## 4.2 Introduction

Fatigue cracking is a primary distress in asphalt pavements and caused by a repeated traffic loading. The fatigue performance of asphalt pavements is strongly related to a

---

\* Reprinted with permission from Taylor & Francis: Y. Zhang, **Y. Gao**. (2019). Predicting crack growth in viscoelastic bitumen under a rotational shear fatigue load. *Road Materials and Pavement Design*, DOI:10.1080/14680629.2019.1635516

bituminous binder that contributes to the rheology, cohesion and adhesion properties of asphalt mixtures (Gao et al., 2015, Zhang et al., 2014, Lytton et al., 2018). Therefore, accurate characterisation and quantification of the fatigue resistance of the bitumen are critical for optimising the asphalt mixture design and extending the service life of pavements.

Fatigue characterisation of bitumen has been a kernel research question in the past few decades. In the Strategic Highways Research Program (SHRP), a fatigue parameter ( $|G^*| \cdot \sin\delta$ ) was proposed to evaluate the fatigue properties of bitumen at the intermediate temperatures (Anderson and Kennedy, 1993), where  $|G^*|$  is shear modulus and  $\delta$  is the phase angle and both are measured by dynamic shear rheometer (DSR). The parameter ( $|G^*| \cdot \sin\delta$ ) should be minimized for the bitumen with a good resistance to fatigue cracking. However, it was found that the SHRP fatigue parameter is not correlated well to the fatigue life of asphalt mixtures and pavements (Bahia et al., 2001b, Planche et al., 2004, Tsai et al., 2005, Zhou et al., 2012). This is fundamentally due to that the shear modulus ( $|G^*|$ ) and the phase angle ( $\delta$ ) in the DSR tests were obtained within the linear viscoelastic region of bitumen without accounting for the damaging effect. This is particularly true for polymer-modified bitumen which can sustain a higher strain before cracking damage has occurred.

Consequently, different approaches were developed to improve the fatigue characterisation for bitumen. In the National Cooperative Highway Research Program (NCHRP) project 9-10, the time sweep (TS) repeated cyclic loading test using the DSR was introduced to study the fatigue behaviour of the bitumen (Bahia et al., 2001a). The TS test has been successfully used for defining fatigue failure and criteria of bitumen (Planche et al., 2004, Anderson et al., 2001, Bonnetti et al., 2002, Wang et al., 2016). Based on the fatigue data of the TS test, the dissipated energy concept has been widely used for bitumen fatigue analysis through providing the alternative definitions of fatigue failure, including the dissipated energy ratio (DER) (Anderson et al., 2001, Bonnetti et al., 2002, Ghuzlan and Carpenter, 2000, Martono et al., 2007) and the ratio of dissipated energy change (RDEC) (Shen and Carpenter, 2005, Shen et al., 2006, Shen et al., 2010). The dissipated energy parameters (DER and RDEC) are indirect and empirical indicators for defining fatigue failure of bitumen. Moreover, linear amplitude sweep (LAS) test was developed as an accelerated fatigue procedure. The test is performed at constant temperature and frequency with an increasing strain amplitude to measure the bitumen damage tolerance. The LAS test has been used to develop a fatigue law based on the viscoelastic continuum damage (VECD) mechanics (Hintz et al., 2011b, Hintz and Bahia, 2013a, Safaei and Castorena, 2016, Safaei and Castorena, 2017, Safaei et al., 2016, Wang et al., 2015a).

Although these methods have been employed to characterise the fatigue behaviour of bituminous binders, the fatigue cracking mechanism are not yet well understood. Further studies from the fundamental mechanical perspective are very needed to understand the fatigue damage for the bitumen under a rotational shear fatigue load. Three key questions raised by the authors are as follows: in the bitumen under the shear fatigue load, (a) what the damage looks like; (b) when the damage is initiated; and (c) how the damage evolves. This Chapter is focused on clarifying the first question and the last two questions will be addressed in **Chapters 5** and **6**.

To understand the damage mechanism leading to bitumen fatigue, some existing studies have been started to focus on the direct investigations of the fatigue crack growth in the bitumen under a rotational shear fatigue load. Hintz and Bahia (2013b) used the time sweep (TS) test in the DSR and the digital visualisation to investigate the fatigue crack growth of the bitumen samples. Shan et al. (2017) employed the DSR testing and the image analysis method to determine the internal crack growth of the bitumen samples during a shear fatigue process. In these studies, **Equation (4-1)** was used to predict the effective radius based on the decrease of the measured torque ( $T$ ) with the number of load cycles in the TS test.

$$r_E^4 = \frac{2Th}{\pi\theta|G_0^*|} \quad (4-1)$$

where  $r_E$  is the effective radius that is the radius of the remaining uncracked area of the bitumen sample in the DSR test;  $T$  and  $\theta$  are the torque and the deflection angle measured by DSR, respectively;  $h$  is the height of the sample; and  $|G_0^*|$  is the shear modulus of the undamaged bitumen.

The crack length in the DSR test was determined by subtracting the effective radius determined by **Equation (4-1)** from the original sample radius. It was found the crack length was less than the measured values from the digital image analysis, particularly at a relatively larger number of load cycles (Hintz and Bahia, 2013b, Shan et al., 2017). This is fundamentally due to the fact that **Equation (4-1)** is derived based on a linearly elastic stress-strain constitutive relation in the undamaged condition thus cannot be used to predict the effective radius which results from the fatigue crack growth in the damaged condition. An assumption was made for **Equation (4-1)** that the shear modulus  $|G^*|$  in the damaging DSR test was assigned as a constant  $|G_0^*|$  that is the shear modulus for the bitumen in the undamaged DSR test. This assumption needs a more solid justification or it can lead to significant systematic errors in the prediction

of the crack growth in the DSR test. Therefore, a further study is needed to better understand the cohesive debonding process due to fatigue and to predict the fatigue crack length of the bitumen in the DSR tests. A better fatigue crack prediction can improve the fundamental understanding and the grading system of the bitumen in terms of fatigue performance.

The objective of this study is to develop a crack length model to quantify cohesive debonding behaviour of bitumen during the DSR testing, so as to provide a direct method to effectively evaluate the fatigue resistance of the bitumen. Using torque and dissipated strain energy (DSE) equilibrium principles, a mechanical model is developed to predict the crack length of the bitumen sample under a rotational shear fatigue load. DSR tests are conducted to determine the model parameters and digital visualisation of cracking surfaces is used to measure crack length in order to validate the developed prediction model. Finally, this model is used to analyse the process of the crack growth in the bitumen sample under the shear fatigue load.

### 4.3 Linear Viscoelastic Analysis of Bitumen

The linear viscoelastic analysis of the bitumen in an undamaged condition is firstly presented. For a strain-controlled cyclic load in the undamaged condition, the strain amplitude is relatively small (e.g., < 1%), within which the shear modulus and phase angle of the bitumen remain unchanged at different strain levels. In this case, a controlled shear strain is expressed as

$$\gamma(t) = \gamma_0 \sin(\omega t) \quad (4-2)$$

and the corresponding shear stress response in the undamaged condition is

$$\tau(t) = \tau_0 \sin(\omega t + \delta_0) \quad (4-3)$$

where  $\gamma_0$  and  $\tau_0$  are the strain amplitude and the stress amplitude, respectively;  $\omega$  is the loading frequency,  $t$  is the loading time, and  $\delta_0$  is the phase angle of the bitumen in the undamaged condition.

The strain amplitude at a given radial position in a cylindrical bitumen sample is defined as

$$\gamma_0(r) = \frac{\theta_0}{h} r \quad \text{with } 0 \leq r \leq r_0 \quad (4-4)$$

where  $\theta_0$  is the amplitude of deflection (rotational) angle,  $r_0$  and  $h$  are the radius and the height of the cylindrical sample, respectively. It is noted that the rotation amplitude  $\theta_0$  is controlled by

DSR directly.

According to the linear viscoelastic stress-strain law and **Equation (4-4)**, the stress amplitude at a given radial position of the sample in the undamaged condition can be expressed as

$$\tau_0(r) = |G_0^*| \gamma_0(r) = \frac{|G_0^*| \theta_0}{h} r \quad \text{with } 0 \leq r \leq r_0 \quad (4-5)$$

where  $|G_0^*|$  is the shear modulus of the bitumen in the undamaged condition. It is found from **Equation (4-5)** that the stress amplitude has a linear relationship with the radius ( $r$ ) of the sample. The stress amplitude increases along the radial direction from the centre to the edge of the sample. When  $r = r_0$ , the stress amplitude reaches its maximum value:

$$\tau_{0\max} = \frac{|G_0^*| \theta_0}{h} r_0 \quad (4-6)$$

where  $\tau_{0\max}$  is the maximum stress amplitude in the undamaged condition, which occurs at the edge of the cylindrical sample. Then, the stress amplitude at a given radial position can be also expressed as

$$\tau_0(r) = \frac{r}{r_0} \tau_{0\max} \quad \text{with } 0 \leq r \leq r_0 \quad (4-7)$$

The torque amplitude measured by DSR directly on the cylindrical bitumen sample in the undamaged condition is defined by **Equation (4-8)**.

$$T_0 = \int_0^{r_0} \tau_0 \cdot 2\pi r \cdot r \cdot dr = \frac{\pi r_0^3}{2} \tau_{0\max} \quad (4-8)$$

Bitumen is a kind of viscoelastic material. When bitumen is subjected to cyclic fatigue loading, in each cycle, the stress-strain curve follows a hysteresis loop in a loading and unloading processes. The area inside the loop is defined as the dissipated strain energy (DSE) density. The DSE concept has been widely used for asphalt mixtures (Lytton et al., 2018, Zhang et al., 2018). The DSE density at a given radial position of the bitumen sample in the undamaged condition in one load cycle can be calculated by

$$DSE_0(r) = \int_{t_0}^{t_0 + \frac{2\pi}{\omega}} \tau(t) d\gamma(t) = \pi \tau_0(r) \gamma_0(r) \sin \delta_0 \quad (4-9)$$

where the strain amplitude  $\gamma_0(r) = \frac{\tau_0(r)}{|G_0^*|}$ , thus **Equation (4-9)** can be further written as

$$DSE_0(r) = \pi \tau_0(r)^2 \frac{\sin \delta_0}{|G_0^*|} \quad (4-10)$$

#### 4.4 Damage Viscoelastic Analysis of Bitumen

The nonlinear viscoelastic behaviour of the bitumen in the damaged condition is analysed under a strain-controlled rotational shear load. The bitumen is regarded as damaged when the strain amplitude is relatively high, at which the shear modulus and phase angle change with load cycles and strain levels. The controlled shear strain in the damaged condition is assumed as

$$\gamma_d(t) = \gamma_d \sin(\omega t) \quad (4-11)$$

and the measured shear stress is expressed as

$$\tau_N(t) = \tau_N \sin(\omega t + \delta_N) \quad (4-12)$$

where  $\delta_N$  is the phase angle of the bitumen at the  $N$ th load cycle in the damaged condition that changes with the load cycle;  $\gamma_d$  is the strain amplitude in the damaged condition; and  $\tau_N$  is the stress amplitude in the damaged condition that changes with the load cycle  $N$ . It is note that both the strain amplitude  $\gamma_d$  and the stress amplitude  $\tau_N$  are a function of the radius ( $r$ ) of the sample.

The shear modulus of the bitumen in the damaged condition is defined as

$$|G_N^*| = \frac{\tau_N(r)}{\gamma_d(r)} \quad (4-13)$$

Note that the shear modulus  $|G_N^*|$  in the damaged condition will decrease with load cycle due to the degradation of the materials. Comparable to **Equation (4-6)**, the maximum stress amplitude of the bitumen sample at the  $N$ th load cycle in the damaged condition can be expressed as:

$$\tau_{N \max} = \frac{|G_N^*| \theta_0}{h} r_0 \quad (4-14)$$

Thus, the torque amplitude measured by DSR directly at the  $N$ th load cycle is determined as:

$$T_N = \frac{\pi r_0^3}{2} \tau_{N \max} \quad (4-15)$$

The dissipated strain energy density at a given radial position of the cylindrical bitumen sample in the damaged condition and the  $N$ th load cycle can be formulated as

$$DSE_N(r) = \int_{(N-1)\frac{2\pi}{\omega}}^{N\frac{2\pi}{\omega}} \tau_N(t) d\gamma_d(t) = \pi \tau_N(r) \gamma_d(r) \sin \delta_N \quad (4-16)$$

where the strain amplitude  $\gamma_d(r) = \frac{\tau_N(r)}{|G_N^*|}$ . **Equation (4-16)** can be further expressed as

$$DSE_N(r) = \pi \tau_N(r)^2 \frac{\sin \delta_N}{|G_N^*|} \quad (4-17)$$

#### 4.5 Modelling Fatigue Crack Length in Bitumen Based on Damage Mechanics

The crack in the cylindrical sample manifests as an ‘edge crack’ under a rotational shear fatigue load in the DSR tests. The edge crack is a circumferential crack that initiates at the periphery of the sample and propagates toward the centre of the sample, based on the laboratory observations of the existing studies (Hintz and Bahia, 2013b, Shan et al., 2017, Aboutorabi et al., 1998). **Figure 4-1** shows the schematic side view of the cylindrical sample and the cracking path in the sample under the cyclic shear load. The cracking path was proposed and verified based on the laboratory observations of the cracking surfaces in the DSR tests in the literature (Hintz and Bahia, 2013b, Shan et al., 2017). In **Figure 4-1**,  $r_0$  is the original radius of the cylindrical bitumen sample and  $h$  is the height of the sample. In this study,  $r_0 = 4$  mm and  $h = 2$  mm. When crack grows, it starts from the sample edge and propagates towards the centre and  $c$  is the crack length. The radius of the remaining un-cracked areas is  $r_E$  that is defined as the effective radius of the sample, thus the crack length can be calculated as  $c = r_0 - r_E$ .

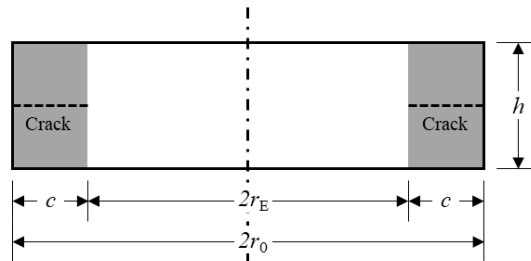


**Figure 4-1 Schematic of a cylindrical sample with a circumferential crack in dynamic shear rheometer (DSR) tests.**

Some researchers have reported the instability of the cracking known as “edge flow” occurring in the sample at the initiation stage of the DSR tests. The edge flow is not a true cracking phenomenon, which is caused by edge instability resulting from the development of the normal forces (Keentok and Xue, 1999, Anderson et al., 2001). Hintz et al. (2011a) have analysed the normal forces during time sweep (TS) testing and found that the normal stresses were negligible compared with the torsional stresses during the binder fatigue testing. It has also been demonstrated that the edge effect could be considered to have no significant effect on parallel plate fatigue testing (Martono et al., 2007) and the edge instability was ruled out as a cause of damage (Hintz and Bahia, 2013b). In this study, the edge instability is negligible and does not affect the crack growth measurement because a) the normal forces are found very small ( $< 0.1\text{N}$ ) and declined very quickly with load cycles; and b) the high shear strain level (5%) was used so that the sample exhibits damaging from the initiation stage of DSR tests. Thus, the damage mechanics concepts can be applied for characterisation and prediction of the fatigue cracking in bitumen under a rotational shear fatigue load.

To determine the effective radius and the crack length of the cylindrical bitumen sample at the  $N$ th load cycle during the shear fatigue process, two equilibrium principles of damage mechanics were employed including torque equilibrium principle and dissipated strain energy (DSE) equilibrium principle, which hypothesized that the torque and the DSE in the apparent (damaged) configuration of the bitumen were equivalent to those in the effective (undamaged) configuration, respectively. It is noted that this study utilised the fundamental energy equilibrium hypothesis from damage mechanics and built the balance equation between the two conditions (undamaged and damaged) of the material, but ignored the process how the material evolves from the undamaged condition to the damaged conditions. Thus the prediction of the cracking damage will use the material properties at the two conditions only. In contrast, this method does not require the material property information during the damage evolution process of the material, e.g., how the material evolves from linear viscoelastic condition to nonlinear viscoelastic condition and to the damage condition. The crack length measured from image analysis of the crack surfaces in bitumen will validate the prediction accuracy of the model, demonstrating that the equilibrium hypothesis of total dissipated strain energy in this damage mechanics framework is valid.

According to the torque amplitude equilibrium principle, the measured torque ( $T_N$ ) at the  $N$ th load cycle for the damaged configuration (with a radius of  $r_0$ ) is equivalent to the effective torque ( $T_E$ ) for the undamaged configuration (with a radius of  $r_E$ ), as expressed in **Equation (4-15)**.

$$T_N = T_E \quad (4-18)$$

Based on **Equations (4-15)** and **(4-8)**, **Equation (4-18)** can be further written as

$$\frac{\pi r_0^3}{2} \tau_{N\max} = \frac{\pi r_E^3}{2} \tau_{E\max} \quad (4-19)$$

where  $\tau_{N\max}$  is defined by **Equation (4-14)**, and  $\tau_{E\max}$  is the effective stress amplitude maximum for the undamaged configuration, defined by **Equation (4-6)** by replacing  $r_0$  with  $r_E$ .

According to the energy equilibrium principle for the entire volume of the cylindrical sample, the dissipated strain energy ( $DSE_N$ ) at the  $N$ th load cycle for the damaged configuration is equivalent to the effective dissipated strain energy ( $DSE_E$ ) for the undamaged configuration, as shown in **Equation (4-20)**.

$$\iiint_{V_0} DSE_N(r) dV_0 = \iiint_{V_E} DSE_E(r) dV_E \quad (4-20)$$

where  $V_0$  is the total volume of the damaged bitumen sample that has a radius of  $r_0$  and the material properties are those in the damaged conditions including  $|G_N^*|$  and  $\delta_N$ .  $V_E$  is the volume of the undamaged bitumen which has a radius of  $r_E$  and the material properties are those in the undamaged conditions including  $|G_0^*|$  and  $\delta_0$ . Substituting **Equations (4-17)** and **(4-10)** into **Equation (4-20)** gives

$$\int_0^{r_0} \pi \tau_N(r)^2 \frac{\sin \delta_N}{|G_N^*|} \cdot 2\pi r \cdot h \cdot dr = \int_0^{r_E} \pi \tau_E(r)^2 \frac{\sin \delta_0}{|G_0^*|} \cdot 2\pi r \cdot h \cdot dr \quad (4-21)$$

It is noted that the dissipated strain energy, rather than the dissipated strain energy density, was used to build the energy equilibrium equation.

Solving **Equations (4-19)**, **(4-21)** and **(4-7)**, the effective radius (see **Figure 4-1**) of the cylindrical bitumen sample at the  $N$ th load cycle can be obtained as **Equation (4-22)** and the crack length can be calculated by **Equation (4-23)**.

$$r_E = \left( \frac{|G_N^*| / \sin(\delta_N)}{|G_0^*| / \sin(\delta_0)} \right)^{\frac{1}{4}} r_0 \quad (4-22)$$

$$c = \left[ 1 - \left( \frac{|G_N^*| / \sin(\delta_N)}{|G_0^*| / \sin(\delta_0)} \right)^{\frac{1}{4}} \right] r_0 \quad (4-23)$$

The DSR-based crack length (DSR-C) model shown in **Equation (4-23)** provides a mechanics model to directly determine the crack growth (crack length,  $c$  vs. load cycle,  $N$ ) of a bitumen with an original radius of  $r_0$  in a cyclic and rotational shear test such as DSR test using the material properties including shear modulus and phase angle. It is emphasized that  $|G_0^*|$  and  $\delta_0$  are the shear modulus and phase angle of the bitumen in the undamaged condition (relatively low strain level, e.g.,  $< 1\%$  at room temperature);  $|G_N^*|$  and  $\delta_N$  are the shear modulus and phase angle of the bitumen at the  $N$ th load cycle which change with the load cycle as the bitumen was subjected to the damaged condition (relatively high strain level, e.g.,  $> 5\%$  at room temperature). The following laboratory test measurement of the crack length will demonstrate the reliability and accuracy of the DSR crack length prediction model shown in **Equation (4-23)**.

## 4.6 Materials and Laboratory Tests

### 4.6.1 Materials

Two types of bituminous binders, the bitumen X-70 (bitumen A) and the bitumen 40/60 (bitumen B), were used in this study. The bitumen A is a polymer modified bitumen with 45/80 penetration grade and the bitumen B is an unmodified bitumen with 40/60 penetration grade. The two binders were tested before and after Thin-Film Oven Test (TFOT) laboratory ageing that was conducted at the temperature of 163 °C for 5 hours. These bitumens are referred to as  $A_v$  and  $B_v$  before ageing and  $A_a$  and  $B_a$  after ageing, respectively.

### 4.6.2 Sample preparation

In this study, the bitumen samples were prepared following the AASHTO T315 “Determining the Rheological Properties of Asphalt Binder Using a Dynamic Shear Rheometer (DSR)” (AASHTO, 2012). The standard specimen geometry (8 mm in diameter with 2 mm height) was employed for all tests due to the testing temperature of 20 °C. The samples were prepared using a silicone mould. The hot bitumen from a heated container was poured into the mould to form a convex surface and then the filled mould was cooled to room temperature without chilling. Then, the bitumen was loosened from the mould by flexing the rubber mould and was adhered to the preheated lower test plate by gently pressing the convex (top) surface of the pellet. After that, the upper test plate was moved until the gap between the plates equals the testing gap (2mm) plus the gap closure required to create a slight bulge at the outside face of the test specimen. The excess bitumen was trimmed by moving a heated trimming tool

around the edges of the plates so that the bitumen is flush with the outer diameter of the plates. When the trimming is complete, the gap is decreased to the testing value (2mm). Finally, the bitumen was heated to the testing temperature and then remained for 5 minutes before loading.

#### 4.6.3 Test methods

Laboratory testing was conducted using a Kinexus DSR from Malvern Panalytical with 8-mm diameter parallel plate geometry. Two types of shear fatigue tests, linear amplitude sweep (LAS) test and time sweep (TS) test, were performed. Two replicates were tested at each testing condition and a third replicate was tested when the deviation was greater than 10%. The measured results were analysed based on the averaged data.

The linear amplitude sweep (LAS) tests were conducted to obtain the shear modulus ( $|G^*_0|$ ) and the phase angle ( $\delta_0$ ) of the bitumen under the undamaged condition and to determine the controlled strain levels for the later TS fatigue damage tests. The strain amplitudes ranged from 0.1% to 30% linearly. The shear modulus and phase angle were recorded with the increasing strain amplitudes. **Figure 4-2** shows a typical result of the LAS tests at 20 °C and 10 Hz which is for the unaged X-70 bitumen. The undamaged shear modulus ( $|G^*_0|$ ) and the phase angle ( $\delta_0$ ) were determined as the average values of the test data in the linear viscoelastic region (plateau stage) of the LAS test where the modulus or phase angle doesn't change with the strain levels, as shown in **Figure 4-2**. The strain sweep tests were performed at two temperatures (15 and 20 °C) and two loading frequencies (10 and 20 Hz), as shown in **Table 4-1**. The shear modulus ( $|G^*_0|$ ) and phase angle ( $\delta_0$ ) of the bitumen under the undamaged condition were also determined at those selected temperatures and loading frequencies. The strain levels (5% and 7%) were selected for TS fatigue damage tests in the nonlinear region of the LAS test conducted on all the tested bitumens at different temperatures or loading frequencies to induce damage. The images of cracking surfaces of bitumen sample shown in **Section 4.7.1** indicate that the applied strain levels were high enough to introduce the cracking damage in the TS tests for all the tested bitumens. In fact, the 5% and 7% strain levels have been used in the literature for the TS tests to study the fatigue damage behaviour of bitumen (Wang et al., 2015a, Wang et al., 2016).

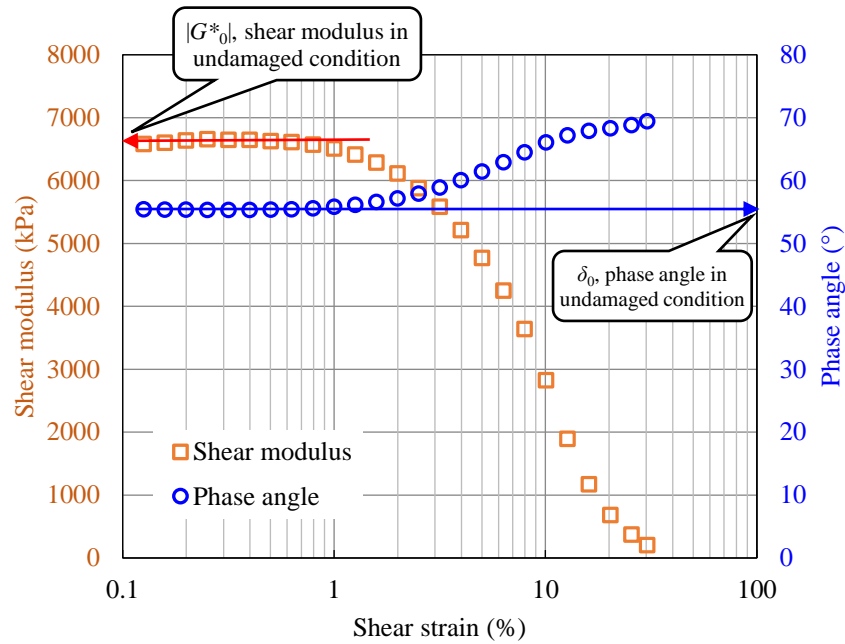


**Figure 4-2 Results of linear amplitude sweep (LAS) tests at 20 °C and 10 Hz including shear modulus ( $|G^*_0|$ ) and phase angle ( $\delta_0$ ) for unaged X-70 bitumen with strain levels.**

**Table 4-1 Shear fatigue testing plan.**

Test	Bitumen	Temperature (°C)	Frequency (Hz)	Strain level	Load cycles
Linear Amplitude Sweep (LAS)	A <sub>v</sub>	20	10	0.1% - 30%	NA
		15	10		
		20	20		
	B <sub>v</sub>	20	10	0.1% - 30%	NA
	A <sub>a</sub>				
Time Sweep (TS)	A <sub>v</sub>	20	10	5%	7200 24000 42000
		15	10	5%	24000
		20	20	5%	
		20	10	7%	
	B <sub>v</sub>	20	10	5%	7200 24000 42000
	A <sub>a</sub>	20	10	5%	24000
	B <sub>a</sub>	20	10	5%	

Note: A<sub>v</sub>, B<sub>v</sub>, A<sub>a</sub> and B<sub>a</sub> stand for the virgin X-70 bitumen (polymer modified), the virgin 40/60 bitumen (unmodified), the aged X-70 bitumen and the aged 40/60 bitumen, respectively.

Time sweep (TS) tests were conducted to obtain the shear modulus ( $|G^*_N|$ ) and the phase angle ( $\delta_N$ ) with the number of load cycles for the bitumen under the damaged condition. In this study, the TS tests were performed using sinusoidal loading with the rotation amplitudes of 0.025 and 0.035 rad, respectively, in order to achieve the target strain amplitudes (5% and 7%) at the edge of the sample ( $r = r_0$ ). The applied strain levels were determined from the above LAS tests at which the bitumen has been in the damaged condition. In order to validate the DSR crack growth model shown in **Equation (4-23)**, the TS tests were performed at different experimental conditions, summarised in **Table 4-1**. The test temperatures (15 and 20 °C) were selected to consider the intermediate temperatures when a fatigue cracking happens. The test frequencies (10 and 20 Hz) and strain levels (5% and 7%) were selected to produce fatigue cracking damage within a reasonable load cycle. The quality of the raw data obtained at the high frequency of 20 Hz was reviewed in the TS test. It was found that the constant shear strain (5%) was well controlled for the full loading history, which means that the DSR data obtained at 20 Hz is reliable.

**Figure 4-3** shows a typical result of the TS test which is for the unaged X-70 bitumen. The test was controlled at a constant strain (5%), a temperature of 20 °C and a loading frequency of 10 Hz. The shear modulus was observed to decrease with load cycles and the phase angle increases to a peak and then decreases with load cycles in the TS test. It should be noted that, at a high strain level (e.g., 5%), cracking damage can lead to not only the decrease of shear modulus but the increase of phase angle. Characterising both changes is critical to accurately model the fatigue performance of bitumen. In fact, it has been reported in the literature (Wang et al., 2015a, Wang et al., 2016) that the phase angle increases up to a peak during the fatigue tests and this peak was used to define the fatigue failure of bitumen.

After the time sweep (TS) test, the crack surface morphological pattern of the bitumen sample needs to be obtained in order to measure the effective radius ( $r_E$ ) of the un-cracked areas of the sample so that the crack length can be determined using  $c = r_0 - r_E$ . The temperature of the sample was reduced to 3 °C immediately after the TS test and maintained for 10 min to freeze the crack surface pattern thoroughly. Then, the top DSR loading platen was directly pulled off from the bottom platen. The bitumen sample's top and bottom surfaces were photographed and the image processing was used to determine the effective radius, which will be detailed in the next section.

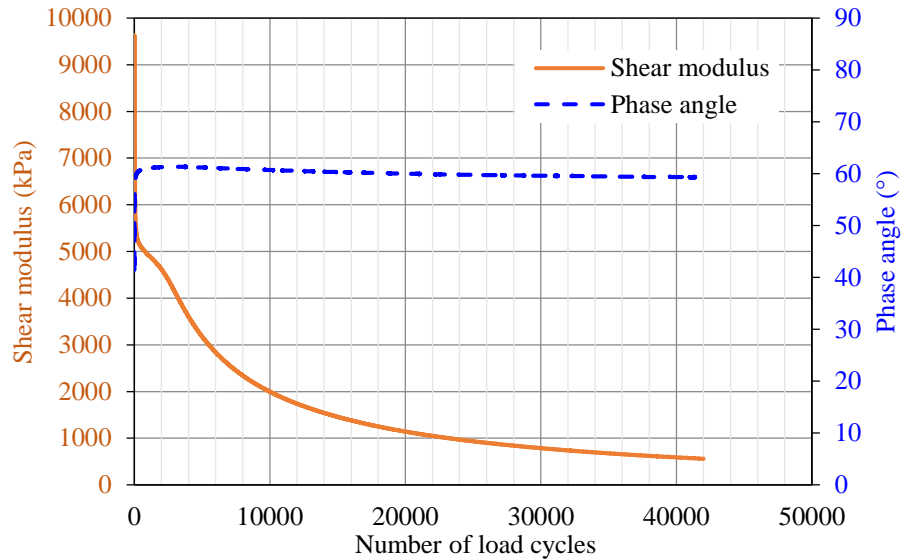


**Figure 4-3 Results of time sweep (TS) test at 5% strain, 20 °C and 10 Hz including shear modulus ( $|G^*_N|$ ) and phase angle ( $\delta_N$ ) for unaged X-70 bitumen with load cycles.**

## 4.7 Results and Discussion

### 4.7.1 Measurement of crack length

A typical image of the bitumen cracking surface after the time sweep (TS) test is presented in **Figure 4-4(a)**. It is observed from this image that the bitumen surface shows distinct morphological patterns at different areas. In the central area of the bitumen sample, it shows a flat and smooth surface which is caused by the direct tensile pull-off (Mode-I fracture) after the TS test. Thus this central area represents the uncracked portion of the sample during the TS test, whose radius is defined as the effective radius ( $r_E$ ). Surrounding this central area, a ring area with rough surfaces exists consisting of the radial peaks and valleys, which results from the shear-induced surface interactions between the top and bottom crack faces. This type of cracking morphology is referred to as ‘factory roof’ (Tschegg et al., 1983). It is believed that this ring area is caused by the cracking under a rotational shear load. This ‘factory roof’ morphology of the crack surface proved that the crack growth in a DSR bitumen sample is fundamentally controlled by the shear fatigue load rather than the ‘edge instability’. The same morphology of bitumen cracking surfaces under a shear fatigue loading was reported in the previous studies (Hintz and Bahia, 2013b, Shan et al., 2017). It is noted from **Equation (4-5)** that the crack under a rotational shear load is initiated at the outer edge of the sample where the largest shear stress occurs. Thus the crack grows toward the centre of the sample once initiated.

**Figure 4-4(b)** shows how the crack length was determined from the bitumen cracking surface photos using an image analysis software Digimizer. The crack length can be determined following the below image-processing steps:

- (1) The edge of the bitumen sample on photos was determined using the *Circle to Center* tool in Digimizer. Then the total area of the bitumen sample on photos can be measured in pixels and the corresponding radius ( $r_{0pi}$ ) of the sample was calculated using the total area.
- (2) The intact area (uncracked portion) in the centre of the sample on photos was identified by defining a circumference as the circular boundary between the central uncracked area with a smooth surface and the ring cracked area with the rough surface. The area of this intact area is measured in pixels using the *Circle to Center* tool in Digimizer, which is then utilized to determine the effective radius ( $r_{Epi}$ ) of this intact area.
- (3) The effective radius ( $r_{Epi}$ ) measured in pixels was converted to the effective radius ( $r_E$ ) in millimetres by **Equation (4-24)**. Note that the original radius ( $r_0$ ) for the laboratory tested sample equals 4 mm.

$$r_E = \frac{r_{Epi}}{r_{0pi}} \cdot r_0 \quad (4-24)$$

- (4) The crack length was defined as the difference between the original radius of the sample and the effective radius when the TS test completes. Thus, the crack length ( $c$ ) was obtained by

$$c = r_0 - r_E \quad (4-25)$$

In the above image analysis procedure, the intact area and the effective radius of the sample were objectively measured by the *Circle to Center* tool in Digimizer software. The boundary between the central uncracked zone and the ring cracked zone was defined by users using a circle in software. It was found that difference of crack length determined by different researchers was negligible (less than 5%), which indicates that the boundary definition is relatively objective and reliable. This is because that the boundary between the smooth and rough surfaces is very obvious in the images of cracking surfaces of bitumen sample, as shown in **Figure 4-4**.

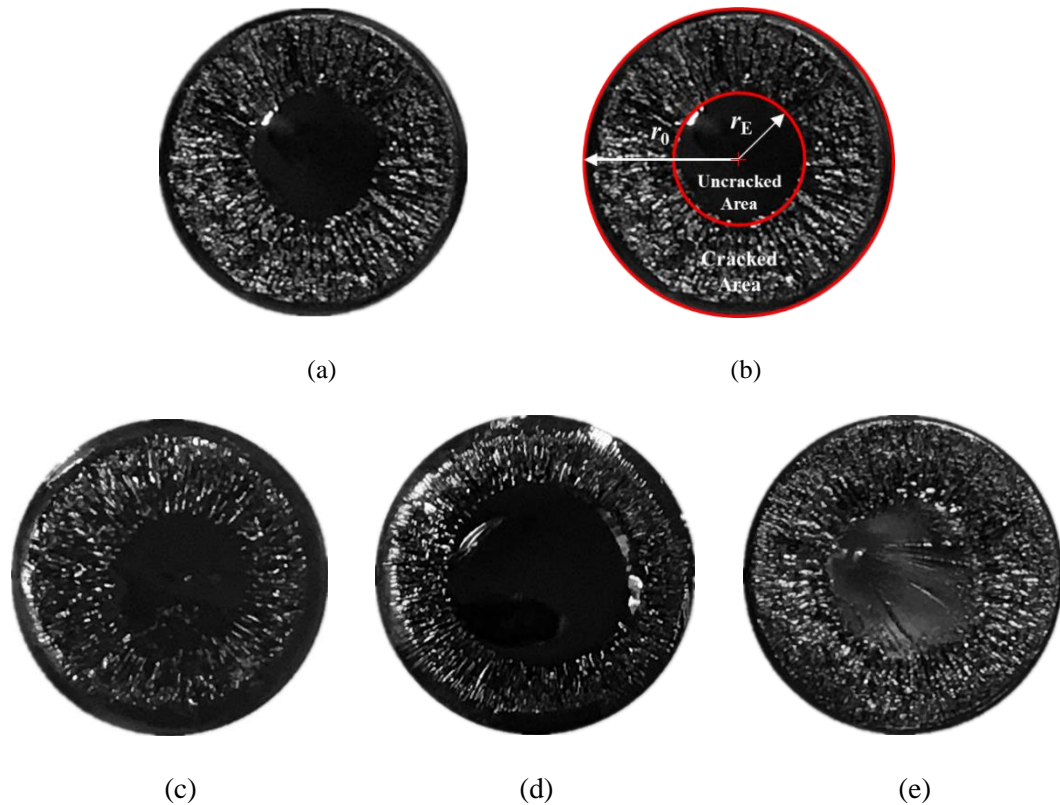


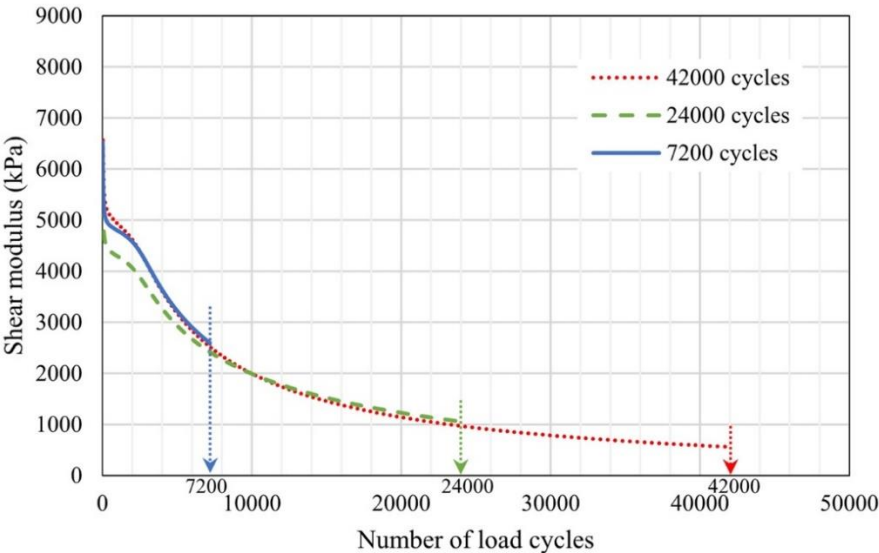
**Figure 4-4 Images of cracking surfaces for bitumen sample after time sweep (TS) tests at 20 °C and 10 Hz. (a) Cracking morphology under 42000 load cycles at 5% strain level for virgin unmodified bitumen 40/60 (B<sub>v</sub>). (b) Definition and measurement of the effective radius and crack length for B<sub>v</sub>. (c) Cracking morphology under 24000 load cycles at 7% strain level for virgin polymer modified bitumen X-70 (A<sub>v</sub>). (d) Cracking morphology under 24000 load cycles at 5% strain level for aged polymer modified bitumen X-70 (A<sub>a</sub>). (e) Cracking morphology under 24000 load cycles at 5% strain level for aged unmodified bitumen 40/60 (B<sub>a</sub>).**

#### 4.7.2 Validation of crack length model

In order to validate the DSR-based crack length (DSR-C) model shown in **Equation (4-23)**, the comparison between the calculated and measured results of the crack length was conducted at varying loading durations (where the test conditions, such as temperature, frequency and strain level were controlled unchanged) and at different testing conditions (where the load cycle was selected as a constant), respectively.

The validation of the prediction model was firstly performed at varying loading durations in terms of load cycles. The TS tests were conducted at a constant strain (5%) loading mode, 20 °C and 10 Hz. Three duplicate samples need to be used to obtain the effective radiuses at three different number of load cycles. The TS test for the first sample was terminated at 7,200

cycles, the sample was pulled apart and the bitumen's cracking surface was imaged, and then the effective radius was measured following the steps in **Section 4.7.1** and the crack length was determined using **Equation (4-25)**. The other two duplicate samples were tested using the same procedure, but terminated at 24,000 and 42,000 load cycles, respectively, to obtain the crack surface images and determine the crack lengths. The shear moduli declining with the number of load cycles for the three samples of the two different bitumen materials (unaged X-70 and unaged 40/60) are presented in **Figure 4-5** on which the crack surface images at the corresponding termination load cycles are also presented. It can be seen that the modulus curves of the three duplicate samples are overlapped each other in general, demonstrating the good repeatability of the fatigue damage tests. With the increase of load cycles, shear modulus declines rapidly at the first 200 load cycles and then starts a relatively slow decrease with the load cycle. The central intact area (defined by the red circles on the crack surface images) became smaller with the increase of load cycle, indicating a growth of crack within the bitumen samples in the TS tests.



7,200 load cycles

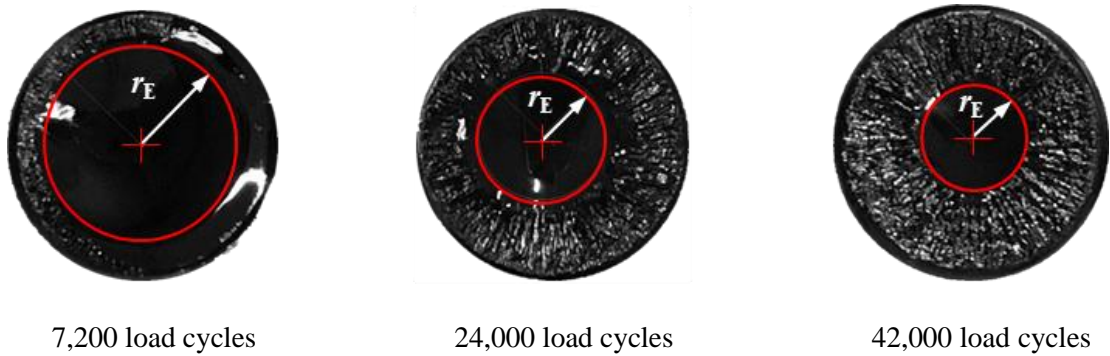
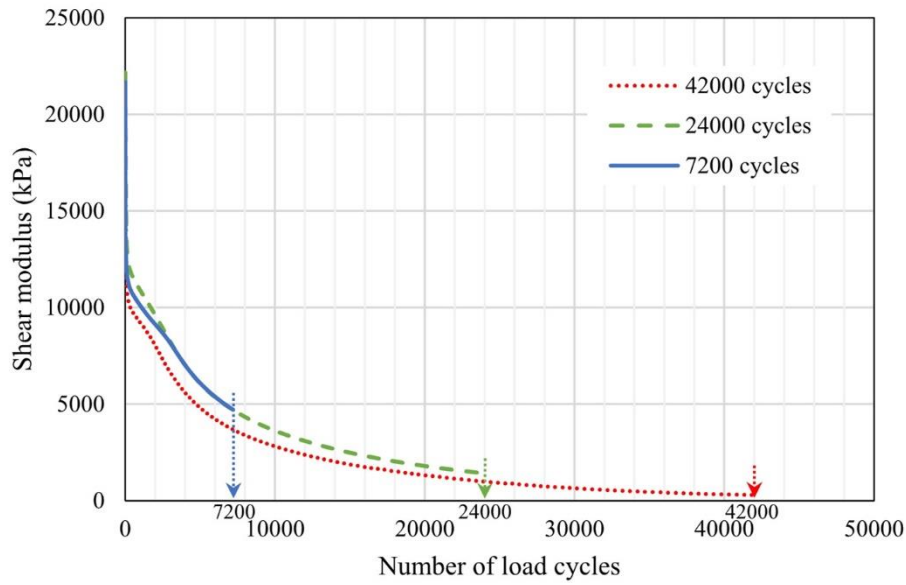


24,000 load cycles



42,000 load cycles

**(a) Polymer modified bitumen X-70**



(b) Unmodified bitumen 40/60

**Figure 4-5 Shear modulus vs. load cycles and crack surface images for three duplicate samples terminated at different load cycles (@ 5% strain level, 20 °C and 10 Hz).**

The predicted effective radius and crack length were calculated by **Equations (4-22)** and **(4-23)**, respectively, where the shear modulus ( $|G^*_0|$ ) and the phase angle ( $\delta_0$ ) of the bitumen in the undamaged condition were obtained from the linear amplitude sweep (LAS) test results and the shear modulus ( $|G^*_N|$ ) and the phase angle ( $\delta_N$ ) of the bitumen in the damaged condition were obtained from the time sweep (TS) tests. The predicted results were compared with the experimental results measured from crack surface images in the TS tests. **Table 4-2** shows the calculated and measured results for the effective radius and crack length under a controlled strain of 5%, 20 °C and 10 Hz, based on the average result of two replicates in each condition. The crack length data were also plotted in **Figure 4-6** to clearly compare the calculated and measured crack length, and the results of the two replicates at each load cycle were presented

to show the consistency of the results. It was found that the predicted results using the **Equation (4-23)** model were in a good agreement (the average difference is within 0.78%) with the experimentally measured results for five of the six conditions, except for the unaged 40-60 bitumen at 7,200 load cycles. The calculated crack length of the unaged 40-60 bitumen at 7,200 load cycles was slightly greater (0.176 mm or 13.69%) than the measured value. This is probably due to the fluctuation of the modulus at the crack initiation stage in the TS test.

**Table 4-2 Calculated vs. measured results for effective radius and crack length in time sweep (TS) tests at different load cycles for two bitumen materials (@ 5% strain level, 20 °C and 10 Hz).**

Materials	Testing conditions		Effective radius (mm)		Crack length (mm)	
			Calculated	Measured	Calculated	Measured
Unaged X-70 bitumen	20°C 10Hz 5% $\gamma$	7200 cycles	3.013	3.044	0.987	0.957
		24000 cycles	2.435	2.433	1.565	1.567
		42000 cycles	2.103	2.091	1.897	1.909
Unaged 40-60 bitumen	20°C 10Hz 5% $\gamma$	7200 cycles	2.534	2.710	1.466	1.290
		24000 cycles	1.857	1.871	2.143	2.129
		42000 cycles	1.403	1.403	2.597	2.597

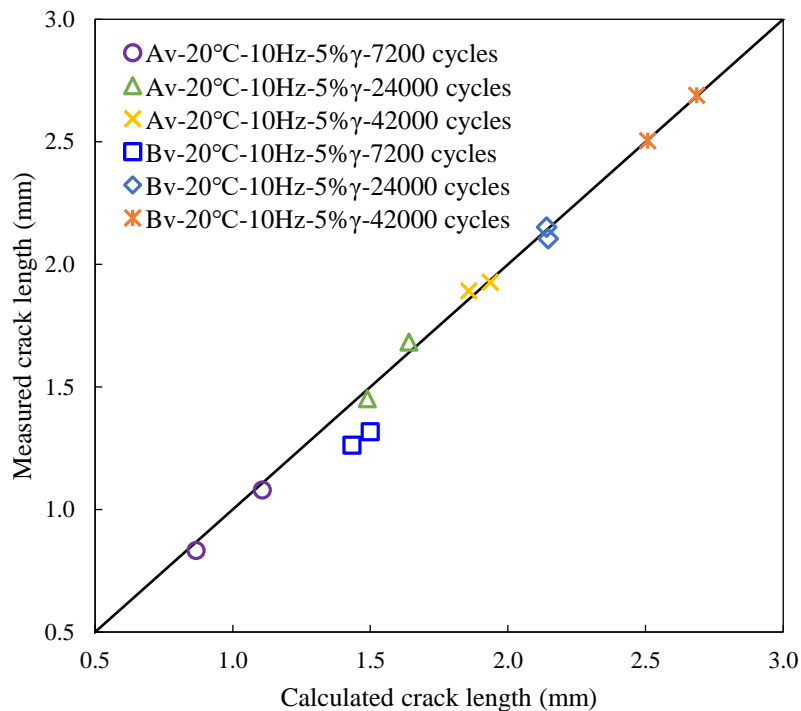


**Figure 4-6 Comparison between calculated and measured crack length in time sweep (TS) tests at different load cycles for two bitumen materials (@ 5% strain level, 20 °C and 10 Hz).**

In addition to the number of load cycles, the DSR-based crack length (DSR-C) model (**Equation 4-23**) was further validated at different testing conditions including temperatures, frequencies and strain levels. Two bitumen materials at unaged and aged conditions were used in the time sweep tests which were all terminated at the same load cycle of 24,000. **Table 4-3** compares the calculated and measured values for effective radius and crack length. **Figure 4-7** shows the comparison between the calculated and measured crack length for the two replicates at each condition. It can be seen that the predicted results agreed well with the experimental measurements with the average difference within 0.68%. This good agreement at different conditions indicates that the developed mechanics-based DSR-C model is capable of accurately predicting the crack length in bitumen under different testing conditions and can be used for quantifying the bitumen's fatigue cracking performance.

**Table 4-3 Calculated vs. measured results for effective radius and crack length in time sweep (TS) tests at different conditions.**

Testing conditions	Effective radius (mm)		Crack length (mm)	
	Calculated	Measured	Calculated	Measured
A <sub>v</sub> -20°C -10Hz-5% $\gamma$ -24000 cycles	2.435	2.433	1.565	1.567
A <sub>v</sub> -15°C -10Hz-5% $\gamma$ -24000 cycles	2.300	2.318	1.700	1.682
A <sub>v</sub> -20°C -20Hz-5% $\gamma$ -24000 cycles	2.356	2.322	1.644	1.678
A <sub>v</sub> -20°C -10Hz-7% $\gamma$ -24000 cycles	1.872	1.860	2.128	2.140
B <sub>v</sub> -20°C -10Hz-5% $\gamma$ -24000 cycles	1.857	1.871	2.143	2.129
A <sub>a</sub> -20°C -10Hz-5% $\gamma$ -24000 cycles	2.285	2.286	1.715	1.714
B <sub>a</sub> -20°C -10Hz-5% $\gamma$ -24000 cycles	1.828	1.823	2.172	2.177

**Table 4-3** and **Figure 4-7** also show that the crack length is greater by 9.32%, 7.34%, 7.04% or 36.53% when the bitumen became aged, the temperature went lower, the loading frequency increased or the strain levels increased. This means the bitumen is subjected to a more severe fatigue damage when the loading level is increased or the material itself becomes relatively stiffer such as undergoing an oxidative ageing, a low temperature, or a high frequency. These observations are consistent with the common understanding and the existing studies of the fatigue behaviour of a bitumen material (Shan et al., 2017, Miró et al., 2015). It is also noted from **Figures 4-6** and **4-7** that the results at each testing condition have a good consistency between the two replicates, which indicate that the variation is minor for the fatigue damage tests done in this study.

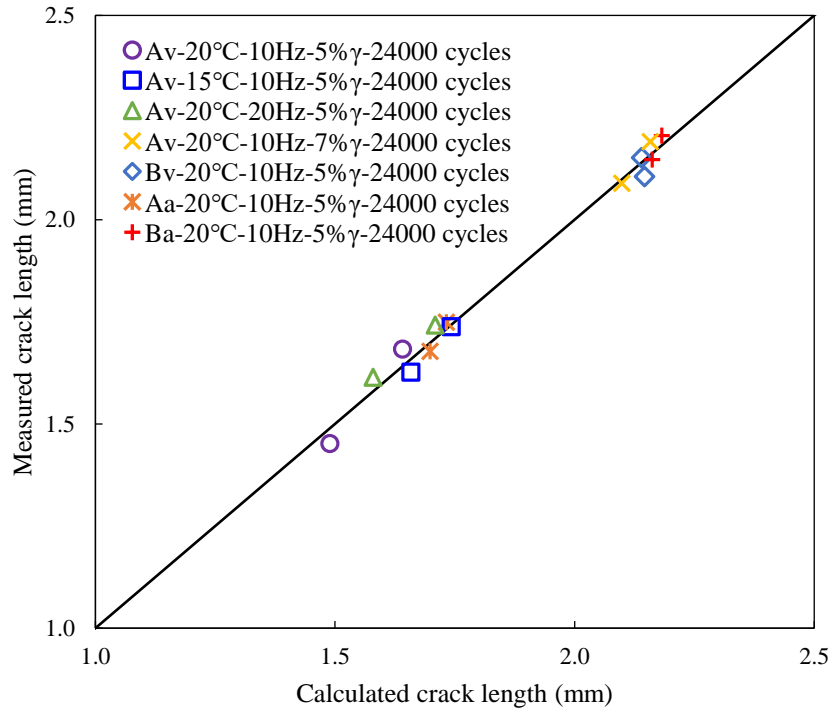


**Figure 4-7 Comparison between calculated and measured crack length in time sweep (TS) tests at different conditions (@ 24,000 load cycles).**

### 4.7.3 Crack growth in bitumen

Based on the developed DSR-C model shown in **Equation 4-23**, the crack growth in the bitumen sample was analysed during the shear fatigue process. **Figure 4-8** shows the crack growth curves of the virgin 40/60 bitumen and the polymer modified X-70 bitumen under a shear fatigue load. It can be seen that the crack length has a sharp increase at the initial stage of the crack growth and then exhibits a relatively stable growth as the number of load cycle increases. This initial unstable crack growth might be caused by the edge flow damage, which will be analysed in **Chapter 5** in detail. After this unstable growth, the crack presents a regular growth. It is also clear from **Figure 4-8** that the virgin 40/60 bitumen and the polymer modified X-70 bitumen showed different fatigue crack length at the stable crack growth stage when subjected to the same loading conditions. The bitumen X-70 which is softer with a lower modulus (see modulus values in **Figure 4-5**) has less crack length compared to the bitumen 40/60 which is relatively stiffer with a greater modulus. Thus, there is a great potential to use the crack length at the stable crack growth stage predicted by DSR-C model to characterise fatigue resistance of different bitumen materials. The stable crack growth of the bitumen will be discussed in **Chapter 6**.

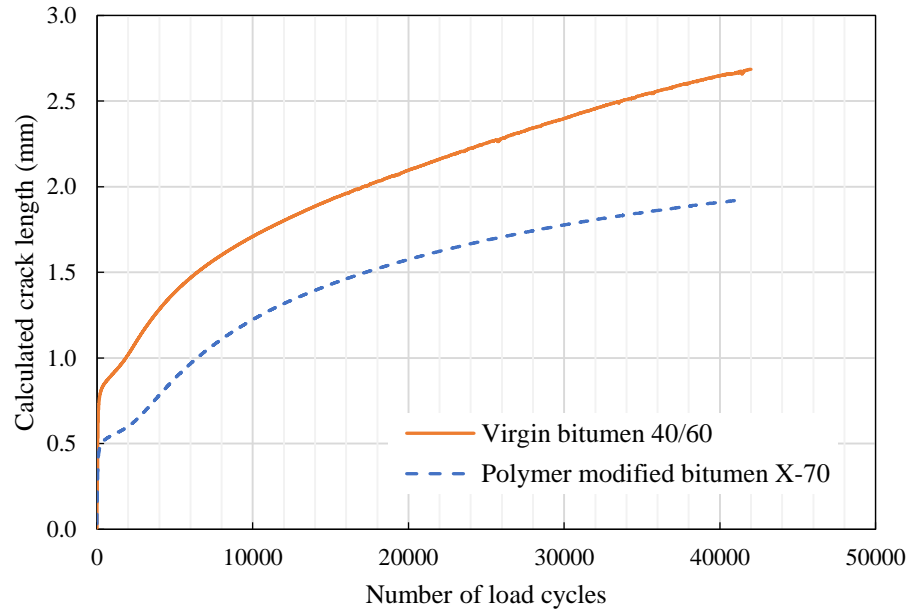


**Figure 4-8 Crack length in bitumen vs. number of load cycle under a rotational shear fatigue load (@ 5% strain level, 20 °C and 10 Hz).**

#### 4.8 Conclusions

This chapter quantified the cohesive debonding behaviour of bitumen due to fatigue using crack length. A dynamic shear rheometer (DSR) based crack length (DSR-C) model was developed for the prediction of crack length in the bitumen specimens subjected to a rotational shear fatigue load. Equilibrium principle of damage mechanics based on the torque and the dissipated strain energy (DSE) was used to construct the DSR-C model to obtain the crack length. The following conclusions were drawn from the research as follows:

- (1) The DSR-based crack length (DSR-C) model based on damage mechanics is capable of accurately predicting the crack length in bitumen under a rotational shear fatigue load at different testing conditions and for different bitumen materials.
- (2) The developed DSR-C model can be applied to investigate the effects of ageing, temperature, loading frequency and strain level (loading amplitude) on the fatigue performance of bitumen. Bitumen will be subjected to a more severe fatigue damage with the increasing crack length by 9.32%, 7.34%, 7.04% or 36.53% in this study when the bitumen became aged, the temperature went lower, the loading frequency increased or the strain level increased.
- (3) The crack length at the stable crack growth stage predicted by DSR-C model can

potentially serve as a direct and fundamental parameter to quantify and differentiate the fatigue performance of various bituminous binders.

# Chapter 5 Microscale Modelling of Cohesive Debonding for Fatigue Crack Initiation in Bitumen

## 5.1 Overview

This chapter aims to model the cohesive debonding in bitumen in order for predicting and modelling the fatigue crack initiation at the microscale. An energy-based crack initiation criterion is developed for the bitumen under a rotational shear fatigue load. Viscoelastic behaviours of the bitumen are firstly characterised by using pseudostrain concept. Based on the analysis of fatigue cracking process using the DSR-C model developed in **Chapter 4**, the crack initiation is defined and local energy redistribution around cracks due to ‘factory-roof’ cracking is quantified. A quantitative energy criterion is proposed for the fatigue crack initiation of the bitumen using the viscoelastic Griffith’s theory. The key model parameter, i.e., cohesive bond energy, is determined by the nanoscale modelling results in **Chapters 2 and 3**. The dynamic shear rheometer (DSR) tests are conducted to determine the remaining model parameters. The crack initiation criterion is validated through comparing the predicted and measured surface energy of the bitumen.

The results show that bitumen fatigue cracking under a rotational shear fatigue load can be divided into two stages: the edge flow damage and the ‘factory-roof’ cracking. The edge flow damage can be regarded as a process including the molecular rearrangements, microcrack nucleation and circumferential crack formation. The energy-based crack initiation criterion along with the DSR fatigue tests can act as a substitute for the surface energy tests.

## 5.2 Introduction

In **Chapter 4**, it was proposed to use the DSR-C model to predict the fatigue crack length in bitumen in order for directly quantifying the cohesive debonding behaviour of the material due to the fatigue load. This Chapter is focused on addressing the second question on when the crack is initiated under the rotational shear fatigue load based on the quantification of cohesive debonding. Crack initiation refers to the onset of the edge fracture, which is critical to estimate crack propagation and fatigue life of the bitumen under the shear fatigue load.

Based on the laboratory observations at the microscale, a number of studies have been carried out to elucidate the mechanisms of crack initiation in metals and polymers. It was found that the crack initiation of metallic materials is mainly caused by dislocations (Brown, 1977).

According to the dislocation movement and plastic deformation, dislocation-based models were proposed to characterise the crack initiation in the metallic materials (Chan, 2003, Tanaka and Mura, 1981, Venkataraman et al., 1991). Polymeric materials are composed of molecular chains, which present a viscoelastic fracture. Its crack initiation results from the chain scission or chain disentanglement. The plastic zone-based model (Bascom et al., 1975, Mai and Cotterell, 1986) or craze zone-based models (Brown and Ward, 1973, Hui et al., 1992, Kambour, 1966) were developed to investigate the crack initiation of polymeric materials.

Furthermore, local crack growth models were proposed for viscoelastic materials including polymers and bitumen, which provide the analytical solutions to crack initiation problems. Knauss (1969) developed a crack speed criterion for viscoelastic materials by defining a critical crack speed transition using continuum mechanics. Schapery (1975) defined a crack tip model with a failure zone behind the tip and developed a local energy criterion for viscoelastic materials to predict the time of crack initiation. While these models can be used to analyse the process of crack initiation, their application in engineering practice, e.g., asphalt mixtures, is limited due to complexity in the determination of the model inputs and the validations of the model predictions.

Griffith's energy criterion presented a more general manner to predict the crack initiation, which defined the energy condition at which the crack is initiated in brittle materials (Griffith, 1921). Recently, Griffith's crack initiation theory has been extended to develop a fracture criterion for the viscoelastic materials (Christensen, 1979, Liang and Zhou, 1997, Nikitin, 1984). Luo et al. (2014) and Zhang et al. (2014) applied viscoelastic Griffith's criterion to develop the crack initiation criteria for the asphalt mixtures in tension and compression, respectively. The tensile crack initiation criterion results in a simple way of measuring the endurance limit and the compressive one leads to a simple way of predicting compressive strength (Lytton et al., 2018). In this study, the viscoelastic Griffith's criterion will be employed to investigate the crack initiation for the bitumen under the rotational shear fatigue loads.

The objective of this study is to develop an energy-based crack initiation criterion for the bitumen subjected to a rotational shear fatigue load so that the initiation of the cohesive debonding can be determined at the microscale. Viscoelasticity of the bitumen is firstly characterised by using pseudostrain concept. Based on the analysis of fatigue cracking process, the crack initiation is defined and energy redistribution due to 'factory-roof' cracks is illustrated. Subsequently, an energy criterion for the crack initiation of the bitumen under the rotational shear fatigue load is developed using the viscoelastic Griffith's criterion. The model parameters are determined by the nanoscale modelling results and the DSR laboratory tests. The predicted

surface energy based on the crack initiation criterion is compared against the experimental data from contact angle measurements to validate the developed criterion.

### 5.3 Viscoelastic Characterisation of Bitumen with Pseudostrain

When a viscoelastic material is subjected to a rotational shear fatigue load, its stress-strain curve forms a hysteresis loop in each load cycle. The area inside the loop is the dissipated strain energy (DSE) density and the area between the stress-strain curve and the horizontal (strain) axis is defined as the recoverable strain energy (RSE) density. The DSE for the materials in the linear viscoelastic undamaged state is the energy dissipated due to the viscoelastic relaxation of the material. In order to remove the viscous effect, pseudostrain was proposed by Schapery (1984) below

$$\gamma^R(t) = \frac{1}{G_R} \int_0^t G(t-s) \frac{d\gamma(s)}{ds} ds \quad (5-1)$$

where  $\gamma^R$  is the pseudostrain;  $G_R$  is the shear reference modulus;  $G(t)$  is the shear relaxation modulus;  $s$  is the time before the current time  $t$ ; and  $\gamma(s)$  is the measured total strain. Pseudostrain has been used in the damage characterization of asphalt mixtures (Zhang et al., 2011, Zhang et al., 2012, Zhang et al., 2013, Zhang et al., 2014). After introducing pseudostrain, the stress-pseudostrain curve at the linear viscoelastic state becomes a straight line, which indicates that the viscous effect is eliminated and the stress-pseudostrain shows like an elastic behaviour. The area below the stress-pseudostrain curve is the recoverable pseudostrain energy (RPSE) density. RPSE is the density of the energy stored in the material during loading and can be released during unloading, which is used for crack initiation analysis of the bituminous binders under rotational a shear fatigue load in this study.

In a strain-controlled rotational shear fatigue test (e.g., time sweep test) of a cylindrical bitumen sample, the applied shear strain is

$$\gamma(t) = \gamma_0 \sin(\omega t) \quad (5-2)$$

where  $\gamma_0$  is the strain amplitude and  $\omega$  is the loading frequency. The strain amplitude at a given radial position of the sample is expressed as

$$\gamma_0(r) = \frac{\theta_0}{h} \cdot r \quad \text{with } 0 \leq r \leq r_0 \quad (5-3)$$

where  $\theta_0$  is the controlled amplitude of rotational angle,  $r_0$  and  $h$  are the original radius and the

height of the cylindrical sample, respectively. Thus, in the strain-controlled cyclic test, the pseudostrain  $\gamma^R(t)$  in **Equation (5-1)** at the linear viscoelastic condition can be determined as

$$\gamma^R(t) = \frac{\gamma_0}{G_R} |G_0^*| \sin(\omega t + \delta_0) \quad (5-4)$$

where  $\delta_0$  is the phase angle of the material in the undamaged condition. The corresponding pseudostrain amplitude is written as

$$\gamma_0^R = \frac{\gamma_0}{G_R} |G_0^*| \quad (5-5)$$

Based on the definition of RPSE density that is the area between the stress-pseudostrain curve and the horizontal (pseudostrain) axis, the value of RPSE density at a given radial position of the sample at the linear viscoelastic condition can be calculated as

$$RPSE(r) = \frac{1}{2} \tau_0 \cdot \gamma_0^R \quad (5-6)$$

where  $\tau_0$  is the amplitude of the measured shear stress corresponding to the controlled shear strain  $\gamma(t)$  shown in **Equation (5-2)**. According to the linear viscoelastic stress-strain law, the shear stress amplitude of the sample can be obtained by

$$\tau_0 = |G_0^*| \gamma_0 = G_R \gamma_0^R \quad (5-7)$$

Substituting **Equations (5-5)** and **(5-7)** into **Equation (5-6)** and considering **Equation (5-3)**, RPSE density at a given radial position of the cylindrical bitumen sample can be given as

$$RPSE(r) = \frac{1}{2} \frac{(|G_0^*| \theta_0)^2}{G_R h^2} \cdot r^2 \quad (5-8)$$

From **Equation (5-8)**, one can find that the RPSE density is non-uniform along the radial direction of the cylindrical bitumen sample but a quadratic function of the radius  $r$  for the sample. The maximum RPSE occurs at the location where the radius is the maximum which is the edge of the sample. This again proves that the crack tends to be initiated from the edge of the sample.

## 5.4 Definition of Fatigue Crack Initiation in Bitumen

According to the discussion and findings in **Chapter 4**, under a rotational shear fatigue load, the crack in a cylindrical bitumen sample grows as a circumferential crack that initiates at the edge of the sample and propagates toward the centre. A typical fracture surface in the bitumen samples is shown in **Figure 5-1(a)**. It can be seen that the crack surface exhibits three different zones based on the morphology of cracking surfaces:

- (1) Edge flow zone. The damage at the edge flow zone is known as ‘edge flow’ that occurs at the edge of the sample and at the initial stage of fatigue cracking. The edge flow is caused by edge instability with complex mechanisms.
- (2) ‘Factory-roof’ cracking zone. At the ‘factory-roof’ cracking zone, the crack is a single ring crack that steadily propagates towards the centre of the sample, resulting in a rough and ‘factory-roof’ like cracking surface under the shear-mode loading.
- (3) Uncracked zone. The uncracked zone is the zone in the sample centre which was not damaged during the rotational shear fatigue load. However, it was generated and captured by pulling the top and bottom sample apart after the fatigue test at a relatively low temperature (i.e., 3 °C). The low-temperature was used to conserve the configuration of the crack surfaces including flow zone crack and the ‘factory-roof’ crack generated during the fatigue test.

Thus, bituminous binders’ fatigue cracking under the rotational shear fatigue load can be divided into two stages: edge flow damage and ‘factory-roof’ cracking. **Figure 5-1(b)** shows the schematic side view of a cylindrical sample with a circumferential crack.

Using the DSR-C model shown in **Equation (4-23)**, the crack growth in bituminous binders under a rotational shear fatigue load can be predicted using the moduli and phase angles of the binders in the undamaged and damaged conditions. **Figure 5-2** shows a typical crack growth curve with the number of load cycles. The corresponding crack growth rate with the crack length is plotted in **Figure 5-3**. It is very clear from **Figures 5-2** and **5-3** that, after the 1000<sup>th</sup> load cycles or the crack length of 0.55 mm, the crack presented a regular growth and the crack growth rate slightly increased and then steadily decreased. This crack growth stage is referred to as the crack propagation (‘factory-roof’ cracking), which will be investigated in **Chapter 6**. Before the crack propagation stage, the initial portion of fatigue cracking is believed as the edge flow damage.

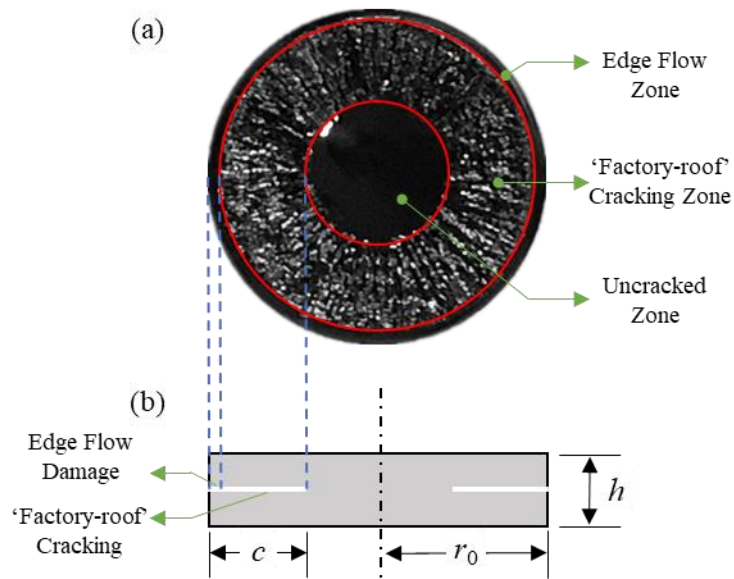


**Figure 5-1 Fatigue cracking in bituminous binders under a rotational shear fatigue load. (a) Cracking morphology. (b) Cracking model.  $c$  is the crack length,  $r_0$  is the original radius of sample, and  $h$  is the height of sample.**

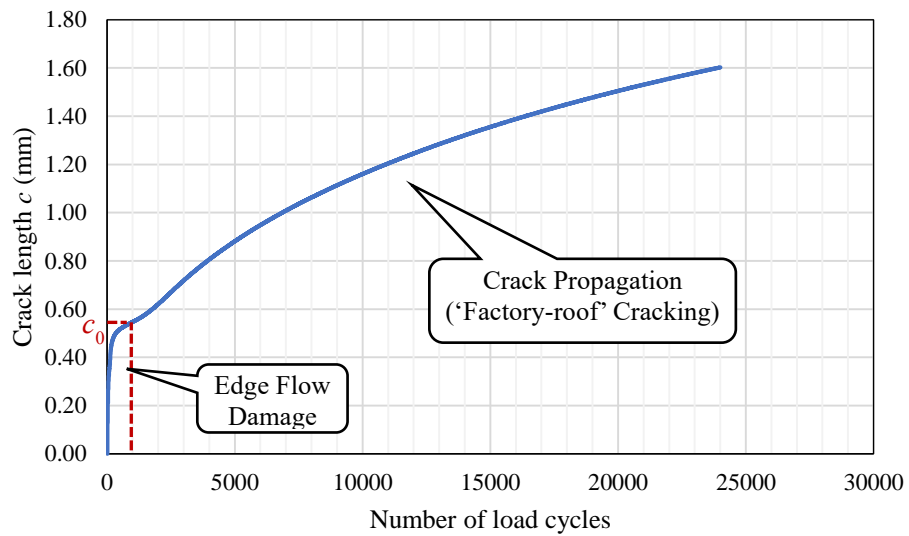


**Figure 5-2 Crack growth with the number of load cycles for a cylindrical bitumen sample subjected to a rotational shear fatigue load.**

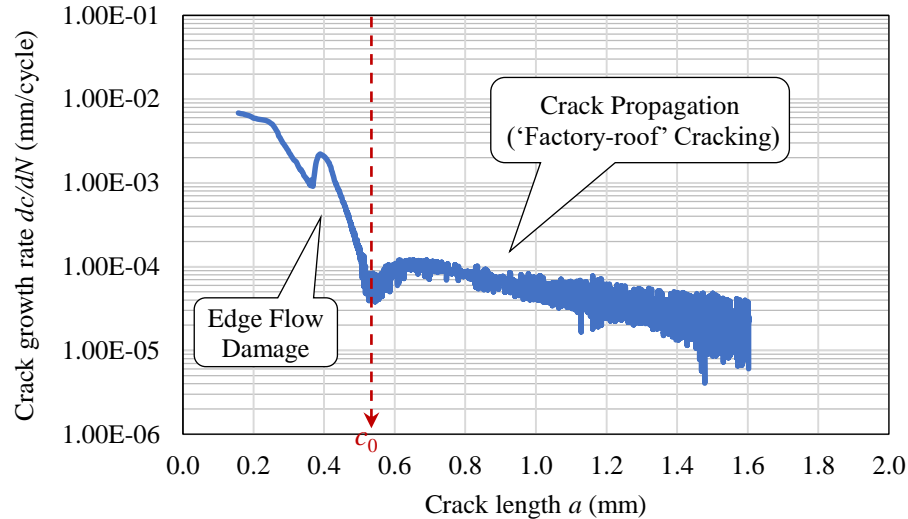


**Figure 5-3 Crack growth rate with the crack length for a cylindrical bitumen sample subjected to a rotational shear fatigue load.**

Edge flow damage is an unsteady cracking stage with complex cracking mechanisms. It can be seen from **Figures 5-2** and **5-3** that the crack length has a sharp increase and the crack growth rate shows a significant fluctuation. A sequence of processes occurring in this stage are described as follows:

- (1) Molecular rearrangements. When the bituminous binders are subjected to the external rotational shear fatigue load, their physical properties such as shear modulus and phase angle changes rapidly (see **Figures 4-3** and **5-5**). This phenomenon is caused by the rearrangement of molecular chains in binders (Schmets et al., 2009, Jahangir et al., 2015), which is referred to as the thixotropic effect (Shan et al., 2010).
- (2) Microcrack nucleation. After the molecular rearrangements, the microcracks are initiated at the edge of cylindrical bitumen sample either by the breakage of atomic bonds or from the pre-existing vacancies and flaws in the materials. These microcracks then occur nucleation and form small macrocracks (Doremus, 1976).
- (3) Circumferential crack formation. With the increasing load cycles, small macrocracks are eventually interconnected to generate a single circumferential crack at the edge of sample. The initial circumferential crack length  $c_0$  is defined as the edge flow damage size which separates the crack growth rate into completely two different stages. As shown in **Figure 5-3**, the crack growth rate is much higher but drops much quicker in the edge flow damage stage than that in ‘factory-roof’ crack propagation stage.

Due to the edge instability and geometry dependence of samples, it becomes very challenging to develop a rigorous model or theory to characterise the molecular rearrangements or the microcrack nucleation during the edge flow damage. However, after the circumferential crack formation, the ‘factory-roof’ crack propagates at a relatively stable and more consistent manner as shown in **Figures 5-2** and **5-3**. Thus in this study the “crack initiation” is defined as the moment at which the circumferential crack formation is complete, which is also the end of the edge flow damage and the start of the ‘factory-roof’ crack propagation. **Figure 5-4** is proposed to model the crack initiation, at which the edge flow damage stage has been finished, thus the crack size has reached a length of  $c_0$ .

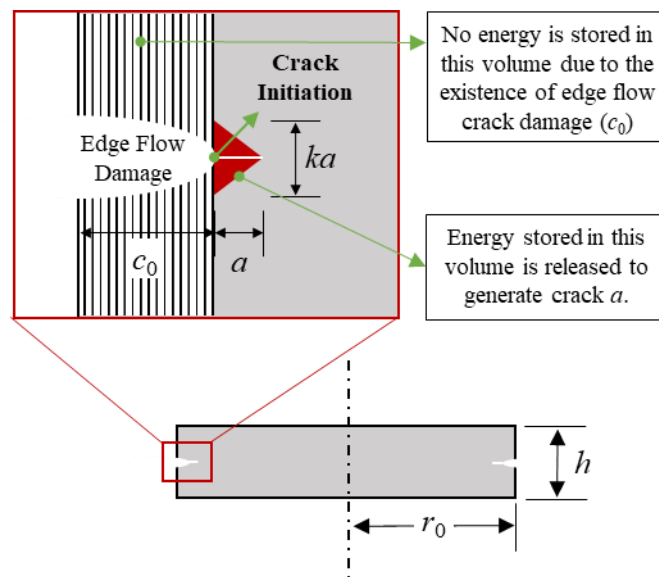


**Figure 5-4** Edge flow damage and crack initiation of ‘factory-roof’ cracking zone.  $c_0$  is the edge flow damage size.  $a$  is the ‘factory-roof’ crack length for crack initiation.

## 5.5 Modelling Fatigue Crack Initiation in Bitumen Using Griffith’s Criterion

### 5.5.1 Energy redistribution due to ‘factory-roof’ cracking

Cracking is a process of energy redistribution in material according to Griffith theory. For bituminous binder, a viscoelastic material, pseudostrain is applied to replace the physical strain so that a viscoelastic problem could be simplified as an elastic one.

According to the cracking pattern of bitumen binders under the rotational shear fatigue load shown in **Figures 5-1** and **5-4**, the total RPSE in bitumen sample with the edge flow damage is redistributed due to the appearance of the circumferential ‘factory-roof’ crack as

follows: (1) RPSE is released from the intact material surrounding the ‘factory-roof’ crack and (2) surface energy is stored on the surfaces of the ‘factory-roof’ crack. Thus, the energy redistribution resulting from the ‘factory-roof’ cracking is formulated as

$$\varepsilon = \varepsilon_1 - \varepsilon_2 + \varepsilon_3 \quad (5-9)$$

where  $\varepsilon$  is the total pseudostrain energy after the energy redistribution in the cylindrical bitumen sample;  $\varepsilon_1$  is the total RPSE in the sample with the edge flow damage before the circumferential ‘factory-roof’ crack initiates;  $\varepsilon_2$  is the released RPSE surrounding the circumferential ‘factory-roof’ crack; and  $\varepsilon_3$  is the total surface energy stored on the ‘factory-roof’ crack surfaces.

To analyse the energy redistribution in bitumen sample, the three energy elements ( $\varepsilon_1$ ,  $\varepsilon_2$  and  $\varepsilon_3$ ) were further derived based on the cracking model of bitumen sample shown in **Figure 5-4**. The total RPSE in the sample with the edge flow damage before the ‘factory-roof’ crack initiates (i.e.,  $\varepsilon_1$ ) is defined as

$$\varepsilon_1 = \iiint_{V_{total}} RPSE(r) dV = \int_0^{r_0-c_0} RPSE(r) \cdot (2\pi rh) dr \quad (5-10)$$

where  $V_{total}$  is the volume of the sample except the edge flow damage zone (the vertically shaded part shown in **Figure 5-4**). Note that the edge flow damage zone was removed from the calculation of the  $V_{total}$  as no RPSE was stored in the zone due to the edge flow damage in the sample.

The released RPSE surrounding the ‘factory-roof’ crack (i.e.,  $\varepsilon_2$ ) is calculated as

$$\varepsilon_2 = \iiint_{V_{releasesad}} RPSE(r) dV \approx RPSE(r) \cdot V_{releasesad} \quad (5-11)$$

where  $V_{released}$  is the volume of the sample that releases RPSE to generate the ‘factory-roof’ crack. As shown in **Figure 5-4**, when a very small ‘factory-roof’ crack  $a$  ( $a \ll c_0$ ) is initiated, only the energy stored in the adjacent volume of the crack is released. It was assumed that this volume is a triangular ring region and highlighted as the red area as shown in **Figure 5-4**. The horizontal height of the triangular region is the crack length  $a$  and the vertical height of the triangular region is  $ka$  according to the previous study (Gent and Yeoh, 2003). Thus, the volume for releasing RPSE can be expressed as

$$V_{released} = \frac{1}{2} \cdot ka \cdot a \cdot 2\pi(r_0 - c_0) \quad (5-12)$$

The total surface energy stored on the ‘factory-roof’ crack surfaces  $\varepsilon_3$  is determined as

$$\varepsilon_3 = \Delta G^c \cdot A = \Delta G^c \cdot \left[ \pi(r_0 - c_0)^2 - \pi(r_0 - c_0 - a)^2 \right] \quad (5-13)$$

where  $\Delta G^c$  is cohesive bond energy of the bitumen and  $A$  is the surface area of a circumferential crack. The cohesive bond energy  $\Delta G^c$  is defined as the energy required to create two new surfaces by the separation of the material and its value equals to two times of the surface energy (**Equation 2-14**), which has been modelled at the nanoscale in **Chapters 2** and **3**.

### 5.5.2 Crack initiation criterion

The Griffith crack initiation criterion states that the potential energy of an elastic body remains unchanged when cracks initiate or the existing cracks grow. Thus, the crack initiation follows an energy balance condition, where the rate of total energy to crack size equals to zero. Based on this criterion, the critical condition at the moment when the crack is initiated can be expressed as

$$\frac{\partial \varepsilon}{\partial c} = 0 \quad (5-14)$$

where  $\varepsilon$  is the total pseudostrain energy after the energy redistribution in the sample shown in **Equation (5-9)**. Thus, substituting **Equation (5-9)** with **Equations (5-10)**, **(5-11)**, **(5-12)**, and **(5-13)** into **Equation (5-14)** and performing differentiation give

$$RPSE(r) \cdot k \cdot a \cdot (r_0 - c_0) - \Delta G^c (r_0 - c_0 - a) = 0 \text{ with } r = r_0 - c_0 \quad (5-15)$$

**Equation (5-15)** is the energy-based crack initiation criterion for the bitumen under the rotational shear fatigue load.

## 5.6 Materials and Laboratory Tests

The unmodified bitumen 40/60 and the polymer-modified bitumen X-70 were applied in this study. The aged binders for bitumen 40/60 and bitumen X-70 were obtained by Thin-Film Oven Test (TFOT). Following the procedure described in **Section 4.6**, the tested bitumen samples were prepared using a silicone mould. All the tests were conducted using a Kinexus DSR from Malvern Panalytical with an 8 mm parallel plates with 2 mm gap as the sample

height. To determine the linear viscoelastic properties and fatigue cracking behaviour of the bituminous binders, viscoelastic frequency sweep (FS) tests and time sweep (TS) fatigue tests were performed on the four binders in this study. Two replicates were tested for each testing condition and one more replicate was required when their deviation was more than 10%.

Frequency sweep tests were conducted at a temperature of 20 °C and frequencies range from 1 to 25 Hz under a 0.5% shear strain level. The shear modulus ( $|G_0^*|$ ) and the phase angle ( $\delta_0$ ) of the undamaged binders can be obtained from the frequency sweep tests. To study the fatigue cracking behaviour of the binders, time sweep fatigue tests were performed at the temperature of 20 °C and frequency of 10 Hz under a 5% shear strain level corresponding to the rotation amplitudes of 0.025 rad. The strain level (5%) have been employed for time sweep fatigue tests in the literature (Wang et al., 2016) to investigate the fatigue damage response of bituminous binders. The testing temperature (20 °C) was selected within the intermediate temperature range where fatigue cracking commonly happens. **Figure 5-5** illustrates a typical result of the time sweep test for an aged X-70 bitumen sample.

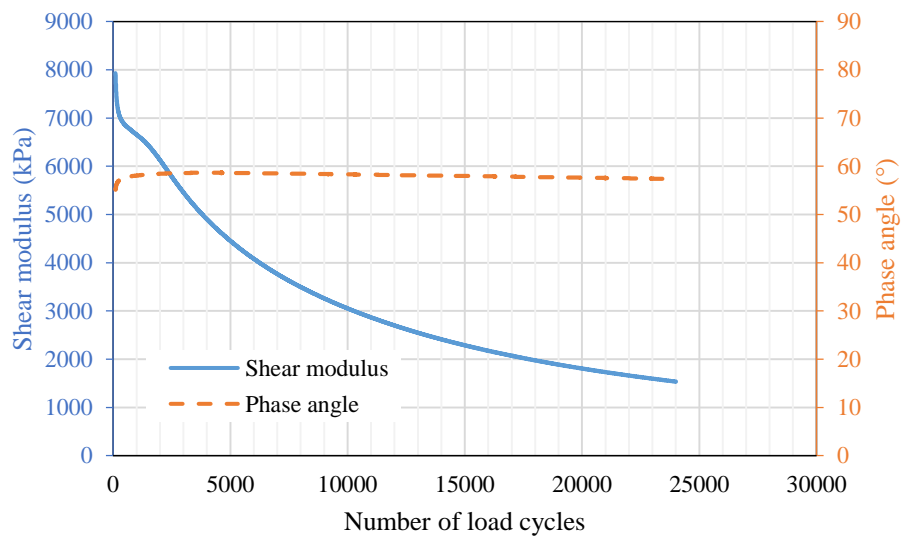


**Figure 5-5 Time sweep (TS) test results at 5% strain, 20 °C and 10 Hz for an aged X-70 bitumen sample.**

## 5.7 Results and Discussion

### 5.7.1 Determination of model parameters

To implement the energy-based crack initiation criterion for the bitumen in **Equation**

(5-15), the model parameters are discussed and determined in this section.

The recoverable pseudostrain energy density  $RPSE(r)$  is calculated using **Equation (5-8)** with the crack initiation position  $r = r_0 - c_0$ . More specifically, the shear modulus  $|G_0^*|$  in the undamaged condition is obtained from the frequency sweep tests. The controlled amplitude of rotational angle  $\theta_0$  is 0.025 rad. The shear reference modulus  $G_R$  is determined as the shear modulus  $|G_0^*|$ . A previous study (Zhang et al., 2011) proved that, when assigning the material modulus to the reference modulus, the physical meaning of the pseudostrain becomes the difference between the viscous strain and the total strain. It is noted that some studies (Lee and Kim, 1998, Gibson et al., 2003) used a unit (1 Pa) as the reference modulus, however, this will result in an unclear physical meaning of the pseudostrain as the unit reference modulus has normalised the pseudostrain when the stress-pseudostrain relations are modelled.

The cohesive bond energy  $\Delta G^c$  is determined based on the nanoscale modelling results in **Chapters 2 and 3**. The edge flow damage size  $c_0$  is determined as the corresponding crack length at which the minimum crack growth rate was obtained before the “factory-roof” crack propagation is started in the TS tests, as shown in **Figure 5-3**. The radius  $r_0$  and the height  $h$  of the cylindrical bitumen sample are 4 mm and 2 mm, respectively.

The coefficient  $k$  of the vertical height  $ka$  in the triangular region shown in **Figure 5-4** is determined as  $2\pi$  (Luo et al., 2014). Note that the ‘factory-roof’ crack length  $a \ll c_0$  at the critical moment of the crack initiation, thus it is assumed that the crack length  $a = \alpha \cdot c_0$  where  $\alpha$  is within a range from 0.0001 to 0.0012 depending on the modulus of the tested bitumen samples. Thus, the crack initiation occurs at the microscale.

### 5.7.2 Implementation in prediction of surface energy

To validate the crack initiation criterion, **Equation (5-15)** is used to predict the surface energy of the bitumen. Based on **Equation (5-8)**,  $RPSE(r)$  at the crack initiation position  $(r_0 - c_0)$  is written as

$$RPSE = \frac{1}{2} \frac{(|G_0^*| \theta_0)^2}{G_R h^2} \cdot (r_0 - c_0)^2 \quad (5-16)$$

Then, substituting **Equations (5-16)** and **(2-14)** into **Equation (5-15)** and using  $r_0 - c_0 - a \approx r_0 - c_0$  due to  $a \ll c_0$  for the crack initiation, the surface energy of the bitumen can

be calculated by

$$\Gamma = \frac{\left(|G_0^*|\theta_0\right)^2 \cdot k \cdot a \cdot (r_0 - c_0)^2}{4G_R h^2} \quad (5-17)$$

**Figure 5-6** presents the comparison between the calculated results from **Equation (5-17)** and the tested results from the contact angle measurements shown in **Tables 2-4** and **3-3**. It can be seen that the predicted results agree well with the tested data for all tested bitumen samples, which indicate that the energy-based crack initiation criterion can be used to determine the surface energy of the bitumen by the DSR fatigue tests. Thus, the energy-based crack initiation criterion along with the DSR fatigue tests can act as a substitute for surface energy tests.

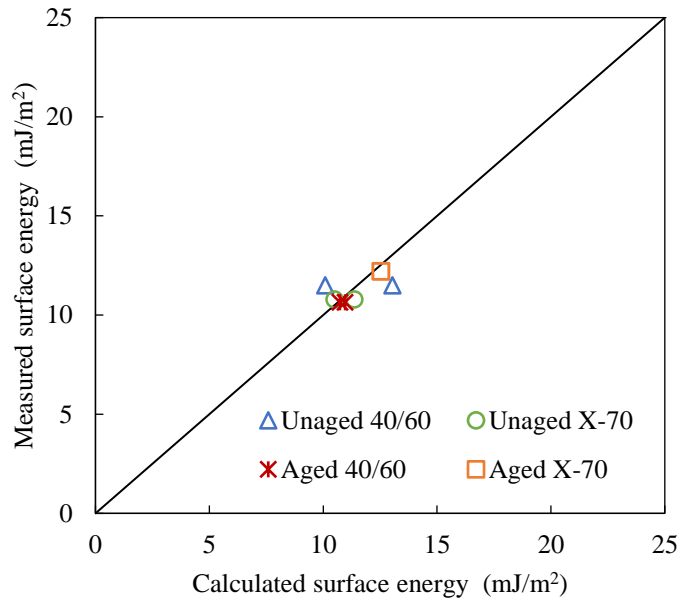


**Figure 5-6 Comparison between the calculated results and the tested data from the contact angle measurements.**

## 5.8 Conclusions

In this chapter, the cohesive debonding for fatigue crack initiation in bitumen is modelled at the microscale. An energy-based crack initiation criterion is developed for the bitumen subjected to a rotational shear fatigue load based on mechanics principles and physical facts during the crack initiation process. Laboratory tests are conducted to determine the model parameters. The crack initiation criterion is validated through comparing the predicted and

measured surface energy of the bitumen. The major contributions of this study are summarised as follows:

- (1) Bitumen fatigue cracking under a rotational shear fatigue load can be divided into two stages: the edge flow damage and the ‘factory-roof’ cracking.
- (2) The edge flow damage can be regarded as a process including the molecular rearrangements, microcrack nucleation and circumferential crack formation.
- (3) The local energy redistribution due to the circumferential ‘factory-roof’ crack is quantified by the pseudostrain energy. A crack initiation criterion is developed for bitumen under a rotational shear fatigue load based on viscoelastic Griffith fracture mechanics.
- (4) The energy-based crack initiation criterion along with the DSR fatigue tests can act as a substitute for the surface energy tests.

# Chapter 6 Macroscale Modelling of Cohesive Debonding for Fatigue Crack Propagation in Bitumen\*

## 6.1 Overview

This chapter aims to model the cohesive debonding in bitumen in order for evaluating the fatigue crack propagation at the macroscale. The fatigue crack length in the bitumen under a rotational shear fatigue load is determined using the damage mechanics-based DSR-C model developed in **Chapter 4** which is a function of the shear moduli and phase angles in undamaged and damaged conditions. The crack evolution is modelled by a pseudo J-integral based Paris' law. A virgin bitumen 40/60 and a polymer-modified bitumen X-70 under unaged and aged conditions are employed for time sweep (TS) fatigue tests using dynamic shear rheometer (DSR) at different temperatures, frequencies and strain levels.

Results show that the pseudo J-integral Paris' law is able to accurately predict the crack evolution in bitumen under the rotational shear fatigue load. The crack grows faster for the aged bitumen or at lower temperatures. The Paris' law model parameters are function of temperatures but independent of loading frequency or loading amplitude. They are fundamental material properties and can be determined at one loading frequency and amplitude, then can be implemented to predict crack propagation of the bitumen at different loading frequencies or amplitudes.

## 6.2 Introduction

Once the fatigue crack is initiated in bitumen under the rotational shear fatigue load discussed in **Chapter 5**, the following question on how the crack evolves is raised and answered in this Chapter based on the quantification of cohesive debonding described in **Chapter 4**. Crack propagation fundamental dominates the fatigue life of the bitumen under the shear fatigue load.

Hintz and Bahia (2013b) analysed the crack growth and developed a failure criterion

---

\* Reprinted with permission from SAGE: **Y. Gao**, L. Li, Y. Zhang. (2020). Modelling crack propagation in bituminous binders under a rotational shear fatigue load using pseudo J-integral Paris' law. *Transportation Research Record: Journal of the Transportation Research Board*. DOI: 10.1177/0361198119899151

for estimating the fatigue resistance of bituminous binders. Nuñez et al. (2016) commented that this criterion needs further development to account for the load and strain level associated with the failure crack length. They investigated the crack growth of modified bituminous binders using the finite element model and presented a new criterion to estimate their fatigue characteristics. Shan et al. (2017) studied the crack growth in bituminous binders under the controlled-stress mode and controlled-strain mode. These studies on crack growth were all based on the torque predictions of crack length. However, it has been proved that the calculated crack lengths based on the torque prediction were inaccurate when the dynamic modulus ( $G^*$ ) value of the material falls to 10% of its initial value (Shan et al., 2017). To better understand the crack evolution, there is a need to fundamentally investigate the crack growth rate for the bituminous binders under a rotational shear fatigue load.

Paris' law proposed by Paris and Erdogan (1963) is widely employed to describe the crack growth in engineering materials due to fatigue. It establishes a power relationship between the crack growth rate and the stress intensity factor, as shown in **Equation (6-1)**.

$$\frac{dc}{dN} = A(\Delta K)^n \quad (6-1)$$

where  $c$  is the crack size;  $dc/dN$  is the crack growth rate;  $\Delta K$  is the stress intensity factor per load cycle; and  $A$  and  $n$  are the fracture coefficients.  $K$  quantifies the stress state near the crack tip. The Paris' law is normally used for the characterisation of the fatigue crack growth of elastic materials such as ceramics, metals or concrete. To characterise the crack propagation of viscoelastic materials, Schapery (1984) suggested replacing the stress intensity factor with a pseudo J-integral. Based on Schapery's viscoelastic damage theory (Schapery, 1984), the Paris's law is then modified as

$$\frac{dc}{dN} = A(\Delta J_R)^n \quad (6-2)$$

where  $\Delta J_R$  is the incremental pseudo J-integral defined as the pseudostrain energy release rate. The pseudo J-integral quantifies the change rate of the dissipated energy due to the crack growth in the viscoelastic materials and eliminates the viscous effect on the crack growth.

The pseudo J-integral Paris' law has been extensively used to investigate the fatigue crack evolution of asphalt mixtures in tension and compression (Lytton et al., 2018). Luo et al. employed the pseudo J-integral Paris' law to predict fatigue crack growth in the asphalt mixtures in tension (Luo et al., 2013, Luo et al., 2016). Zhang et al. characterised fatigue cracking

damage of the asphalt mixtures under compressive loads using the pseudo J-integral Paris' law (Zhang et al., 2012, Zhang et al., 2013, Zhang et al., 2018). In these studies, a damage density was used to replace the crack length  $c$  to quantify the fatigue damage based on continuum damage mechanics (CDM). It was concluded that the pseudo J-integral Paris' law is able to model the fatigue crack evolution and to capture the fatigue cracking properties of the viscoelastic materials, e.g., asphalt mixtures.

The objective of this study is to develop a crack propagation model at the macroscale to predict the crack evolution in bitumen under a rotational shear fatigue load. The DSR-C model is employed to calculate the crack length in the cylindrical bitumen samples and then the crack growth rate is obtained. The energy release rate is derived based on dissipated pseudostrain energy (DPSE). The crack evolution is modelled by a pseudo J-integral based Paris' law. Time sweep (TS) fatigue tests are conducted by using dynamic shear rheometer (DSR). The Paris' law coefficients are analysed under different temperature, loading frequency and strain level conditions.

### 6.3 Dissipated Pseudostrain Energy (DPSE) for Crack Growth

Bitumen is a kind of viscoelastic material. When bitumen is subjected to a rotational shear fatigue load, the stress versus strain curve follows a hysteresis loop during the loading and unloading processes in each cycle. The area inside the loop is the dissipated strain energy (DSE). The DSE in the undamaged viscoelastic state is the energy consumed for viscoelastic relaxation of the materials. When the bitumen sample is damaged, the DSE is the total energy expended for the viscous and damage effects of the materials. After introducing pseudostrain shown in **Equation (5-1)**, the stress versus pseudostrain curve in a linear viscoelastic state becomes a straight line with no enclosed area. In a nonlinear viscoelastic state, the stress versus pseudostrain curve becomes a loop. The enclosed area in the loop represents the energy consumed for the nonlinearity of bitumen, defined as the dissipated pseudostrain energy (DPSE).

To determine the dissipated pseudostrain energy (DPSE) in the  $N$ th load cycle of bitumen, the pseudostrain in the damaged condition is first derived. In a strain-controlled cyclic rotational test, the shear strain in the damaged condition is expressed as

$$\gamma_d(t) = \gamma_d \sin(\omega t) \quad (6-3)$$

where  $\gamma_d$  is the shear strain amplitude and  $\omega$  is the loading frequency. The strain amplitude at a given radial position in a cylindrical bitumen sample is defined as

$$\gamma_d(r) = \frac{\theta_0}{h} \cdot r \text{ with } 0 \leq r \leq r_0 \quad (6-4)$$

where  $\theta_0$  is the amplitude of rotational angle that is controlled by DSR directly and  $h$  is the height of the cylindrical sample.

Taking into account **Equation (6-3)** in **Equation (5-1)**, the pseudostrain  $\gamma_d^R(t)$  in the damaged condition in a strain-controlled cyclic rotational test can be then derived as

$$\gamma_d^R(t) = \frac{\gamma_d}{G_R} |G_0^*| \sin(\omega t + \delta_0) \quad (6-5)$$

As previously explained, the dissipated pseudostrain energy density  $DPSED_N$  in the  $N$ th load cycle is defined as the energy corresponding to the enclosed area in the loop. The  $DPSED_N$  at a given radial position of the cylindrical bitumen sample in the damaged condition can be calculated as

$$DPSED_N(r) = \int_{(N-1)\frac{2\pi}{\omega}}^{N\frac{2\pi}{\omega}} \tau_N(t) d\gamma_d^R(t) \quad (6-6)$$

where  $N$  is the number of loading cycles and  $\frac{2\pi}{\omega}$  is the loading period. Based on the controlled shear strain  $\gamma_d(t)$  shown in **Equation (6-3)**, the measured shear stress in the damaged condition is expressed as

$$\tau_N(t) = \tau_N \sin(\omega t + \delta_N) \quad (6-7)$$

where  $\tau_N$  is the shear stress amplitude. According to the linear viscoelastic stress-strain law, the stress amplitude at a given radial position in a cylindrical bitumen sample can be written as

$$\tau_N(r) = |G_N^*| \gamma_d(r) \text{ with } 0 \leq r \leq r_0 \quad (6-8)$$

Substituting **Equations (6-5)**, **(6-7)** and **(6-4)** into **Equation (6-6)** gives

$$DPSED_N(r) = \pi \frac{|G_0^*|}{G_R} |G_N^*| \left( \frac{r\theta_0}{h} \right)^2 \sin(\delta_N - \delta_0) \quad (6-9)$$

Thus, the  $DPSED_N$  at a given radial position of the cylindrical bitumen sample under the damaged condition can be determined by **Equation (6-9)**.

To determine the energy consumed in one load cycle due to the crack growth in the bitumen, the dissipated pseudostrain energy  $DPSE_N$  in the  $N$ th load cycle is calculated by

integrating the  $DPSED_N$  over the volume in which the material dissipated the energy for cracking growth.

$$DPSE_N = \iiint_{V_{\Delta c}} DPSED_N(r) dV_{\Delta c} \approx DPSED_N(r) \cdot V_{\Delta c} \quad (6-10)$$

where  $V_{\Delta c}$  is the volume where the material has dissipated energy for the crack increment ( $\Delta c$ ) occurring in the  $N$ th load cycle and can be expressed as

$$V_{\Delta c} = \pi(r_E + \Delta c)^2 h - \pi(r_E)^2 h = \pi h(\Delta c^2 + 2r_E \Delta c) \quad (6-11)$$

where  $\Delta c$  is the crack increment in  $N$ th load cycle.

Based on **Equations (6-9)** and **(6-11)**, **Equation (6-10)** can be further written as

$$DPSE_N = \pi^2 \frac{|G_0^*|}{G_R} |G_N^*| \frac{(r_E^{N-1} \theta_0)^2}{h} \cdot (\Delta c^2 + 2r_E \Delta c) \cdot \sin(\delta_N - \delta_0) \quad (6-12)$$

## 6.4 Modelling Crack Propagation in Bitumen Using Pseudo J-integral Paris' Law

The pseudo J-integral Paris' law shown in **Equation (6-2)** is applied in this study to model the crack propagation in bitumen under a rotational shear fatigue load. It must be noted that the Paris' law is applicable only for the steady crack propagation in a fatigue test. Thus the pseudo J-integral Paris' law will be used to model the steady crack growth in the propagation stage in this study.

To compute Paris' law coefficients  $A$  and  $n$  in **Equation (6-2)**, the crack length  $c$  and the incremental pseudo J-integral  $\Delta J_R$  should be firstly determined. In this study, the crack length  $c$  is obtained by the DSR-C model shown in **Equation (4-23)**. It is noted that the pseudo J-integral equals the energy release rate resulting from cracking damage. This means the pseudo J-integral represents the rate of the dissipated energy that is solely consumed for crack growth, rather than for other physics such as viscoelastic relaxation or heat loss. The incremental pseudo J-integral  $\Delta J_R$  is defined as the dissipated pseudostrain energy (DPSE) to create a unit area of crack in the viscoelastic materials, as expressed in **Equation (6-13)**.

$$\Delta J_R = \frac{\partial DPSE}{\partial CSA} = \frac{\partial DPSE / \partial N}{\partial CSA / \partial N} = \frac{DPSE_N}{CSA_N} \quad (6-13)$$

where  $DPSE$  is the total dissipated pseudostrain energy which is accumulated from the first load cycle;  $CSA$  is the crack surface areas including the upper and lower crack surfaces that is

accumulated from the first load cycle; and  $DPSE_N$  and  $CSA_N$  are the dissipated pseudostrain energy (defined by **Equation (6-12)**) and the crack surface area, which are the incremental values in the  $N$ th load cycle, respectively. The  $CSA_N$  is calculated by

$$CSA_N = 2 \left[ \pi (r_E + \Delta c)^2 - \pi (r_E)^2 \right] = 2\pi (\Delta c^2 + 2r_E \Delta c) \quad (6-14)$$

Substituting **Equations (6-12)** and **(6-14)** into **Equation (6-13)**, the energy release rate per unit of crack surface area can be determined by the following **Equation (6-15)**.

$$\Delta J_R = \frac{\pi}{2} \frac{|G_0^*|}{G_R} |G_N^*| \frac{(r_E^{N-1} \theta)^2}{h} \sin(\delta_N - \delta_0) \quad (6-15)$$

where the shear reference modulus  $G_R$  is assigned to the shear modulus  $|G_0^*|$  of bitumen in the undamaged condition according to a previous study by Zhang et al. (2011).

Once the crack growth rate ( $dc/dN$ ) and the energy release rate ( $\Delta J_R$ ) were obtained, the crack evolution in the bitumen under the rotational shear fatigue load can be modelled by the Paris' law using the **Equation (6-2)**. The model parameters  $A$  and  $n$  can also be determined by regressing the data of crack growth rate ( $dc/dN$ ) against the energy release rate ( $\Delta J_R$ ).

## 6.5 Materials and Laboratory Tests

Two kinds of bituminous binders were employed in this study, including the unmodified bitumen 40/60 and the polymer-modified bitumen X-70. They were tested before and after Thin-Film Oven Test (TFOT) laboratory ageing. Bitumen samples were prepared using a silicone mould by following the procedure described in **Section 4.6**. A Kinexus DSR from Malvern Panalytical with an 8 mm diameter parallel plate geometry (2 mm gap) was used to conduct the laboratory tests. The frequency sweep (FS) test and the time sweep (TS) test were performed to determine the model parameters and evaluate the crack propagation of the bitumen. At each testing condition, two replicates were tested and their average value was used for data analysis. One more replicate was required if the deviation between the two measured results was greater than 10%.

In order to obtain the shear modulus ( $|G_0^*|$ ) and the phase angle ( $\delta_0$ ) of the binders in the undamaged condition, FS tests were conducted at temperatures of 15, 20 and 25 °C and frequencies between 1 and 25 Hz under 0.5% shear strain level. TS fatigue damage tests were performed to obtain the shear modulus ( $|G_N^*|$ ) and the phase angle ( $\delta_N$ ) of the binders with the

number of load cycles in the damaged condition. The strain levels of 3%, 5% and 7%, corresponding to the rotation amplitudes of 0.015, 0.025 and 0.035 rad, respectively, were selected for the TS fatigue damage tests. Based on the results from Linear Amplitude Sweep (LAS) tests, it was found that the applied strain levels are sufficiently high to generate fatigue cracking damage for all tested samples, as discussed in **Section 4.6.3**. The three strain levels have been used in the TS tests to study the fatigue damage response of bituminous binders in the literature (Wang et al., 2015a, Wang et al., 2016). To investigate the effects of temperature and loading frequency on crack evolution, TS tests were performed at different experimental conditions, as shown in **Table 1**.

In the FS and TS tests for unaged X-70 bitumen, aged X-70 bitumen and unaged 40/60 bitumen, the three test temperatures (15, 20 and 25 °C) were selected within the intermediate temperature range at which a fatigue cracking commonly happens. For aged 40/60 bitumen, the test temperatures of 20, 25 and 30 °C were used due to its high stiffness (shear modulus). The three test frequencies (5, 10 and 15 Hz) were employed to produce fatigue cracking within the reasonable load cycles.

**Table 6-1 Laboratory test plan.**

Tests	Bitumen	Temperature (°C)	Frequency (Hz)	Strain levels	Load cycles
Frequency Sweep	Unaged X-70 Unaged 40/60 Aged X-70	15, 20, 25	1-25	0.5%	NA
	Aged 40/60	20, 25, 30			
Time Sweep	Unaged X-70 Unaged 40/60 Aged X-70	15, 20, 25	5, 10, 20	3%, 5%, 7%	24000
	Aged 40/60	20, 25, 30			

## 6.6 Results and Discussion

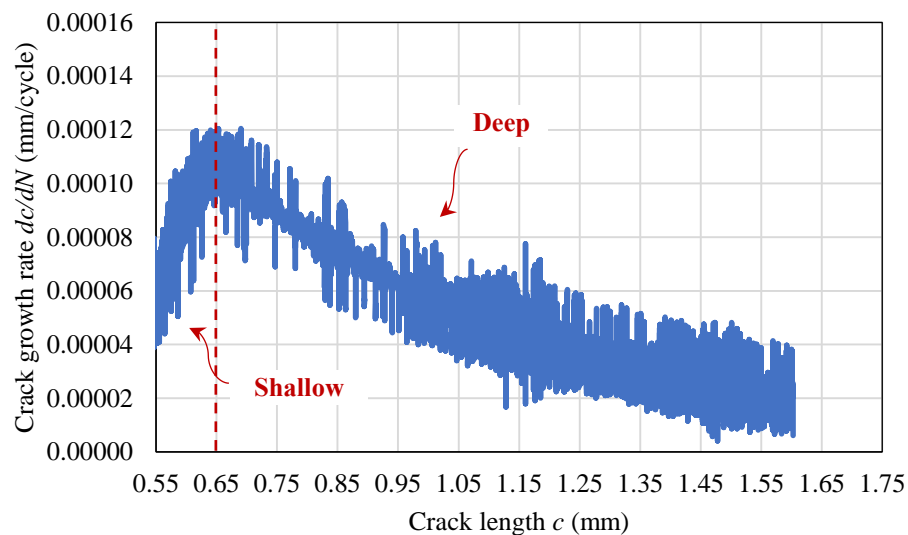
### 6.6.1 Description of fatigue crack propagation in bitumen

According to the analysis of fatigue cracking process shown in **Section 5.4**, the crack growth in bitumen under a rotational shear fatigue load demonstrates different cracking stages. **Figure 5-3** shows the crack growth rate ( $dc/dN$ ) with the crack length. It can be seen that the crack growth is divided into edge flow damage and crack propagation (“factory-roof” cracking).

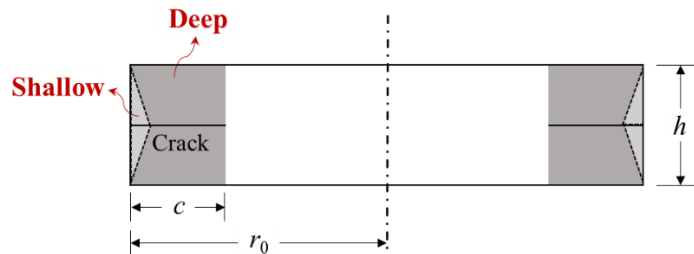
During the crack propagation, it is found from **Figure 6-1(a)** that the crack growth rate increases as crack length increases, followed by a decrease in crack growth rate with increasing crack length. The crack propagation trend was referred to as ‘shallow’ and ‘deep’ crack growth

(Gent and Yeoh, 2003). The shallow crack growth is driven by the strain energy from the material in the immediate vicinity of the crack. As the crack propagates inward, the more volume of material near the sample edge starts to supply the energy, resulting in an increase in the crack growth rate. However, this energy source would only last a short time and then be limited by the physical top and bottom boundaries of the sample (e.g., the top and bottom plates in the DSR test), as shown in **Figure 6-1(b)**. At this point, the crack propagation becomes the deep crack growth, which is driven by the strain energy from the material in the interior of the sample. According to the strain distribution in the sample, the amount of energy available decreases and consequently crack growth rate decreases with the increasing crack length. The deep crack growth is observed as a steady cracking stage during the crack propagation.

Therefore, the crack propagation model shown in **Equation (6-2)** based on pseudo J-integral Paris' law is used during the deep crack growth in this study as the Paris' law is only applicable to stable crack growth (Anderson, 2005).



(a) Crack growth rate vs. crack length during crack propagation.



(b) A schematic side view of a cylindrical sample during crack propagation.  
**Figure 6-1** Crack propagation including 'shallow' crack growth and 'deep' crack growth.

### 6.6.2 Paris' law coefficients $A$ and $n$

Crack growth rate  $dc/dN$  as a function of energy release rate  $\Delta J_R$  during the deep (steady) crack propagation is plotted in **Figure 6-2** for the four binders tested at 20 °C and 10 Hz under 5% strain level. **Figure 6-2** demonstrates that crack growth in the bitumen under the rotational shear fatigue load generally follows a power law relationship between crack growth rate and energy release rate. Based on this result, the developed crack propagation model is used to fit the  $dc/dN$ - $\Delta J_R$  curve from the time sweep (TS) testing to determine the Paris' law coefficients  $A$  and  $n$ , which are also shown in **Figure 6-2** for the four tested binders. It can be seen that high coefficients of determination were obtained for all four binder ( $R^2 > 0.98$ ), proving that the crack propagation model based on pseudo J-integral Paris' law is able to accurately characterise the crack propagation in different bituminous binders under a rotational shear fatigue load.

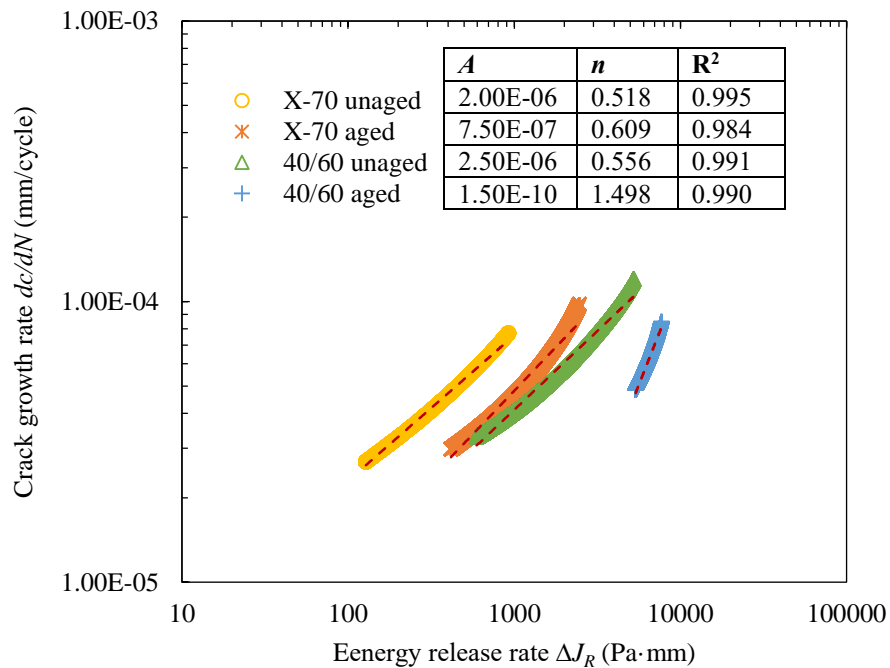


**Figure 6-2 Relationship between crack growth rate ( $dc/dN$ ) and energy release rate ( $\Delta J_R$ ) during deep (steady) crack growth at 20 °C and 10 Hz under 5% strain level.**

**Figure 6-3** shows the Paris' law coefficients  $A$  and  $n$  for the four different binders determined from the time sweep (TS) tests at the different temperatures and ageing conditions. It is found from **Figures 6-3** that, when the bitumen becomes stiffer due to laboratory ageing, the Paris' law coefficient  $A$  decreases and the Paris' law exponent  $n$  increases. Compared to the

polymer modified X-70, the unmodified 40/60 bitumen introduces bigger changes in the Paris' law coefficients. For instance, when the binders became aged, the  $n$  value increases by 169.17% for the unmodified 40/60 bitumen but increases by only 17.56% for the polymer modified X-70 at all testing temperatures. This indicates that the ageing has a more significant impact on the crack propagation of the unmodified bitumen than that of the polymer modified bitumen.

More importantly, **Figure 6-3** demonstrates that the temperature has a significant effect on the Paris' law coefficients  $A$  and  $n$  for the four types of bituminous binders. The Paris' law coefficient  $A$  increases and the Paris' law exponent  $n$  decreases with an increasing temperature due to the viscoelastic nature of the bitumen. This phenomenon has also been found in asphalt mixtures, as reported in the literature (Jacobs, 1995, Zhou et al., 2007).

In conclusion, a stiffer bituminous binder due to laboratory ageing or decreasing temperature tends to have a smaller Paris' law coefficient  $A$  and a larger Paris' law exponent  $n$ . A higher  $n$  value leads to a quicker crack propagation. This means the crack grows faster for the aged bitumen or at lower temperatures.

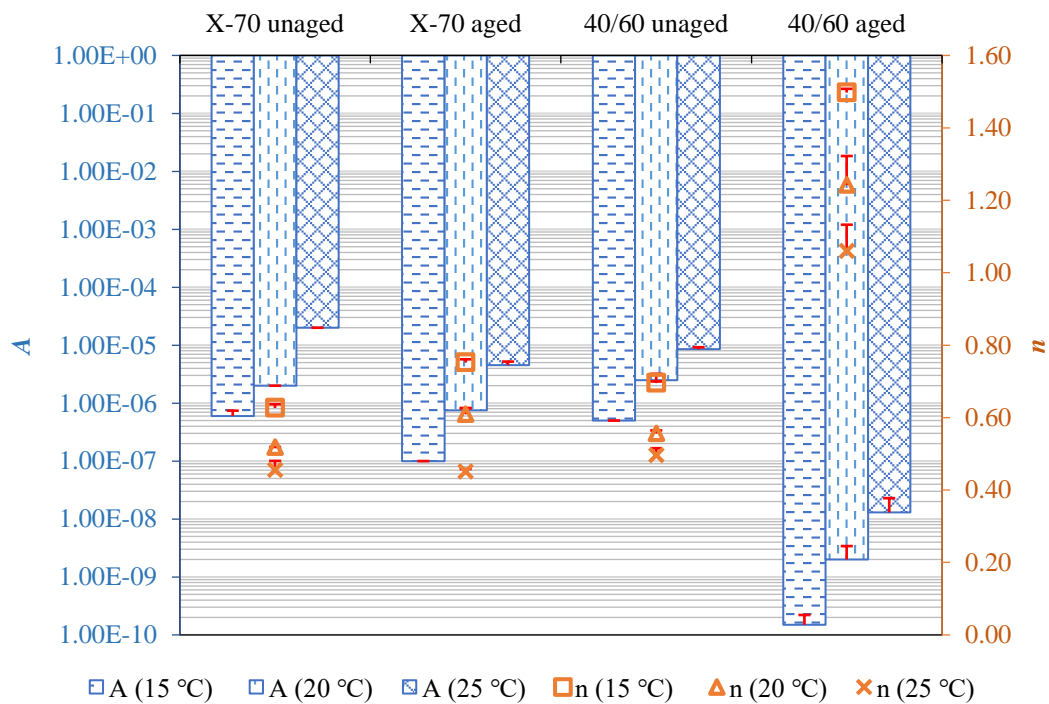
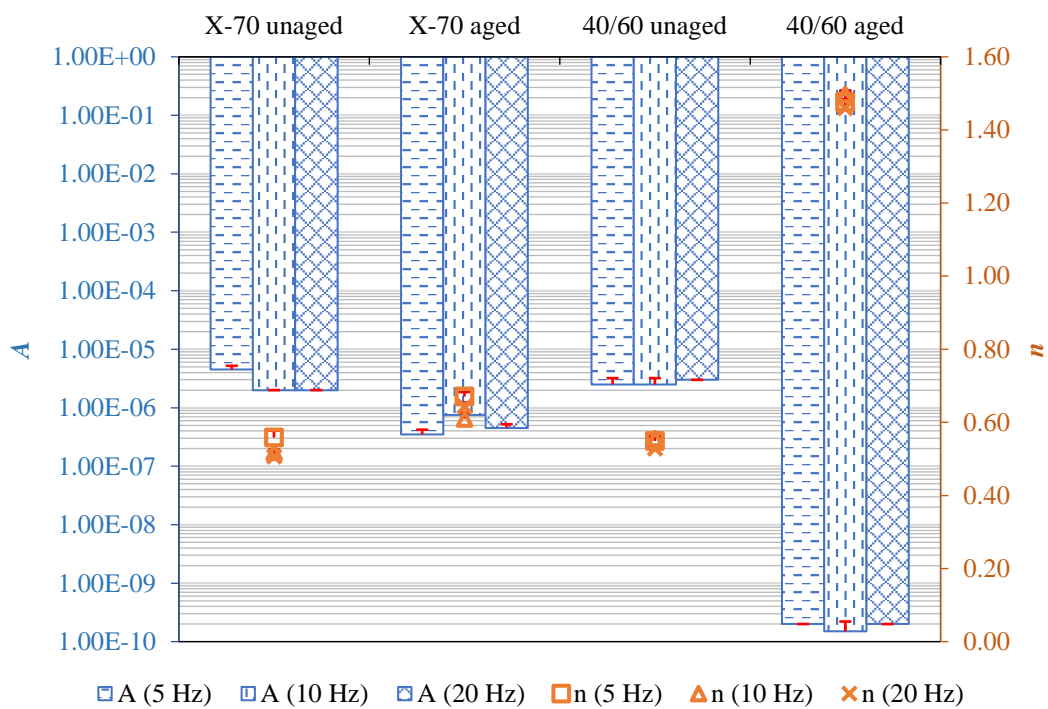


**Figure 6-3 Paris' law coefficients at different temperatures and ageing conditions (@ 10 Hz and 5% strain level).**

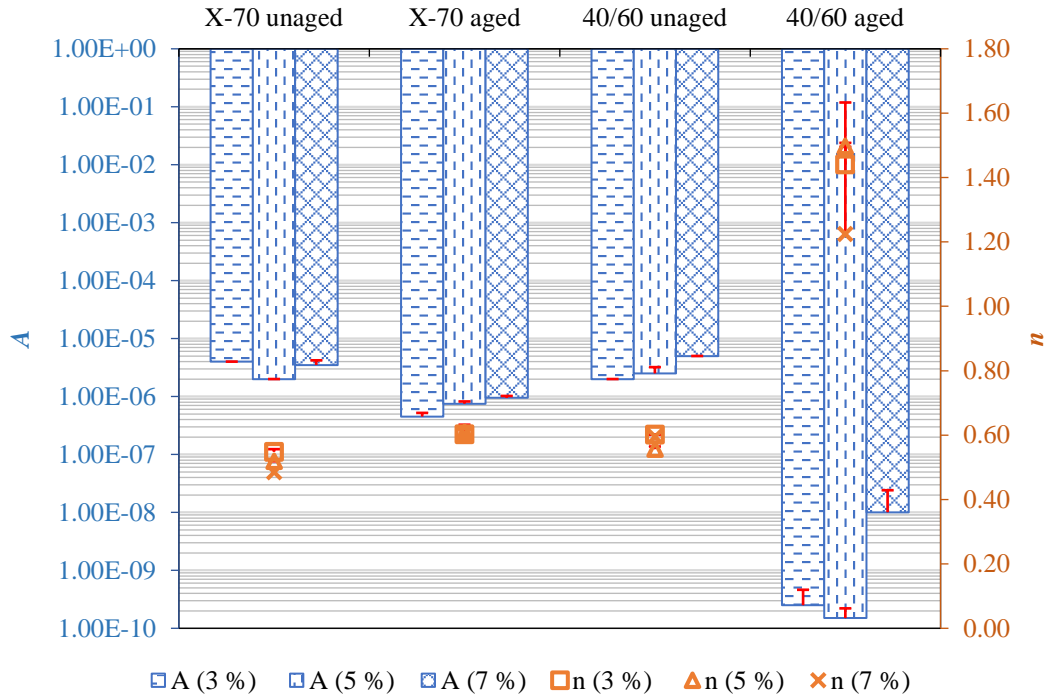
**Figure 6-4** presents the Paris' law coefficients  $A$  and  $n$  of all binders at different loading frequencies and strain levels. **Figure 6-4** indicates that the Paris' law coefficients  $A$  and  $n$  of a

specific bituminous binder do not vary significantly with either loading frequencies or loading amplitudes (strain levels). Therefore, it can be concluded that the Paris' law coefficients  $A$  and  $n$  are fundamental material parameters and independent of loading frequency or loading amplitude. The independence of the Paris' law coefficients of loading rate or loading mode has been verified for asphalt mixtures (Zhang et al., 2018). Thus the Paris' law coefficients  $A$  and  $n$  can be determined at one loading frequency and amplitude, then be implemented to predict the crack growth of the bitumen at different loading frequencies or amplitudes.

It should be noted that the variability of the results was also analysed in this study using two replicates at each testing condition. The standard deviation for all the tested samples under different testing conditions was shown in **Figures 6-2, 6-3 and 6-4** by red error bar. It can be seen that the standard deviation for Paris' law coefficients  $A$  and  $n$  is very low, which indicates that the variability of the results is much less significant.



**(a) Paris' law coefficients at different loading frequencies (@ 20 °C and 5% strain level).**



(b) Paris' law coefficients at different strain levels (@ 20 °C and 10 Hz).  
**Figure 6-4 Paris' law coefficients at different loading frequencies and strain levels for different binders.**

## 6.7 Conclusions

In this chapter, fatigue crack propagation in bitumen is modelled at the macroscale. The crack propagation in the bitumen under a rotational shear fatigue load was investigated by a time sweep (TS) fatigue test using the dynamic shear rheometer (DSR). The crack evolution is modelled by a pseudo J-integral based Paris' law. TS tests were conducted for the virgin bitumen 40/60 and the polymer-modified bitumen X-70 before and after laboratory ageing. These fatigue tests were performed at different temperatures, loading frequencies and loading amplitudes. Conclusions were drawn from the research as below:

- (1) The crack propagation model based on the pseudo J-integral Paris' law is able to accurately characterise the crack evolution in bitumen under a rotational shear fatigue load.
- (2) A stiffer bitumen due to laboratory ageing or decreasing temperature tends to have a smaller Paris' law coefficient  $A$  and a larger Paris' law exponent  $n$ . This proves that crack grows faster for the aged bitumen or at lower temperatures.

- (3) Ageing has a more significant impact on the crack propagation of the unmodified bitumen than that of the polymer modified bitumen.
- (4) The Paris' law coefficients  $A$  and  $n$  are demonstrated to be independent of loading frequency or loading amplitude, which indicate that they are fundamental material properties that are functions of temperatures and the material itself.

Based on the above conclusions, the Paris' law coefficients  $A$  and  $n$  can be determined at one loading frequency and amplitude, then be implemented to predict the crack growth of the bitumen at different loading frequencies or amplitudes.

# Chapter 7 Summaries, Conclusions and Recommendations

## 7.1 Summaries

Bonding performance of bituminous materials fundamentally determines the resistance of asphalt to fatigue cracking which is one of the major distresses in asphalt pavements. The fatigue performance of asphalt is closely related to fatigue resistance of bitumen. The fatigue mechanisms of bitumen have not been well understood, particularly from the fundamental perspective of material bonding behaviour at multiple scales. To reveal the debonding mechanism of fatigue damage in bitumen, a hierarchical multiscale modelling framework was developed in this study to understand and model the bonding performance of bitumen from nanoscale to macroscale so as to accurately and reliably predict the fatigue crack initiation and propagation in bitumen.

At the nanoscale, the bonding performance of bitumen with the effects of aggregate mineralogy and oxidative ageing was modelled using the molecular dynamics (MD) simulations to understand the fundamental mechanisms in bitumen bonding. The MD simulations were validated by the contact angle measurements. At the microscale, the cohesive debonding performance of bitumen under a rotational shear fatigue load was first quantified by the DSR-C model to predict fatigue crack length. Then, based on the understanding of bonding performance at the nanoscale, an energy-based fatigue crack initiation criterion for bitumen was proposed using a viscoelastic Griffith's theory. At the macroscale, the cohesive debonding behaviour in bitumen was modelled for fatigue crack propagation by a pseudo J-integral based Paris' law. The developed models were validated by DSR tests conducted at different environmental and loading conditions.

In this multiscale modelling framework, the critical link between the nanoscale modelling and the microscale and macroscale modelling lies in that the fundamental material parameters predicted from nanoscale are scale-independent thus can be directly used as the inputs to the mechanical models for bitumen's fatigue cracking prediction at the microscale and the macroscale. The fundamental investigation of bonding performance of bitumen from multiscale modelling can provide critical information to better explore and predict the material behaviour and pavement performance of mastic and asphalt at higher levels.

## 7.2 Conclusions

Specific conclusions drawn from this study are summarised below.

- **Nanoscale modelling**

- (1) The cohesive bond energy predicted based on MD simulations at the nanoscale can be used as a fundamental and scale-independent input for the mechanics modelling of bitumen fatigue cracking at the microscale.
- (2) The adhesive bonding performance between bitumen and minerals is attributed to non-bond interaction energy, where the major contribution is from van der Waals interaction for the acidic minerals like quartz while from the electrostatic interaction for the alkali minerals such as calcite, albite and microcline.
- (3) For both dry and wet conditions, the calcite-bitumen bonding performance is stronger than the quartz-bitumen bonding performance, and the adhesion of the four minerals with bitumen is ranked as: microcline > albite > calcite > quartz. The moisture can reduce the adhesion between bitumen and minerals by 82%, 84%, 18% and 1% for the quartz, calcite, albite and microcline, respectively.
- (4) The oxidised functional groups (i.e., ketone and sulfoxide) in bitumen due to oxidative ageing strengthens the intermolecular bonding performance of the bitumen including van der Waals and electrostatic interactions, which results in the aggregation of bitumen molecules and physical hardening of the aged bitumen, eventually leading to block cracking in the field pavements.
- (5) The adhesive bonding performance of bitumen-acidic minerals (e.g., quartz) at dry condition is dominated by van der Waals interaction which decreases when bitumen becomes aged. This is due to the increased bitumen-quartz distance caused by the aggregated bitumen molecules. In comparison, the interfacial adhesion of bitumen-strong alkali minerals (e.g., albite and microcline) is dominated by electrostatic energy which increases during ageing. This results from the higher polarity introduced by the oxidised products including ketone and sulfoxide in an aged bitumen.
- (6) The adhesive bonding performance of bitumen-weak alkali mineral (calcite) at dry condition is attributed primarily to electrostatic energy and secondarily to van der Waals energy. The electrostatic energy between aged bitumen and the weak alkali mineral decreases due to the increased bitumen-mineral distance when the bitumen is lightly-oxidised and increases due to the higher bitumen polarity when the bitumen is heavily-oxidised.

- (7) For the adhesive bonding performance in wet condition, water is the dominating factor that affects (weakens) the interfacial adhesion between the bitumen and the acidic minerals such as quartz. While the oxidative ageing of bitumen is the major factor that affects (strengthens) the interfacial adhesion between the bitumen and the strongly alkaline minerals (i.e., albite and microcline). For the weak alkali minerals such as calcite, both water and bitumen ageing can significantly affect the interfacial adhesion.

- **Microscale modelling**

- (1) The DSR-based crack length (DSR-C) model based on damage mechanics is capable of accurately and reliably predicting the crack length in bitumen under a rotational shear fatigue load at different loading and environmental conditions and for different bitumen materials.
- (2) The DSR-C model can be applied to investigate the effects of ageing, temperature, loading frequency and strain level (loading amplitude) on the fatigue performance of bitumen. Bitumen will be subjected to a more severe fatigue damage with the increasing crack length by 9.32%, 7.34%, 7.04% or 36.53% in this study when the bitumen became aged, the temperature went lower, the loading frequency increased, or the strain level increased.
- (3) The crack length at the stable crack growth stage predicted by DSR-C model has the potential to quantify the fatigue resistance of different bitumen materials including the polymer modified bitumen.
- (4) Bitumen fatigue cracking under a rotational shear fatigue load can be divided into two stages: the edge flow damage and the ‘factory-roof’ cracking.
- (5) The edge flow damage can be regarded as a process including the molecular rearrangements, microcrack nucleation and circumferential crack formation.
- (6) The local energy redistribution due to the circumferential ‘factory-roof’ crack is quantified by the pseudostrain energy. A crack initiation criterion is developed for bitumen under a rotational shear fatigue load based on viscoelastic Griffith’s criterion.
- (7) The energy-based crack initiation criterion along with the DSR fatigue tests can act as a substitute for the surface energy tests.

- **Macroscale modelling**

- (1) The crack propagation model based on the pseudo J-integral Paris’ law is able to accurately characterise the crack evolution in bitumen under a rotational shear fatigue load.
- (2) A stiffer bitumen due to laboratory ageing or decreasing temperature tends to have a

smaller Paris' law coefficient  $A$  and a larger Paris' law exponent  $n$ . This proves that crack grows faster for the aged bitumen or at lower temperatures.

- (3) Ageing has a more significant impact on the crack propagation of the unmodified bitumen than that of the polymer modified bitumen.
- (4) The Paris' law coefficients  $A$  and  $n$  are demonstrated to be independent of loading frequency or loading amplitude, which indicate that they are fundamental material properties and are only functions of temperature and the material itself.

### 7.3 Recommendations

This study provides a significant contribution to the fundamental understanding and characterisation of bonding performance of bitumen by using a bottom-up multiscale modelling approach. However, there are some areas that merit further investigation to continue the research effectively. Recommendations for future studies are suggested as follows:

- (1) Based on the twelve-component model with the saturate, aromatic, resin and asphaltene (SARA) four fractions, a widely used bitumen molecular model proposed by Li and Greenfield (2014a) is employed in this study to investigate the bonding performance of the bitumen at the nanoscale. This molecular model is capable of simulating the molecular behaviour of the bitumen bonding. However, the simulation results from this general model cannot be directly compared to the test results of a specific bitumen sample. More specific molecular models are needed to simulate the tested bitumen such as the 40/60 bitumen and the X-70 bitumen used for this study. In future study, the molecular models should be built using actual measurements of SARA mass fractions to predict the bonding performance of the tested bituminous binders.
- (2) In this study, an unmodified bitumen 40/60 and a polymer-modified bitumen X-70 were selected and their unaged and aged samples were prepared. Four kinds of bitumen samples in total were tested at different testing temperatures, frequencies and amplitudes to validate the developed models. Future study is needed for the further validation of the developed models in more different types of bituminous binders and the practical application of the models to quantify and differentiate the fatigue performances of various bituminous binders.
- (3) Fatigue cracking in asphalt pavements typically occurs either within bitumen or at bitumen-aggregate interface. The cohesive debonding performance of bitumen under a rotational shear fatigue load is investigated in this study to better evaluate the cohesive

fatigue failure of the bitumen. In the future study, the mechanistic modelling of adhesive debonding performance of the bitumen-aggregate interface under the rotational shear fatigue load is needed to evaluate the adhesive fatigue failure of the bitumen with aggregate. To model the adhesive debonding for fatigue cracking at the interface, the prediction of the adhesive bonding performance of the bitumen with aggregate is also needed at the nanoscale. The recommended study will allow for multiscale modelling of adhesive bonding performance of bituminous materials.

- (4) Asphalt concrete is a typical multi-phase viscoelastic composite, which exhibits a hierarchical structure composed of molecule (Level 0), bitumen (Level I), mastic (Level II) and asphalt (Level III), as illustrated in **Chapter 1**. This study is mainly focused on the bonding modelling of molecules at the Level 0 and the bitumen at the Level I. Following this fundamental investigation, future study involving multiscale constitutive modelling of mastic and asphalt at the higher levels (Levels II and III) is needed to better improve the material selection, mixture design and pavement performance prediction.

## List of References

- AASHTO 2012. Standard method of test for determining the rheological properties of asphalt binder using a dynamic shear rheometer (DSR). American Association of State and Highway Transportation Officials.
- ABO-QUDAIS, S. & AL-SHWEILY, H. 2007. Effect of aggregate properties on asphalt mixtures stripping and creep behavior. *Construction and Building Materials*, 21, 1886-1898.
- ABOUTORABI, H., EBBOTT, T., GENT, A. & YEOH, O. 1998. Crack growth in twisted rubber disks. Part I: Fracture energy calculations. *Rubber Chemistry and Technology*, 71, 76-83.
- AMIN, J. S., NIKOOEE, E., GHATEE, M., AYATOLLAHI, S., ALAMDARI, A. & SEDGHAMIZ, T. 2011. Investigating the effect of different asphaltene structures on surface topography and wettability alteration. *Applied Surface Science*, 257, 8341-8349.
- ANDERSEN, S. I. & BIRDI, K. S. 1991. Aggregation of asphaltenes as determined by calorimetry. *Journal of Colloid and Interface Science*, 142, 497-502.
- ANDERSON, D. A. & KENNEDY, T. W. 1993. Development of SHRP binder specification (with discussion). *Journal of the Association of Asphalt Paving Technologists*, 62.
- ANDERSON, D. A., LE HIR, Y. M., MARASTEANU, M. O., PLANCHE, J.-P., MARTIN, D. & GAUTHIER, G. 2001. Evaluation of fatigue criteria for asphalt binders. *Transportation Research Record*, 1766, 48-56.
- ANDERSON, T. L. 2005. *Fracture mechanics: fundamentals and applications*, CRC press.
- APEAGYEI, A. K., GRENFELL, J. R. & AIREY, G. D. 2014. Moisture-induced strength degradation of aggregate–asphalt mastic bonds. *Road Materials and Pavement Design*, 15, 239-262.
- ARTOK, L., SU, Y., HIROSE, Y., HOSOKAWA, M., MURATA, S. & NOMURA, M. 1999. Structure and reactivity of petroleum-derived asphaltene. *Energy & Fuels*, 13, 287-296.
- BAHIA, H. U., HANSON, D., ZENG, M., ZHAI, H., KHATRI, M. & ANDERSON, R. 2001a. Characterization of modified asphalt binders in superpave mix design. Washington, DC: National Cooperative Highway Research Program.
- BAHIA, H. U., ZHAI, H., ZENG, M., HU, Y. & TURNER, P. 2001b. Development of binder specification parameters based on characterization of damage behavior (with discussion). *Journal of the Association of Asphalt Paving Technologists*, 70.
- BASCOM, W., COTTINGTON, R., JONES, R. & PEYSER, P. 1975. The fracture of epoxy - and elastomer - modified epoxy polymers in bulk and as adhesives. *Journal of Applied Polymer Science*, 19, 2545-2562.
- BHASIN, A., BOMMAVARAM, R., GREENFIELD, M. L. & LITTLE, D. N. 2010. Use of molecular dynamics to investigate self-healing mechanisms in asphalt binders. *Journal of Materials in Civil Engineering*, 23, 485-492.
- BHASIN, A., LITTLE, D. N., VASCONCELOS, K. L. & MASAD, E. 2007. Surface free energy to identify moisture sensitivity of materials for asphalt mixes. *Transportation Research Record*, 2001, 37-45.
- BHASIN, A., PALVADI, S. & LITTLE, D. N. 2011. Influence of aging and temperature on intrinsic healing of asphalt binders. *Transportation Research Record*, 2207, 70-78.
- BONNETTI, K. S., NAM, K. & BAHIA, H. U. 2002. Measuring and defining fatigue behavior of asphalt binders. *Transportation Research Record*, 1810, 33-43.
- BROWN, H. & WARD, I. 1973. Craze shape and fracture in poly (methyl methacrylate). *Polymer*, 14, 469-475.

- BROWN, L. 1977. Dislocation substructures and the initiation of cracks by fatigue. *Metal Science*, 11, 315-320.
- CAI, C., ZHANG, C., CAI, L., WU, G., JIANG, L., XU, Z., LI, K., MA, A. & CHEN, L. 2009. Origins of Palaeozoic oils in the Tarim Basin: evidence from sulfur isotopes and biomarkers. *Chemical Geology*, 268, 197-210.
- CHAN, K. S. 2003. A microstructure-based fatigue-crack-initiation model. *Metallurgical and Materials Transactions A*, 34, 43-58.
- CHEN, Z., PEI, J., LI, R. & XIAO, F. 2018. Performance characteristics of asphalt materials based on molecular dynamics simulation—A review. *Construction and Building Materials*, 189, 695-710.
- CHEN, Z., XIE, J., XIAO, Y., CHEN, J. & WU, S. 2014. Characteristics of bonding behavior between basic oxygen furnace slag and asphalt binder. *Construction and Building Materials*, 64, 60-66.
- CHENG, D., LITTLE, D. N., LYTTON, R. L. & HOLSTE, J. C. 2002. Surface energy measurement of asphalt and its application to predicting fatigue and healing in asphalt mixtures. *Transportation Research Record*, 1810, 44-53.
- CHRISTENSEN, R. 1979. A rate-dependent criterion for crack growth. *International Journal of Fracture*, 15, 3-21.
- COLLOP, A. C., CHOI, Y. & AIREY, G. 2007. Effects of pressure and aging in SATS test. *Journal of Transportation Engineering*, 133, 618-624.
- CUCALON, L. G., KASSEM, E., LITTLE, D. N. & MASAD, E. 2017. Fundamental evaluation of moisture damage in warm-mix asphalts. *Road Materials and Pavement Design*, 18, 258-283.
- CUI, S., BLACKMAN, B. R., KINLOCH, A. J. & TAYLOR, A. C. 2014. Durability of asphalt mixtures: Effect of aggregate type and adhesion promoters. *International Journal of Adhesion and Adhesives*, 54, 100-111.
- DAS, P. K., BALIEU, R., KRINGOS, N. & BIRGISSON, B. 2015. On the oxidative ageing mechanism and its effect on asphalt mixtures morphology. *Materials and Structures*, 48, 3113-3127.
- DENG, M., TAN, V. & TAY, T. 2004. Atomistic modeling: interfacial diffusion and adhesion of polycarbonate and silanes. *Polymer*, 45, 6399-6407.
- DING, Y., HUANG, B., SHU, X., ZHANG, Y. & WOODS, M. E. 2016. Use of molecular dynamics to investigate diffusion between virgin and aged asphalt binders. *Fuel*, 174, 267-273.
- DONG, Z., LIU, Z., WANG, P. & GONG, X. 2017. Nanostructure characterization of asphalt-aggregate interface through molecular dynamics simulation and atomic force microscopy. *Fuel*, 189, 155-163.
- DOREMUS, R. 1976. Cracks and energy—Criteria for brittle fracture. *Journal of Applied Physics*, 47, 1833-1836.
- GAO, Y., DONG, M., LI, L., WANG, L. & SUN, Z. 2015. Interface effects on the creep characteristics of asphalt concrete. *Construction and Building Materials*, 96, 591-598.
- GAO, Y., LI, L. & ZHANG, Y. 2020. Modeling Crack Propagation in Bituminous Binders under a Rotational Shear Fatigue Load using Pseudo J-Integral Paris' Law. *Transportation Research Record*, DOI: 10.1177/0361198119899151.
- GAO, Y., ZHANG, Y., GU, F., XU, T. & WANG, H. 2018. Impact of minerals and water on bitumen-mineral adhesion and debonding behaviours using molecular dynamics simulations. *Construction and Building Materials*, 171, 214-222.
- GAO, Y., ZHANG, Y., YANG, Y., ZHANG, J. & GU, F. 2019. Molecular dynamics investigation of interfacial adhesion between oxidised bitumen and mineral surfaces. *Applied Surface Science*, 479, 449-462.
- GENT, A. & YEOH, O. 2003. Crack growth in twisted rubber disks. Part 3. Effects of crack depth and location. *Rubber Chemistry and Technology*, 76, 1276-1289.

- GHUZLAN, K. A. & CARPENTER, S. H. 2000. Energy-derived, damage-based failure criterion for fatigue testing. *Transportation Research Record*, 1723, 141-149.
- GIBSON, N. H., SCHWARTZ, C. W., SCHAPERLY, R. A. & WITCZAK, M. W. 2003. Viscoelastic, viscoplastic, and damage modeling of asphalt concrete in unconfined compression. *Transportation Research Record*, 1860, 3-15.
- GOOD, R. J. & GIRIFALCO, L. 1960. A theory for estimation of surface and interfacial energies. III. Estimation of surface energies of solids from contact angle data. *The Journal of Physical Chemistry*, 64, 561-565.
- GREENFIELD, M. L. 2011. Molecular modelling and simulation of asphaltenes and bituminous materials. *International Journal of Pavement Engineering*, 12, 325-341.
- GRENFELL, J., AHMAD, N., LIU, Y., APEAGYEI, A., LARGE, D. & AIREY, G. 2014. Assessing asphalt mixture moisture susceptibility through intrinsic adhesion, bitumen stripping and mechanical damage. *Road Materials and Pavement Design*, 15, 131-152.
- GRIFFITH, A. A. 1921. VI. The phenomena of rupture and flow in solids. *Philosophical transactions of the royal society of london. Series A, containing papers of a mathematical or physical character*, 221, 163-198.
- GROENZIN, H. & MULLINS, O. C. 2000. Molecular size and structure of asphaltenes from various sources. *Energy & Fuels*, 14, 677-684.
- HINTZ, C. & BAHIA, H. 2013a. Simplification of linear amplitude sweep test and specification parameter. *Transportation Research Record*, 2370, 10-16.
- HINTZ, C. & BAHIA, H. 2013b. Understanding mechanisms leading to asphalt binder fatigue in the dynamic shear rheometer. *Road Materials and Pavement Design*, 14, 231-251.
- HINTZ, C., VELASQUEZ, R., BAHIA, H. & STIMILLI, A. 2011a. Normal stresses in dynamic shear rheometer testing for binder damage. *University of Wisconsin-Madison Modified Asphalt Research Center (MARC) white paper*.
- HINTZ, C., VELASQUEZ, R., JOHNSON, C. & BAHIA, H. 2011b. Modification and validation of linear amplitude sweep test for binder fatigue specification. *Transportation Research Record*, 2207, 99-106.
- HORGNIES, M., DARQUE-CERETTI, E., FEZAI, H. & FELDER, E. 2011. Influence of the interfacial composition on the adhesion between aggregates and bitumen: Investigations by EDX, XPS and peel tests. *International Journal of Adhesion and Adhesives*, 31, 238-247.
- HOU, Y., WANG, L., WANG, D., GUO, M., LIU, P. & YU, J. 2017a. Characterization of bitumen micro-mechanical behaviors using AFM, phase dynamics theory and MD simulation. *Materials*, 10, 208.
- HOU, Y., WANG, L., WANG, D., QU, X. & WU, J. 2017b. Using a molecular dynamics simulation to investigate asphalt nano-cracking under external loading conditions. *Applied Sciences*, 7, 770.
- HOUSTON, W., MIRZA, M., ZAPATA, C. & RAGHAVENDRA, S. 2007. Simulating the effects of hot mix asphalt aging for performance testing and pavement structural design. *NCHR Research Results Digest*, 324.
- HOWSON, J., MASAD, E., BHASIN, A., LITTLE, D. & LYTTON, R. 2011. Comprehensive analysis of surface free energy of asphalts and aggregates and the effects of changes in pH. *Construction and Building Materials*, 25, 2554-2564.
- HOWSON, J. E. 2011. *Relationship between surface free energy and total work of fracture of asphalt binder and asphalt binder-aggregate interfaces*. Texas A&M University, Texas.
- HUI, C., RUINA, A., CRETON, C. & KRAMER, E. 1992. Micromechanics of crack growth into a craze in a polymer glass. *Macromolecules*, 25, 3948-3955.
- JACOBS, M. M. J. 1995. Crack growth in asphaltic mixes.
- JAHANGIR, R., LITTLE, D. & BHASIN, A. 2015. Evolution of asphalt binder microstructure due to tensile loading determined using AFM and image analysis techniques. *International Journal of Pavement Engineering*, 16, 337-349.

- JENNINGS, P., PRIBANIC, J., DESANDO, M., RAUB, M., MOATS, R., SMITH, J., MENDES, T., MCGRANE, M., FANCONI, B. & VANDERHART, D. 1993. Binder characterization and evaluation by nuclear magnetic resonance spectroscopy. Strategic Highway Research Program, National Research Council, Washington, DC.
- JONES, D. R. 1993. *SHRP materials reference library: Asphalt cements: A concise data compilation*, Strategic Highway Research Program, National Research Council, Washington, DC.
- KAMBOUR, R. P. 1966. Mechanism of fracture in glassy polymers. III. Direct observation of the craze ahead of the propagating crack in poly (methyl methacrylate) and polystyrene. *Journal of Polymer Science Part A - 2: Polymer Physics*, 4, 349-358.
- KEENTOK, M. & XUE, S.-C. 1999. Edge fracture in cone-plate and parallel plate flows. *Rheologica Acta*, 38, 321-348.
- KIM, Y. R., LEE, H.-J. & LITTLE, D. N. 1997. Fatigue characterization of asphalt concrete using viscoelasticity and continuum damage theory (with discussion). *Journal of the Association of Asphalt Paving Technologists*, 66.
- KING, W. H. & CORBETT, L. W. 1969. Relative oxygen absorption and volatility properties of submicron films of asphalt using the quartz crystal microbalance. *Analytical Chemistry*, 41, 580-583.
- KNAUSS, W. 1969. Stable and unstable crack growth in viscoelastic media. *Transactions of the Society of Rheology*, 13, 291-313.
- KNORR JR, D. B., DAVISON, R. R. & GLOVER, C. J. 2002. Effect of various aging techniques on asphalt low-temperature properties. *Transportation Research Record*, 1810, 9-16.
- KOC, M. & BULUT, R. 2013. Assessment of a sessile drop device and a new testing approach measuring contact angles on aggregates and asphalt binders. *Journal of Materials in Civil Engineering*, 26, 391-398.
- KOOPMANS, M. P., DE LEEUW, J. W. & DAMSTÉ, J. S. S. 1997. Novel cyclised and aromatised diagenetic products of  $\beta$ -carotene in the Green River Shale. *Organic Geochemistry*, 26, 451-466.
- KOOPMANS, M. P., DE LEEUW, J. W., LEWAN, M. D. & DAMSTE, J. S. S. 1996. Impact of dia-and catagenesis on sulphur and oxygen sequestration of biomarkers as revealed by artificial maturation of an immature sedimentary rock. *Organic Geochemistry*, 25, 391-426.
- KRINGOS, N., SCARPAS, A., COPELAND, A. & YOUTCHEFF, J. 2008a. Modelling of combined physical-mechanical moisture-induced damage in asphaltic mixes Part 2: moisture susceptibility parameters. *International Journal of Pavement Engineering*, 9, 129-151.
- KRINGOS, N., SCARPAS, T., KASBERGEN, C. & SELVADURAI, P. 2008b. Modelling of combined physical-mechanical moisture-induced damage in asphaltic mixes, Part 1: governing processes and formulations. *International Journal of Pavement Engineering*, 9, 115-128.
- KWOK, D. Y. & NEUMANN, A. W. 1999. Contact angle measurement and contact angle interpretation. *Advances in Colloid and Interface Science*, 81, 167-249.
- LEE, H.-J. & KIM, Y. R. 1998. Viscoelastic constitutive model for asphalt concrete under cyclic loading. *Journal of Engineering Mechanics*, 124, 32-40.
- LESUEUR, D. 2009. The colloidal structure of bitumen: Consequences on the rheology and on the mechanisms of bitumen modification. *Advances in Colloid and Interface Science*, 145, 42-82.
- LI, D. D. & GREENFIELD, M. L. 2011. High internal energies of proposed asphaltene structures. *Energy & Fuels*, 25, 3698-3705.
- LI, D. D. & GREENFIELD, M. L. 2014a. Chemical compositions of improved model asphalt

- systems for molecular simulations. *Fuel*, 115, 347-356.
- LI, D. D. & GREENFIELD, M. L. 2014b. Viscosity, relaxation time, and dynamics within a model asphalt of larger molecules. *The Journal of Chemical Physics*, 140, 034507.
- LIANG, R. Y. & ZHOU, J. 1997. Energy based approach for crack initiation and propagation in viscoelastic solid. *Engineering Fracture Mechanics*, 58, 71-85.
- LIRA-GALEANA, C. & HAMMAMI, A. 2000. Wax precipitation from petroleum fluids: A review. *Developments in Petroleum Science*. Elsevier.
- LITTLE, D. N. & BHASIN, A. 2006. Using surface energy measurements to select materials for asphalt pavement. Final Report for NCHRP Project 9-37.
- LU, Y. & WANG, L. 2010. Nanoscale modelling of mechanical properties of asphalt–aggregate interface under tensile loading. *International Journal of Pavement Engineering*, 11, 393-401.
- LU, Y. & WANG, L. 2011. Nano-mechanics modelling of deformation and failure behaviours at asphalt–aggregate interfaces. *International Journal of Pavement Engineering*, 12, 311-323.
- LU, Y. & WANG, L. 2017. Atomistic modelling of moisture sensitivity: a damage mechanisms study of asphalt concrete interfaces. *Road Materials and Pavement Design*, 18, 200-214.
- LUO, X., LUO, R. & LYTTON, R. L. 2013. Modified Paris's law to predict entire crack growth in asphalt mixtures. *Transportation Research Record*, 2373, 54-62.
- LUO, X., LUO, R. & LYTTON, R. L. 2014. Energy-based crack initiation criterion for viscoelastoplastic materials with distributed cracks. *Journal of Engineering Mechanics*, 141, 04014114.
- LUO, X., ZHANG, Y. & LYTTON, R. L. 2016. Implementation of pseudo J-integral based Paris' law for fatigue cracking in asphalt mixtures and pavements. *Materials and Structures*, 49, 3713-3732.
- LYNE, Å. L., REDELIUS, P., COLLIN, M. & BIRGISSON, B. 2013. Characterization of stripping properties of stone material in asphalt. *Materials and Structures*, 46, 47-61.
- LYTTON, R. L., MASAD, E. A., ZOLLINGER, C., BULUT, R. & LITTLE, D. N. 2005. Measurements of surface energy and its relationship to moisture damage. Final Report for FHWA/TX-05/0-4524-2.
- LYTTON, R. L., ZHANG, Y., GU, F. & LUO, X. 2018. Characteristics of damaged asphalt mixtures in tension and compression. *International Journal of Pavement Engineering*, 19, 292-306.
- MAI, Y.-W. & COTTERELL, B. 1986. On the essential work of ductile fracture in polymers. *International Journal of Fracture*, 32, 105-125.
- MARTONO, W., BAHIA, H. U. & D'ANGELO, J. 2007. Effect of testing geometry on measuring fatigue of asphalt binders and mastics. *Journal of Materials in Civil Engineering*, 19, 746-752.
- MARYNOWSKI, L., ROSPONDEK, M. J., ZU RECKENDORF, R. M. & SIMONEIT, B. R. 2002. Phenylidibenzofurans and phenylidibenzothiophenes in marine sedimentary rocks and hydrothermal petroleum. *Organic Geochemistry*, 33, 701-714.
- MASAD, E. A., ZOLLINGER, C., BULUT, R., LITTLE, D. N. & LYTTON, R. L. 2006. Characterization of HMA moisture damage using surface energy and fracture properties (with discussion). *Journal of the Association of Asphalt Paving Technologists*, 75.
- MIRÓ, R., MARTÍNEZ, A. H., MORENO-NAVARRO, F. & DEL CARMEN RUBIO-GÁMEZ, M. 2015. Effect of ageing and temperature on the fatigue behaviour of bitumens. *Materials & Design*, 86, 129-137.
- MIRZABABAEI, P. 2016. Effect of zycotherm on moisture susceptibility of Warm Mix Asphalt mixtures prepared with different aggregate types and gradations. *Construction and Building Materials*, 116, 403-412.

- MORAES, R., VELASQUEZ, R. & BAHIA, H. 2017. Using bond strength and surface energy to estimate moisture resistance of asphalt-aggregate systems. *Construction and Building Materials*, 130, 156-170.
- MULLINS, O. C. 2010. The modified Yen model. *Energy & Fuels*, 24, 2179-2207.
- MURGICH, J., RODRÍGUEZ, J. & ARAY, Y. 1996. Molecular recognition and molecular mechanics of micelles of some model asphaltenes and resins. *Energy & Fuels*, 10, 68-76.
- NETZEL, D. A. & ROVANI, J. F. 2007. Direct separation and quantitative determination of (n-, iso-) alkanes in neat asphalt using urea adduction and high-temperature gas chromatography (HTGC). *Energy & fuels*, 21, 333-338.
- NICKEL, E. H. 1995. Definition of a mineral. De Gruyter.
- NIKITIN, L. 1984. Application of the Griffith's approach to analysis of rupture in viscoelastic bodies. *International Journal of Fracture*, 24, 149-157.
- NUÑEZ, J. Y. M., LEONEL, E. D. & FAXINA, A. L. 2016. Fatigue characteristics of modified asphalt binders using fracture mechanics. *Engineering Fracture Mechanics*, 154, 1-11.
- OLDENBURG, T., HUANG, H., DONOHOE, P., WILLSCH, H. & LARTER, S. 2004. High molecular weight aromatic nitrogen and other novel hopanoid-related compounds in crude oils. *Organic Geochemistry*, 35, 665-678.
- PAN, J. & TAREFDER, R. A. 2016. Investigation of asphalt aging behaviour due to oxidation using molecular dynamics simulation. *Molecular Simulation*, 42, 667-678.
- PAN, T., LU, Y. & LLOYD, S. 2012. Quantum-chemistry study of asphalt oxidative aging: an XPS-aided analysis. *Industrial & Engineering Chemistry Research*, 51, 7957-7966.
- PARIS, P. & ERDOGAN, F. 1963. A critical analysis of crack propagation laws.
- PETERSEN, J. C. 2000. Chemical composition of asphalt as related to asphalt durability. *Developments in Petroleum Science*. Elsevier.
- PETERSEN, J. C. 2009. A review of the fundamentals of asphalt oxidation: chemical, physicochemical, physical property, and durability relationships. *Transportation Research Circular*.
- PETERSEN, J. C. & GLASER, R. 2011. Asphalt oxidation mechanisms and the role of oxidation products on age hardening revisited. *Road Materials and Pavement Design*, 12, 795-819.
- PETERSEN, J. C. & HARNBERGER, P. M. 1998. Asphalt aging: dual oxidation mechanism and its interrelationships with asphalt composition and oxidative age hardening. *Transportation Research Record*, 1638, 47-55.
- PLANCHE, J.-P., ANDERSON, D., GAUTHIER, G., LE HIR, Y. & MARTIN, D. 2004. Evaluation of fatigue properties of bituminous binders. *Materials and Structures*, 37, 356-359.
- POPLE, S. & WILLIAMS, M. 2002. *Science to GCSE*, Oxford University Press, USA.
- QIN, Q., SCHABRON, J. F., BOYSEN, R. B. & FARRAR, M. J. 2014. Field aging effect on chemistry and rheology of asphalt binders and rheological predictions for field aging. *Fuel*, 121, 86-94.
- RAPAPORT, D. C. & RAPAPORT, D. C. R. 2004. *The art of molecular dynamics simulation*, Cambridge university press.
- REDELIUS, P. 2000. Solubility parameters and bitumen. *Fuel*, 79, 27-35.
- SAFAEI, F. & CASTORENA, C. 2016. Temperature effects of linear amplitude sweep testing and analysis. *Transportation Research Record*, 2574, 92-100.
- SAFAEI, F. & CASTORENA, C. 2017. Material nonlinearity in asphalt binder fatigue testing and analysis. *Materials & Design*, 133, 376-389.
- SAFAEI, F., CASTORENA, C. & KIM, Y. R. 2016. Linking asphalt binder fatigue to asphalt mixture fatigue performance using viscoelastic continuum damage modeling. *Mechanics of Time-Dependent Materials*, 20, 299-323.
- SCHAPERLY, R. A. 1975. A theory of crack initiation and growth in viscoelastic media.

- International Journal of Fracture*, 11, 141-159.
- SCHAPERLY, R. A. 1984. Correspondence principles and a generalized J integral for large deformation and fracture analysis of viscoelastic media. *International Journal of Fracture*, 25, 195-223.
- SCHMETS, A., KRINGOS, N., SCARPAS, A., DUIF, C., SCHITTER, G. & PAULI, T. 2009. First-principles investigation of the multiple phases in bituminous materials: the case of asphaltene stacking. *Advanced testing and characterisation of bituminous materials*, 1, 143-150.
- SHAN, L., TAN, Y., UNDERWOOD, S. & KIM, Y. R. 2010. Application of thixotropy to analyze fatigue and healing characteristics of asphalt binder. *Transportation Research Record*, 2179, 85-92.
- SHAN, L., TIAN, S., HE, H. & REN, N. 2017. Internal crack growth of asphalt binders during shear fatigue process. *Fuel*, 189, 293-300.
- SHEN, S., AIREY, G. D., CARPENTER, S. H. & HUANG, H. 2006. A dissipated energy approach to fatigue evaluation. *Road Materials and Pavement Design*, 7, 47-69.
- SHEN, S. & CARPENTER, S. H. 2005. Application of the dissipated energy concept in fatigue endurance limit testing. *Transportation Research Record*, 1929, 165-173.
- SHEN, S., CHIU, H.-M. & HUANG, H. 2010. Characterization of fatigue and healing in asphalt binders. *Journal of Materials in Civil Engineering*, 22, 846-852.
- SIMANZHENKOV, V. & IDEM, R. 2003. *Crude oil chemistry*, Crc Press.
- SUN, D., LIN, T., ZHU, X., TIAN, Y. & LIU, F. 2016. Indices for self-healing performance assessments based on molecular dynamics simulation of asphalt binders. *Computational Materials Science*, 114, 86-93.
- SUN, H. 1998. COMPASS: an ab initio force-field optimized for condensed-phase applications overview with details on alkane and benzene compounds. *The Journal of Physical Chemistry B*, 102, 7338-7364.
- TAN, Y. & GUO, M. 2013. Using surface free energy method to study the cohesion and adhesion of asphalt mastic. *Construction and Building Materials*, 47, 254-260.
- TANAKA, K. & MURA, T. 1981. A dislocation model for fatigue crack initiation. *Journal of Applied Mechanics*, 48, 97-103.
- TAREFDER, R. A. & ARISA, I. 2011. Molecular dynamic simulations for determining change in thermodynamic properties of asphaltene and resin because of aging. *Energy & Fuels*, 25, 2211-2222.
- THOM, N. 2014. *Principles of pavement engineering*, London, ICE Publishing.
- THOMAS, Y. 1805. An essay on the cohesion of fluids. *Philos. Trans. R. Soc. London*, 95, 65-87.
- TSAI, B.-W., MONISMITH, C., DUNNING, M., GIBSON, N., D'ANGELO, J., LEAHY, R., KING, G., CHRISTENSEN, D., ANDERSON, D. & DAVIS, R. 2005. Influence of asphalt binder properties on the fatigue performance of asphalt concrete pavements. *Journal of the Association of Asphalt Paving Technologists*, 74, 733-789.
- TSCHEGG, E., RITCHIE, R. & MCCLINTOCK, F. 1983. On the influence of rubbing fracture surfaces on fatigue crack propagation in mode III. *International Journal of Fatigue*, 5, 29-35.
- VAN OSS, C., GOOD, R. & CHAUDHURY, M. 1988. Additive and nonadditive surface tension components and the interpretation of contact angles. *Langmuir*, 4, 884-891.
- VAN OSS, C. J. 2002. Use of the combined Lifshitz-van der Waals and Lewis acid-base approaches in determining the apolar and polar contributions to surface and interfacial tensions and free energies. *Journal of Adhesion Science and Technology*, 16, 669-677.
- VAN OSS, C. J., CHAUDHURY, M. & GOOD, R. J. 1987. Monopolar surfaces. *Advances in Colloid and Interface Science*, 28, 35-64.
- VENKATARAMAN, G., CHUNG, Y.-W. & MURA, T. 1991. Application of minimum energy formalism in a multiple slip band model for fatigue—I. Calculation of slip band

- spacings. *Acta Metallurgica et Materialia*, 39, 2621-2629.
- VERENICH, S., PAUL, S. & POURDEYHIMI, B. 2008. Surface and bulk properties of glycidyl methacrylate modified polypropylene: Experimental and molecular modeling studies. *Journal of Applied Polymer Science*, 108, 2983-2987.
- WANG, C., CASTORENA, C., ZHANG, J. & RICHARD KIM, Y. 2015a. Unified failure criterion for asphalt binder under cyclic fatigue loading. *Road Materials and Pavement Design*, 16, 125-148.
- WANG, C., ZHANG, H., CASTORENA, C., ZHANG, J. & KIM, Y. R. 2016. Identifying fatigue failure in asphalt binder time sweep tests. *Construction and Building Materials*, 121, 535-546.
- WANG, H., LIN, E. & XU, G. 2015b. Molecular dynamics simulation of asphalt-aggregate interface adhesion strength with moisture effect. *International Journal of Pavement Engineering*, 18, 414-423.
- WANG, P., DONG, Z.-J., TAN, Y.-Q. & LIU, Z.-Y. 2015c. Investigating the interactions of the saturate, aromatic, resin, and asphaltene four fractions in asphalt binders by molecular simulations. *Energy & Fuels*, 29, 112-121.
- WEI, J., DONG, F., LI, Y. & ZHANG, Y. 2014. Relationship analysis between surface free energy and chemical composition of asphalt binder. *Construction and Building Materials*, 71, 116-123.
- XU, G. & WANG, H. 2016a. Molecular dynamics study of interfacial mechanical behavior between asphalt binder and mineral aggregate. *Construction and Building Materials*, 121, 246-254.
- XU, G. & WANG, H. 2016b. Study of cohesion and adhesion properties of asphalt concrete with molecular dynamics simulation. *Computational Materials Science*, 112, 161-169.
- XU, G. & WANG, H. 2017. Molecular dynamics study of oxidative aging effect on asphalt binder properties. *Fuel*, 188, 1-10.
- YAO, H., DAI, Q. & YOU, Z. 2015. Chemo-physical analysis and molecular dynamics (MD) simulation of moisture susceptibility of nano hydrated lime modified asphalt mixtures. *Construction and Building Materials*, 101, 536-547.
- YAO, H., DAI, Q., YOU, Z., BICK, A., WANG, M. & GUO, S. 2017. Property analysis of exfoliated graphite nanoplatelets modified asphalt model using molecular dynamics (MD) method. *Applied Sciences*, 7, 43.
- YI, J., PANG, X., FENG, D., PEI, Z., XU, M., XIE, S. & HUANG, Y. 2018. Studies on surface energy of asphalt and aggregate at different scales and bonding property of asphalt-aggregate system. *Road Materials and Pavement Design*, 19, 1102-1125.
- YIN, Y., CHEN, H., KUANG, D., SONG, L. & WANG, L. 2017. Effect of chemical composition of aggregate on interfacial adhesion property between aggregate and asphalt. *Construction and Building Materials*, 146, 231-237.
- ZHANG, J., APEAGYEI, A. K., AIREY, G. D. & GRENFELL, J. R. 2015. Influence of aggregate mineralogical composition on water resistance of aggregate-bitumen adhesion. *International Journal of Adhesion and Adhesives*, 62, 45-54.
- ZHANG, L. & GREENFIELD, M. L. 2007a. Analyzing properties of model asphalts using molecular simulation. *Energy & fuels*, 21, 1712-1716.
- ZHANG, L. & GREENFIELD, M. L. 2007b. Molecular orientation in model asphalts using molecular simulation. *Energy & fuels*, 21, 1102-1111.
- ZHANG, L. & GREENFIELD, M. L. 2007c. Relaxation time, diffusion, and viscosity analysis of model asphalt systems using molecular simulation. *The Journal of Chemical Physics*, 127, 194502.
- ZHANG, X., LU, G., WEN, X. & YANG, H. 2009. Molecular dynamics investigation into the adsorption of oil-water-surfactant mixture on quartz. *Applied Surface Science*, 255, 6493-6498.
- ZHANG, Y. & GAO, Y. 2019. Predicting crack growth in viscoelastic bitumen under a

- rotational shear fatigue load. *Road Materials and Pavement Design*, 1-20.
- ZHANG, Y., GU, F., BIRGISSON, B. & LYTTON, R. L. 2018. Modelling cracking damage of asphalt mixtures under compressive monotonic and repeated loads using pseudo J-integral Paris' law. *Road Materials and Pavement Design*, 19, 525-535.
- ZHANG, Y., LUO, R. & LYTTON, R. L. 2011. Characterizing permanent deformation and fracture of asphalt mixtures by using compressive dynamic modulus tests. *Journal of Materials in Civil Engineering*, 24, 898-906.
- ZHANG, Y., LUO, R. & LYTTON, R. L. 2012. Mechanistic modeling of fracture in asphalt mixtures under compressive loading. *Journal of Materials in Civil Engineering*, 25, 1189-1197.
- ZHANG, Y., LUO, R. & LYTTON, R. L. 2013. Anisotropic characterization of crack growth in the tertiary flow of asphalt mixtures in compression. *Journal of Engineering Mechanics*, 140, 04014032.
- ZHANG, Y., LUO, X., LUO, R. & LYTTON, R. L. 2014. Crack initiation in asphalt mixtures under external compressive loads. *Construction and Building Materials*, 72, 94-103.
- ZHOU, F., HU, S., SCULLION, T., Chen D., Qi X., & Claros G. 2007. Development and verification of the overlay tester based fatigue cracking prediction approach. *Journal of the Association of Asphalt Paving Technologists*, 76, 627-662.
- ZHOU, F., MOGAWER, W., LI, H., ANDRIESCU, A. & COPELAND, A. 2012. Evaluation of fatigue tests for characterizing asphalt binders. *Journal of Materials in Civil Engineering*, 25, 610-617.
- ZHOU, X., WU, S., LIU, Q., CHEN, Z. & YI, M. 2015. Effect of surface active agents on the rheological properties and solubility of layered double hydroxides-modified asphalt. *Materials Research Innovations*, 19, S5-978-S5-982.